Effects of Silicon Oxides as Substrates for Graphene-based Gas Sensor

by

Shengtai Shi

For the degree of

Master of Science in Microelectronics

At Delft University of Technology

To be defended publicly on Friday November 24th, 2017 at 13:00PM

Supervisor:

Prof.dr. Lina Sarro

Daily Supervisors:

Dr. Filiberto Ricciardella

Dr.ir. Sten Vollebregt

Thesis Committee:

Prof.dr. Lina Sarro

Dr. Filiberto Ricciardella

Dr.ir. Sten Vollebregt

Dr. Olindo Isabella

Preface

The two years at TU Delft have brought me lots of valuable memories. This thesis marks an end to my journey for Master of Science degree. There is no doubt that without the help from people I got to know during my thesis project, I would not achieve this outcome.

First of all, my time within the ECTM master student group is relatively shorter than my peers, however I really appreciated the connections I shared with everyone during this period of time to learn, to inspire, to encourage, to support each other. It is a wonderful period of time that enriched my soul and I will certainly keep this spirit high for the roads ahead.

When I started this thesis project, it was an unfavorable time during my study. Just shortly afterwards, I felt things were going on the right direction working with Dr. Sten Vollebregt and Dr. Filiberto Ricciardella. Dr. Sten Vollebregt shared the information about this project with me at the first place and introduced me to the Graphene group, for that I felt thankful. Besides, it is due to his solid guidance so that my work in cleanroom could have progressed steadily and fast towards the outcome.

Dr. Filiberto Ricciardella, who was very much involved in almost every aspect of my thesis project, has had given me numerous suggestions motiving me to achieve the best out of this experience. For countless times that I learned how to improve my work from his inspiring yet meticulous supervision. In addition, I am truly thankful for his understanding and encouragement all this time long from which I developed my confidence in this work. For my thesis experience, I simply could not ask for more than having Dr. Filiberto Ricciardella as my daily supervisor.

In addition, I would like to thank Prof. dr. Lina Sarro, my project supervisor, who showed care and trust to me. Also, I am grateful for the help received from Dr. Paolo Sberna, who guided me on material science study and provided valuable trainings for my cleanroom works. Furthermore, my gratitude goes to other personnel of ECTM and EKL, especially for Boyao, Jian, Silvana, Tom and Marian.

At last, I want to express my deep appreciation to my family and friends in China and here in the Netherlands. Your continuing support is my best motivation and reason to have made this far. Above all, to my lovely girlfriend, who shared every up and down with me this year, truly brought my life in this period of time with joy and turned every single day meaningful.

Shengtai Shi

Delft, November 2017

Contents

Chapter 1. Thesis Introduction **1**

1.0 Overview 1

1.1 The growing needs for gas sensing applications 1

1.2 From SnO2 to Graphene: the development of technology 2

1.3 Research Objectives 4

1.4 Outline of the thesis 5

References 6

Chapter 2. Chem-resistor Based Graphene Gas Sensor **7**

2.0 Overview 7

2.1 Graphene as a promising material for gas sensing 7

2.2 Sensing mechanism of chem-resistor graphene gas sensor 9

2.3 Conclusion and opportunities in studies of substrate materials 10

References 11

Chapter 3. Study of Device Performances on Three Kinds of SiO_2 as Substrates **13**

3.0 Overview 13

3.1 Gas sensing experiment setup and environments 13

3.2 Analysis methodology and an example based on sensing responses from protocol (I) 14

3.3 Analysis of sensing responses from protocol (II) 19

3.4 Analysis of sensing responses from protocol (III) 23

3.5 Conclusions and additional discussions 28

References 29

Chapter 4. Material Study of PECVD, LPCVD and Thermal SiO_2 Substrates **30**

4.0 Overview 30

4.1 Substrate Material Fabrication and Related Experiment Setup 30

4.2 Characterization of substrate materials by C-V measurements 33

4.3 Characterization of substrate materials by FTIR measurements 37

4.4 Comparison of FLG on top of oxides using Raman measurement data 44

4.5 Conclusions and implications on sensing behavior from material study 50

References 52

Chapter 5. Study of Contact Resistance between Graphene with Different Metals 54

5.0 Overview 54

5.1 Motivation of contact resistance study and Experiment Setups 54

5.2 Contact Resistance Measurement Results and Analysis 56

5.3 Conclusions 68

References... 69

Chapter 6. Thesis Conclusions and Recommendations 70

6.1 Conclusions of thesis study 70

6.2 Recommendations for future works.. 71

Appendix A CVD Graphene Growth Environment... 73

Appendix B Processing Details of C-V Structures 74

Appendix C Processing Details of Metal-graphene Contacts 76

List of Abbreviations 79

List of Symbols 80

Chapter 1. Thesis Introduction

1.0 Overview

This chapter first introduces the origin of the growing demands of gas sensing and future trends in section 1.1. Then, the development of gas sensing technology over the past several decades is briefly discussed in section 1.2. Finally, the research goals of this study and the outline of this thesis are presented in section 1.3 and 1.4 respectively.

1.1 The growing needs for gas sensing applications

As technology progresses in our society, rapid industrialization around the world has deeply transformed the way people live and work. Industrialized manufacturing requires precise measurement and control of materials. Modern living style brings more concerns about environment. All of them lead to fast growing needs for gas sensing technology over the past several decades. For example, its usage has been seen in fields like pollution control study, disease diagnosis, manufacturing security and national defense [1]. Among various types of gases, a handful of them received continuous attention from researchers and scientists, including O_2, CO, CO_2, H_2, SO_2, NO_2, NH_3, water vapor and so on. It is crucial for people to be able to detect and monitor these gases. In fact, these gases do not only often occur during human agricultural and industrial activities, but could also cause environmental or public health problems. For instance, approximately 88% of ammonia (NH_3) production in United States is used as fertilizer [2], however, gaseous ammonia will react with oxides of nitrogen and sulfur to form fine sized particles, which accounts for 47% of atmospheric particulate matter with a diameter less than 2.5 μm (PM2.5) according to monitoring data in eastern United States. And studies of PM2.5 particles indicate that these particles are harmful for human health and may lead to increased mortality [3]. Nitrogen dioxide (NO_2) and nitrogen monoxide (NO) are harmful for human health as well. In fact, NO_2 raises the chances of respiratory infections [6] and European Union has a standard showing that the concentration of NO_2 in the air should not exceed 40 μg/m3 at an average period of one year [4,5]. The cases above present only a small portion of potential problems brought by various gases, therefore the need to develop better gas sensors to detect and monitor different gases is growing from a macroscopic point of view.

Since 2004, graphene has grabbed lots of attention from researchers due to its superior material properties [13,15,16]. It also did not take long for people to discover its advantages in gas sensing applications, for example, in 2007 Geim and Novoselov have reported that graphene “offers clear advantages” in gas sensors [13]. In the same year, Schedin et al. published a groundbreaking paper demonstrating the ability to detect

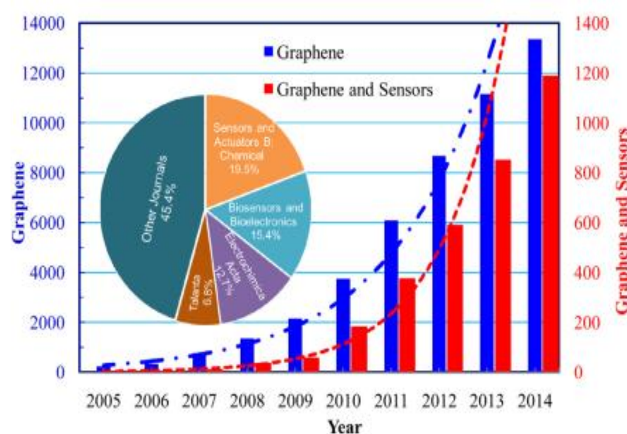

Figure 1.1. Publications on "Graphene" and "Graphene and Sensors" from 2005 to 2014 [8

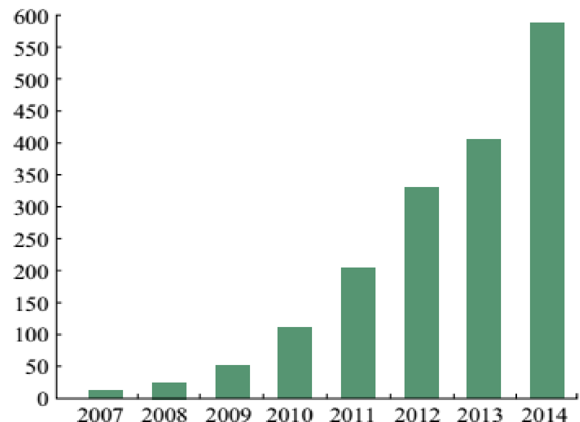

Figure 1.2. Number of publications on graphene based gas/vapor sensor, dated from 2007 to 2014 [9]

down to single gas molecule by using mechanical-exfoliated graphene as sensing layer [7]. This work showed promising results and inspired followers to continuously research on graphene for gas sensing applications. People hope to develop graphene gas sensors that are small, low cost, low power and yet have better sensitivity than current solid-state gas sensors. The strong interest in graphene sensing applications can be seen from the fast-growing publications concerning graphene sensors. The study from Varghese et al. indicates that within Scopus search, the publications on graphene and sensors increased more than 20 times from 2008 to 2014 [8], as presented in Figure 1.1. This is an average growth rate of almost 70% per year. As shown in Figure 1.2, similar results also can be found in the review reported by Wang et al. in 2015 [9]. These data clearly reflect the high interest in graphene sensing from people. Eventually, people believe in the future graphene based gas sensors will give birth to a new class of gas sensors with "superior sensitivity, excellent selectivity, reduced size, and extended lifetimes for a wide range of environments and applications" [9].

1.2 From SnO_2 to Graphene: the development of technology

Sensing technologies over past decades have developed rapidly and they are optimized for detection of various gases. As Moseley pointed out, there are currently three kinds of target for gas sensing: (1) Oxygen; (2) Flammable gases; (3) Toxic gases in air. Especially for toxic gases, sensor with ability to detect gas concentration of less than 1ppm or even lower than 100ppb is required [10]. Moseley also reported that "The majority of the well established types of gas sensor are solid-state devices which combine rugged construction with sufficiently low purchase costs to allow widespread deployment" [10]. Therefore, here it is reasonable to refine the context of our discussion to be within solid-state gas sensors. So far there are three main types of solid-state gas sensors being massively deployed, namely: solid electrolytes type (electrochemical sensors), catalytic combustion type (pellistors) and resistance modulation of semiconducting oxides type (chemiresistance based sensors) [11].

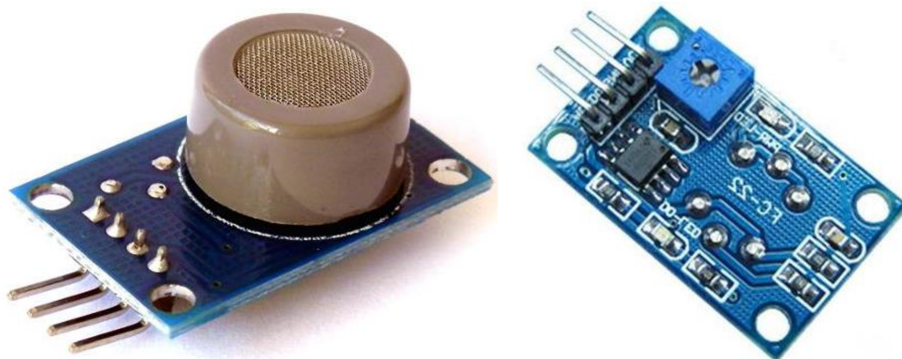

Figure 1.3. MQ-9 SnO2 Gas sensor, an example of commercial semiconducting oxide sensor

It is worth mentioning that semiconducting oxides type beats the other two types as it is the fastest growing on the global market among all three types. A famous example of this kind is the tin dioxide (SnO_2) sensor which has been used in countless quantities of residences around the world to provide alarm for CO, explosion and other potential hazards. Reasons behind the popularity of semiconducting oxide sensors can be observed from the following table. It provides a good comparison in terms of sensor performance. It can be found that on each category of performance, semiconducting oxide gas sensor is better or as good as the other two types except selectivity.

Table 1.1. Performance comparison of solid-state gas sensors [11]

Parameters	Type of gas sensors		
	Semiconducting Oxide	**Catalytic Combustion**	**Electrochemical**
Sensitivity	e	g	g
Accuracy	g	g	g
Selectivity	p	b	g
Response time	e	g	p
Stability	g	g	b
Durability	g	g	p
Maintenance	e	e	g
Cost	e	e	g
Suitability to portable instruments	e	g	b
e: excellent; g: good; p: poor; b: bad;			

The discussion above examined the overall advantages of semiconducting oxide sensors. Indeed, a major faction of sensors in gas sensing utilize the variation of electrical properties as signals for detection. Liu et al. listed 4 kinds of material choices for this type of sensor in their review for gas sensing technology [1]. With semiconducting oxide being one of this category, the others are polymer, carbon nanotubes and moisture absorbing material. Upon being contact with analytes, sensors generate a change in the electrical properties of these materials, such as resistance or capacitance. This change in electrical property can be interpreted as a sign of detection and analyzed quantitively to determine key sensor parameters. More detailed discussions of analyte detection mechanism and analysis of electrical signals will be introduced in Chapter 2 and Chapter 3.

However, each kind of material is in fact specialized for a certain type of gas and has its pros and cons. A detailed summary can be seen in Table 1.2 which is excerpted from [1].

As Liu et al. summarized in the review [1], metal oxide semiconductor has advantages to be cheap in cost, reliable and reproducible in quality and yet versatile for different gases. Comparing with other materials, these advantages make metal oxide semiconductor stand out easily, being economically and technologically viable to be applied for massive industrial and daily use.

Two analyses with different rules, the judgements are alike. Despite all the advantages making semiconducting oxide sensor the crown jewel in gas sensing, attentions should be paid to its serious drawbacks. First of all, semiconducting oxide sensor cannot work at room temperature. A micro environment with an elevated temperature has to been provided in order for the sensor to work properly. This requirement is usually fulfilled with a micro-hotplate or filament installed as part of the sensor. Second, poor selectivity still hinders the development of semiconducting oxide sensor. Because disturbing factors like ambient relative humidity change and interferences with gases of similar chemical composition could all easily drift the sensor response away from the optimal value. Although the selectivity could be improved by means like doping the material surface with a suitable catalyst material or using a sensor array [1], the chances of selectivity being compromised is still high for traditional semiconducting oxide sensors. Third and the last, sensitivity has only recently appeared to be a drawback since the demand for detections in sub ppm or ppb level is raising in the future. However, this drawback has put semiconducting oxide sensor at a difficult position to keep its dominating status, because carbon based materials, including CNTs and more recently graphene, are more advantageous in this task.

Table 1.2. Summary of existing gas sensing materials using electrical sensing methods [1]

Materials	Advantages	Disadvantages	Target Gases and Application Fields
Metal Oxide Semiconductor	a) Low cost b) Short response time c) Wide range of target gases d) Long life time	a) Relatively low sensitivity and selectivity b) Sensitive to environmental factors c) High energy consumption	Industrial applications and civil use
Polymer	a) High sensitivity b) Short response time c) Low cost of fabrication d) Simple and portable structure e) Low energy consumption	a) Long-time instability b) Irreversibility c) Poor selectivity	a) Indoor air monitoring b) Storage place of synthetic products as paints, wax or fuels c) Workplaces like chemical industries
Carbon Nanotubes	a) Ultra-sensitive b) Great adsorptive capacity c) Large surface-area-to-volume ratio d) Quick response time e) Low weight	a) Difficulties in fabrication and repeatability b) High cost	Detection of partial discharge (PD)
Moisture Absorbing Material	a) Low cost b) Low weight c) High selectivity to water vapor	a) Vulnerable to friction b) Potential irreversibility in high humidity	Humidity monitoring

In Table 1.2, it is listed that carbon nanotube (CNT) is ultrasensitive and this big advantage make people consider CNT as a promising candidate for gas detection in ultra-low concentrations. Essentially, CNTs are suitable for this task because of its large surface-to-volume ratio and excellent electrical properties [12]. And in fact, graphene has those advantages too. Recent development in graphene research has shown its superiority in gas sensing [7,13]. The 2D planar structure provides graphene with potentially the highest surface- to-volume ratio [14]. In addition, because of the 2D structure, graphene is more compatible with current microfabrication technologies than the CNTs [12]. This property makes graphene easier to be integrated with standard systems. Considering the rapid development happened in graphene fabrication technology during the past decade, there is a reason to believe graphene can possibly overcome the fabrication disadvantages that troubled CNT gas sensors.

1.3 Research Objectives

This thesis work serves for people to understand how to improve the sensing responses of graphene gas sensor. The work in this thesis is carried out based on graphene based chem-resistor sensing device. Chem-resistor sensor design is no new story. Indeed, semiconducting oxide sensor is one kind of this family and by now it is a mature design for sensors. Through literature study, it is found that graphene chem-resistor sensor is well adopted and used in research now [7,8,9,12,14]. More technological details about chem-resistor graphene gas sensor will be discussed in Chapter 2.

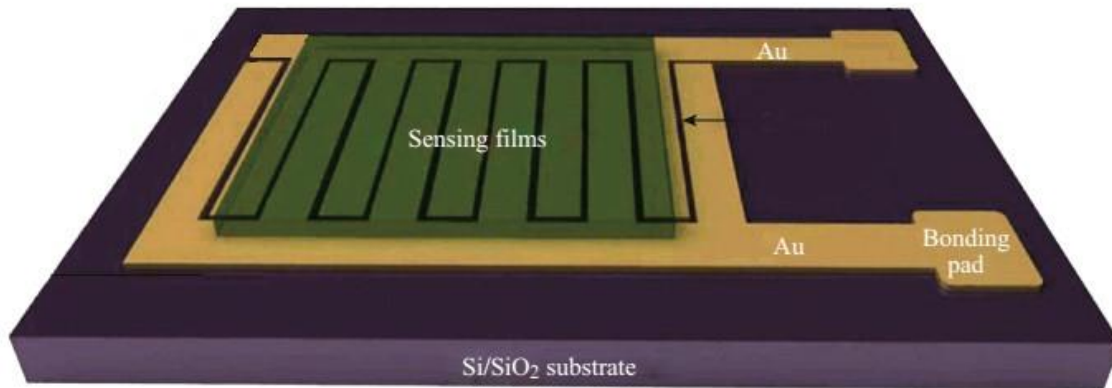

Figure 1.4. Design diagram of a typical chem-resistor sensor [9]

Past studies mainly worked around graphene itself to improve the performance of the sensor in terms of sensitivity, limit of detection and durability et al. However, this thesis focuses on investigating the role of the SiO_2 layer, which in general is the substrate material for chem-resistor type sensor [9]. Since SiO_2 layer is in touch directly with the graphene sensing layer, then graphene physical and electrical properties are susceptible to the influence from SiO_2. This approach looks at the problem from a new perspective which will provide valuable insights from a holistic thinking point of view. Within the scope of this thesis study, the performance of graphene gas sensors is studied and analyzed based on three different oxides, namely thermally grown SiO_2, plasma enhanced chemical vapor deposition (PECVD) SiO_2 and low pressure chemical vapor deposition (LPCVD) SiO_2.

The central objective is to investigate the relationship between the choice of oxide materials and the sensor performance. And additionally, efforts are made to discover reasons behind the relationship.

Besides, another part the thesis focuses on studying the electrical behavior of contacts made between graphene and different metals such as Au, Ti, Al, and Pd. The objective for this part of the thesis is to provide more knowledge and understanding of the interactions between graphene and these metals. Apart from the active sensing part, electrical contacts also play an important role in the system. Therefore, such study is necessary in order to improve performance of electrical contacts in graphene sensors.

1.4 Outline of the thesis

In Chapter 2, this thesis will introduce details of graphene properties and its related sensing mechanism in chem-resistor. Chapter 3 to Chapter 5 will cover all the experimental works and analysis of sensing data from experiments.

Specifically speaking, in Chapter 3, the contents cover a thorough description about the gas sensing experiments and discussion about the analysis of corresponding data. The results quantitively present the effects of different oxide materials. Chapter 4 focuses on determining the main differences in material properties among three different kinds of oxides. The results provide explanations to the sensing behavior discussed in Chapter 3. Finally, Chapter 5 is about the study of contact resistance between graphene and metals. This work can help people understand which material is more suitable to be used together with graphene to make electrical contacts in a sensor.

References

[1] Liu, X., Cheng, S., Liu, H., Hu, S., Zhang, D. and Ning, H., 2012. A survey on gas sensing technology. *Sensors*, *12*(7), pp.9635-9665.

[2] U.S. Department of Interior, U.S. Geological Survey. Mineral Commodity Summaries 2016.

[3] Anderson, N., Strader, R. and Davidson, C., 2003. Airborne reduced nitrogen: ammonia emissions from agriculture and other sources. *Environment International*, *29*(2), pp.277-286.

[4] Air quality standards, European Commission, http://ec.europa.eu/environment/air/quality/standards.htm

[5] Novikov, S., Lebedeva, N., Satrapinski, A., Walden, J., Davydov, V. and Lebedev, A., 2016. Graphene based sensor for environmental monitoring of NO 2. *Sensors and Actuators B: Chemical*, *236*, pp.1054-1060.

[6] Chauhan, A.J., Krishna, M.T., Frew, A.J. and Holgate, S.T., 1998. Exposure to nitrogen dioxide (NO2) and respiratory disease risk. *Reviews on environmental health*, *13*(1-2), p.73.

[7] Schedin, F., Geim, A.K., Morozov, S.V., Hill, E.W., Blake, P., Katsnelson, M.I. and Novoselov, K.S., 2007. Detection of individual gas molecules adsorbed on graphene. *Nature materials*, *6*(9), pp.652-655.

[8] Varghese, S.S., Lonkar, S., Singh, K.K., Swaminathan, S. and Abdala, A., 2015. Recent advances in graphene based gas sensors. *Sensors and Actuators B: Chemical*, *218*, pp.160-183.

[9] Wang, T., Huang, D., Yang, Z., Xu, S., He, G., Li, X., Hu, N., Yin, G., He, D. and Zhang, L., 2016. A review on graphene-based gas/vapor sensors with unique properties and potential applications. *Nano-Micro Letters*, *8*(2), pp.95-119.

[10] Moseley, P.T., 1997. Solid state gas sensors. *Measurement Science and technology*, *8*(3), p.223.

[11] Korotcenkov, G., 2007. Metal oxides for solid-state gas sensors: What determines our choice?. *Materials Science and Engineering: B*, *139*(1), pp.1-23.

[12] Yoon, H.J., Yang, J.H., Zhou, Z., Yang, S.S. and Cheng, M.M.C., 2011. Carbon dioxide gas sensor using a graphene sheet. *Sensors and Actuators B: Chemical*, *157*(1), pp.310-313.

[13] Geim, A.K. and Novoselov, K.S., 2007. The rise of graphene. *Nature materials*, *6*(3), pp.183-191.

[14] Ricciardella, F., Massera, E., Polichetti, T., Miglietta, M.L. and Di Francia, G., 2014. A calibrated graphene-based chemi-sensor for sub parts-per-million NO2 detection operating at room temperature. *Applied Physics Letters*, *104*(18), p.183502.

[15] Zhu, Y., Murali, S., Cai, W., Li, X., Suk, J.W., Potts, J.R. and Ruoff, R.S., 2010. Graphene and graphene oxide: synthesis, properties, and applications. Advanced materials, 22(35), pp.3906-3924.

[16] Novoselov, K.S., Fal, V.I., Colombo, L., Gellert, P.R., Schwab, M.G. and Kim, K., 2012. A roadmap for graphene. nature, 490(7419), pp.192-200.

Chapter 2. Chem-resistor Based Graphene Gas Sensor

2.0 Overview

This chapter starts by discussing the properties and fabrication techniques of graphene, in particular introducing the potential benefits of using defective graphene in gas sensing applications. Then section 2.2 is about analyte detection mechanism and working principles of chem-resistor based graphene gas sensor. Finally, additional discussions of potential research opportunity in substrate study and graphene-metal contact study are made.

2.1 Graphene as a promising material for gas sensing

In Chapter 1, the advantages of using graphene as gas sensing material have been briefly discussed. Graphene is a two-dimensional monolayer of sp^2 hybridized carbon atom densely packed in a honeycomb crystal lattice [1]. Graphene outperforms other materials in solid state gas sensor in terms of superb electrical and mechanical properties, large surface to volume ratio and better compatibility for large-scale fabrication. In addition, its excellent electrical conductivity and few defects crystal structure results in low Johnson and thermal noise [2,3]. These advantages make graphene very suitable for gas sensor applications as I reported from the discussions in Chapter 1. However, graphene obtained by different fabrication techniques varies a lot in terms of electrical and mechanical characteristics. Before quantitively analyzing graphene as the sensing material in gas sensor, it is necessary to first distinguish different types of graphene and their related qualities.

Since the Novoselov et al. first reported graphene in 2004 [4], multiple fabrication techniques have been developed. In 2011, Hill et al. summarized six fabrication techniques such as: mechanical exfoliation, chemical exfoliation, growth by chemical vapor deposition (CVD), decomposition of carbides, synthetic route and splitting nanotubes [5]. Among the six mentioned ways to prepare graphene, mechanical exfoliation is the first technique applied in experiments to prepare graphene and growth by CVD is widely considered as a promising way for large-scale fabrication. In fact, graphene used in this thesis project is also grown by CVD. Therefore, we will focus on introducing these two techniques and discuss graphene properties obtained by them respectively.

(1) Mechanical exfoliation is the original method that Novoselov et al. used to obtain graphene back in 2004 [4]. This method uses a high tack type (Nitto™ tape) to repeatedly peel small flakes out of a bulk highly oriented pyrolytic graphite [4,5,6]. Using this approach, Novoselov et al. can reliably obtain few-layer graphene (FLG) up to 10 μm in size and they managed to obtain single layer graphene (SLG) as well [4]. According to Hill et al., now it is possible to obtain millimeter sized SLG using mechanical exfoliation method [5]. The superb qualities of graphene initially reported by Novoselov et al. belong to high quality samples obtained by mechanical exfoliation. More than 10 years has passed, it is still graphene samples obtained by mechanical exfoliation that provide the best quality [5]:

- Intrinsic charge carrier mobility up to 200,000 cm^2/Vs for suspended graphene at room temperature with a carrier density of ~ 10^{12} cm^{-2} (up to 40,000 cm^2/Vs on SiO_2) Give graphene the lowest resistivity (10^{-6} Ω cm) among all matters known so far at room temperature [6,7]
- A large specific surface area of 2630 m^2g^{-1}, which provides graphene the largest sensing area per unit volume [7]

- Able to sustain current densities of 5×10^8 A / cm^2 [8]

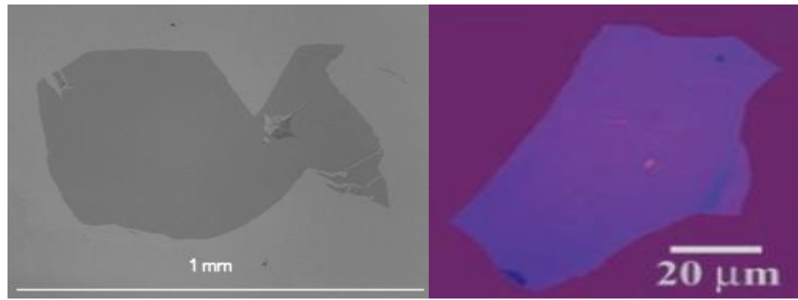

Figure 2.1. Graphene obtained by mechanical exfoliation [4,5]

(2) Besides mechanical exfoliation, graphene growth by chemical vapor deposition (CVD) has begun to receive more attention since its first appearance in 2008/2009 [10]. It is considered by people as a cost-effective and reliable solution to produce large-area SLG and multilayer graphene (MLG) with high quality [5,9,10]. There are two types of CVD for graphene, namely, Thermal CVD and Plasma-Enhanced CVD (PECVD). Thermal CVD has a working environment temperature usually above 900°C, but PECVD has a much lower working temperature around 650°C, as well as a shorter deposition [6,9,11]. In comparison to thermal CVD route, processes in PECVD for graphene are not fully understood by people and the end product is observed to be thick graphite-like structures [9,22] Therefore, PECVD graphene has an advantage to meet low-temperature requirement, but thermal CVD is better is terms of quality. In a typical graphene growth step, hydrocarbon precursor gases decompose to form carbon atoms in the desired environment with controlled temperature and pressure. Under diffusion, individual carbon atoms first dissolve into a thin pre-deposited metal catalyst layer on a rigid substrate with mediate to high carbon solubility (>0.1atomic %) [9], for example, Ni, Cu Co and Mo. These incorporated carbon atoms act like numerous nuclei in the metal structure. Then precipitation of carbon atoms happens under a controlled cooling phase of the metal catalyst, forming islands of graphene from nearby nucleus. Finally, SLG or MLG is formed depending of factors such as cooling rate of the metal layer, concentration of carbonaceous gas in CVD, metal layer carbon solubility and metal layer thickness [9,10,12]. According to Singh et al., the average number of graphene layers on a Ni catalyst layer is 3-8, while mono or bilayer graphene grows predominantly on Cu [9]. The existence of metal layer is this process plays an important role. It works as a catalyst to lower the energy barrier of the reaction. The characteristics of chosen metal layer also determines the graphene forming mechanism which affects the quality of the graphene [10]. Due to the importance of using catalytic metal layer in the process, this method to prepare graphene can also be referred to as the Catalytic CVD technique (CCVD).

Up till this stage, the CVD growth of graphene is completed. Once graphene is formed, it is necessary to remove the metal catalyst layer by chemical etching and in the end graphene film can be transferred to another substrate for the desired application [9,10]. However, the etching and transfer process introduce crystal lattice damage to the obtained graphene film, which compromises the quality of graphene. Facing this problem, on one hand efforts have been made to improve etching and transfer techniques such as shown in [11]. On the other hand, techniques such as seen in [12,14] to achieve placing graphene directly on dielectric or flexible substrate without transferring are developed. CVD process for graphene received fast development and according to Kim et al. high-quality graphene films with area as large as 30 inches can have mobility up to 7350 $cm^2V^{-1}s^{-1}$ [13]. Despite the developments of graphene CVD technology, improvements in precise control over layer thickness and large-area graphene reproducibility still need to be made before adopting graphene CVD at industrial scale [6].

From the previous discussion it is worth mentioning the fact that best electrical and mechanical properties of graphene come from high quality samples made by mechanical exfoliation. Graphene obtained by CVD is inferior in terms of quality. Having the best quality, nevertheless mechanical exfoliation is not suitable for mass production requirements because of lack of scalability and randomness in fabrication procedures [8,9]. If graphene is to realize greater application as a novel sensing material, a reliable method to synthesis large-area graphene with desired thickness has to be adopted [8]. For gas sensing applications in particular, graphene is fundamentally very promising due to its intrinsic large surface to volume ratio, outstanding conductivity and extreme low noise nature [6,7]. In addition, defects of graphene can in fact act as a helpful characteristic in gas sensing [15]. In 2009 Zhang et al., using density functional computations, predicted that defective graphene has strong interactions with CO, NO and NO_2 [15]. Later, solid experimental evidence such as reported by Ricciardella et al. in [16] reveals a clear correlation between the level of defectiveness and sensing behavior towards the analyte. Therefore, rather than using high quality graphene from mechanical exfoliation, graphene from CVD has more advantages in gas sensor development, being a reliable and cost-effective way for future large scalability applications [6].

The graphene used in this thesis work is obtained by CVD. In addition, for the sake of clarity in the following sections, unless specifically mentioned in the text, we will assume the sensing mechanism for MLG is the same as that of SLG.

2.2 Sensing mechanism of chem-resistor graphene gas sensor

Previous discussions covered the advantages and reasons of using graphene in gas sensing applications. With the aim of developing ultra-high sensitive gas sensor with fast response and recovery time [6], people have applied graphene into multiple gas sensor configurations, including: chem-resistor type, field effect transistor (FET) type, surface work function (SWF) type and surface acoustic wave (SAW) type [5-7]. Each type of sensor configuration has distinct working principle. In the following discussions we will focus on the sensing mechanism of chem-resistor graphene gas sensor.

Figure 2.2. CVD graphene on top of SiO2 with electrodes

A chem-resistor type sensor detects gases based on the conductance change of the device upon adsorption of gas species. Applying graphene as the active sensing layer in a chem-resistor gas sensor configuration can readily exploit the excellent conductivity of graphene. In addition, graphene films can be patterned with current micro-fabrication techniques, making it easy to measure the conductivity change directly through four-point probe devices [6,7]. Such benefits of graphene enable chem-resistor graphene gas sensor to be a simple, reliable and reproducible device for gas sensing [6].

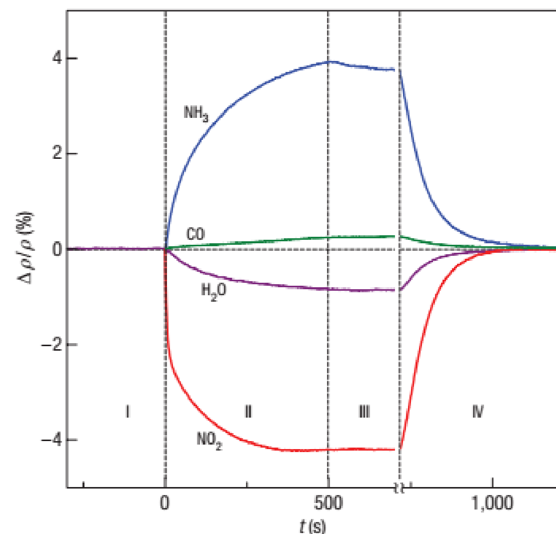

Figure 2.3. Graphene resistivity variance due to different gases [3]

At its natural state, graphene presents a zero-band gap property [8,23]. Past literature reveals the charge transfer and doping effects on graphene from gases like CO, NO,

NO_2, NH_3, H_2O [6,17]. CO and NH_3 transfer electrons to graphene making it more electron rich (N-type) while NO_2 and H_2O will take electrons from graphene making it more hole rich (P-type) [5]. Considering the fact that graphene usually is slightly p-type doped through the interaction with substrate [7,23], so the conductance will vary differently depending of adsorbates. For example, adsorption of NH_3 molecules will decrease conductance of graphene while adsorption of NO_2 will increase the conductance of graphene [7]. Fundamentally, the change of conductivity results from the change of charge carrier concentration in the graphene induced by adsorption of gas molecules [15]. It is also found that graphene has no dangling bonds on its surface [6] which is unfavorable in chemical detection for sensitivity enhancement. To overcome this intrinsic drawback of graphene, lots of efforts have been made to functionalize graphene in various ways with metals, polymers or other modifiers [9,18]. For instance, platinum has been used to enhance performance of graphene in H_2 detection [19,20].

Besides various ways to functionalize graphene towards specific adsorbates, defects on graphene and substrates are also parameters affecting the sensing mechanism of graphene gas sensor. Through a principle study, Zhang et al. showed that defective graphene can strongly increase the binding energy between CO, NO and NO_2 molecules and the graphene surface, thus improving the sensing properties than pristine graphene [15]. Moreover, Yuan et al. conclude that line defects in graphene sheets can reduce conduction path and enhance sensing response [7]. A study [21] published in 2013 by Kumar et al. suggested that pristine graphene ChemFETs are not intrinsically as sensitive as defective graphene ChemFETs obtained from CVD or chemical exfoliation. They also reported defective substrates are needed to more strongly modulate the electrical properties of graphene [21]. Although in the study conducted by Kumar et al., the sensor configuration is ChemFET and the substrate is SiO_2, these findings together indicate the possibilities to control sensing properties of graphene gas sensor by engineering the substrate properties in general.

It is worth noticing that to consider graphene a suitable material to incorporate into more electronic or optoelectronic applications in the future, developing graphene-metal contacts with low contact resistance is an imperative requirement [24]. Then certainly in a graphene gas sensor system, good graphene-metal contacts are necessary. Understanding graphene-metal interactions will therefore be beneficial to improve the sensing performance. First-principles study by Giovannetti et al. [25] has reported different graphene doping effects introduced by interactions between graphene and metals such as Ni, Pd, Al, Cu, Au, and Pt. Besides engineering the substrate properties mentioned in the previous discussion, this result leads to a different way to potentially improve sensing behavior of graphene using doping effects by metals contacts. Because of this possibility, it gives motivation to incorporate the experimental study on graphene metal contact resistance in this thesis as well. Details of this part of work is presented in Chapter 5.

2.3 Conclusion and opportunities in studies of substrate materials

In section 2.1, advantages of adopting graphene as active sensing layer in gas sensor are revisited. Moreover, graphene properties and mainstream graphene fabrication method including mechanical exfoliation, chemical exfoliation and CVD are discussed.

Section 2.2 first introduces the sensing mechanisms of chem-resistor type graphene gas sensor and relevant parameters that affect the process.

In particular, the work by Zhang, Kumar et al. open interesting research opportunities for this thesis work. Effects on graphene gas sensing from differently prepared substrates are investigated, such as thermally grown, LPCVD and PECVD SiO_2.

Next, in chapter 3, specific gas sensing experiments and results will be presented and discussed to further address this topic.

References

[1] Novikov, S., Lebedeva, N., Satrapinski, A., Walden, J., Davydov, V. and Lebedev, A., 2016. Graphene based sensor for environmental monitoring of NO 2. *Sensors and Actuators B: Chemical*, *236*, pp.1054-1060.

[2] Pearce, R., Iakimov, T., Andersson, M., Hultman, L., Spetz, A.L. and Yakimova, R., 2011. Epitaxially grown graphene based gas sensors for ultra sensitive NO 2 detection. *Sensors and Actuators B: Chemical*, *155*(2), pp.451-455.

[3] Schedin, F., Geim, A.K., Morozov, S.V., Hill, E.W., Blake, P., Katsnelson, M.I. and Novoselov, K.S., 2007. Detection of individual gas molecules adsorbed on graphene. *Nature materials*, *6*(9), pp.652-655.

[4] Novoselov, K.S., Geim, A.K., Morozov, S.V., Jiang, D., Zhang, Y., Dubonos, S.V., Grigorieva, I.V. and Firsov, A.A., 2004. Electric field effect in atomically thin carbon films. *science*, *306*(5696), pp.666-669.

[5] Hill, E.W., Vijayaragahvan, A. and Novoselov, K., 2011. Graphene sensors. *IEEE Sensors Journal*, *11*(12), pp.3161-3170.

[6] Basu, S. and Bhattacharyya, P., 2012. Recent developments on graphene and graphene oxide based solid state gas sensors. *Sensors and Actuators B: Chemical*, *173*, pp.1-21.

[7] Yuan, W. and Shi, G., 2013. Graphene-based gas sensors. *Journal of Materials Chemistry A*, *1*(35), pp.10078-10091.

[8] Fuhrer, M.S., Lau, C.N. and MacDonald, A.H., 2010. Graphene: materially better carbon. *MRS bulletin*, *35*(4), pp.289-295.

[9] Singh, V., Joung, D., Zhai, L., Das, S., Khondaker, S.I. and Seal, S., 2011. Graphene based materials: past, present and future. *Progress in materials science*, *56*(8), pp.1178-1271.

[10] Zhang, Y.I., Zhang, L. and Zhou, C., 2013. Review of chemical vapor deposition of graphene and related applications. Accounts of chemical research, 46(10), pp.2329-2339.

[11] Lee, Y., Bae, S., Jang, H., Jang, S., Zhu, S.E., Sim, S.H., Song, Y.I., Hong, B.H. and Ahn, J.H., 2010. Wafer-scale synthesis and transfer of graphene films. *Nano letters*, *10*(2), pp.490-493.

[12] Zheng, M., Takei, K., Hsia, B., Fang, H., Zhang, X., Ferralis, N., Ko, H., Chueh, Y.L., Zhang, Y., Maboudian, R. and Javey, A., 2010. Metal-catalyzed crystallization of amorphous carbon to graphene. *Applied Physics Letters*, *96*(6), p.063110.

[13] Bae, S., Kim, H., Lee, Y., Xu, X., Park, J.S., Zheng, Y., Balakrishnan, J., Lei, T., Kim, H.R., Song, Y.I. and Kim, Y.J., 2010. Roll-to-roll production of 30-inch graphene films for transparent electrodes. *Nature nanotechnology*, *5*(8), pp.574-578.

[14] Vollebregt, S., Alfano, B., Ricciardella, F., Giesbers, A.J.M., Grachova, Y., van Zeijl, H.W., Polichetti, T. and Sarro, P.M., 2016, January. A transfer-free wafer-scale CVD graphene fabrication process for MEMS/NEMS sensors. In *Micro Electro Mechanical Systems (MEMS), 2016 IEEE 29th International Conference on* (pp. 17-20). IEEE.

[15] Zhang, Y.H., Chen, Y.B., Zhou, K.G., Liu, C.H., Zeng, J., Zhang, H.L. and Peng, Y., 2009. Improving gas sensing properties of graphene by introducing dopants and defects: a first-principles study. *Nanotechnology*, *20*(18), p.185504.

[16] Ricciardella, F., Vollebregt, S., Polichetti, T., Miscuglio, M., Alfano, B., Miglietta, M.L., Massera, E., Di Francia, G. and Sarro, P.M., 2017. Effects of graphene defects on gas sensing properties towards NO 2 detection. Nanoscale, 9(18), pp.6085-6093.

[17] Leenaerts, O., Partoens, B. and Peeters, F.M., 2008. Adsorption of H 2 O, N H 3, CO, N O 2, and NO on graphene: A first-principles study. *Physical Review B*, *77*(12), p.125416.

[18] Pumera, M., Ambrosi, A., Bonanni, A., Chng, E.L.K. and Poh, H.L., 2010. Graphene for electrochemical sensing and biosensing. *TrAC Trends in Analytical Chemistry*, *29*(9), pp.954-965.

[19] Shafiei, M., Arsat, R., Yu, J., Kalantar-Zadeh, K., Wlodarski, W., Dubin, S. and Kaner, R.B., 2009, October. Pt/graphene nano-sheet based hydrogen gas sensor. In *Sensors, 2009 IEEE* (pp. 295-298). IEEE.

[20] Chu, B.H., Lo, C.F., Nicolosi, J., Chang, C.Y., Chen, V., Strupinski, W., Pearton, S.J. and Ren, F., 2011. Hydrogen detection using platinum coated graphene grown on SiC. *Sensors and Actuators B: Chemical*, *157*(2), pp.500-503.

[21] Kumar, B., Min, K., Bashirzadeh, M., Farimani, A.B., Bae, M.H., Estrada, D., Kim, Y.D., Yasaei, P., Park, Y.D., Pop, E. and Aluru, N.R., 2013. The role of external defects in chemical sensing of graphene field-effect transistors. *Nano letters*, *13*(5), pp.1962-1968.

[22] Vitchev, R., Malesevic, A., Petrov, R.H., Kemps, R., Mertens, M., Vanhulsel, A. and Van Haesendonck, C., 2010. Initial stages of few-layer graphene growth by microwave plasma-enhanced chemical vapour deposition. Nanotechnology, 21(9), p.095602.

[23] Geim, A.K., 2009. Graphene: status and prospects. science, 324(5934), pp.1530-1534.

[24] Cusati, T., Fiori, G., Gahoi, A., Passi, V., Lemme, M.C., Fortunelli, A. and Iannaccone, G., 2017. Electrical properties of graphene-metal contacts. Scientific Reports, 7.

[25] Giovannetti, G.A.K.P.A., Khomyakov, P.A., Brocks, G., Karpan, V.V., Van den Brink, J. and Kelly, P.J., 2008. Doping graphene with metal contacts. Physical review letters, 101(2), p.026803.

Chapter 3. Study of Device Performance on Three Kinds of SiO_2 as Substrates

3.0 Overview

This chapter introduces the basics of gas sensing experiment in section 3.1. Details about data analysis methodology and related results are described in section 3.2 to section 3.4. At last, discussions about sensing responses are summarized in section 3.5.

3.1 Gas Sensing Experiment Setup and Environments

The gas sensing experiments presented in this thesis are carried out using the 'Gas Sensor Characteristic System' (GSCS) in the research laboratory located at ENEA research center in Italy. As reported in ref [1], the following contents in this section give a detailed description about the experiment setup and related environment. GSCS contains parts including a test chamber for device and connection to conductance measurement setup. Sensor device is placed in a test chamber able to mimic the environmental conditions in terms of temperature, humidity and pressure. In the test chamber, a total gas flow (analyte plus carrier gas) is around 500sccm. N_2 is used as carrier gas. The concentration of analyte to be detected is in the range of hundreds of ppb. The conductance of the device in its equilibrium state is measured before introducing the analyte. This result represents the so-called baseline of the measurement. Additionally, the actual analyte concentration in the chamber is checked by an Fourier-transform infrared spectroscopy (FTIR) device to ensure it is in agreement with the desired value of choice in the experiment. A work station containing the required software links the hardware in the system to automatically control and record experiment signals, environment parameters, making it possible to perform various protocols, which are essentially customized automatic measurements on devices. The chem-resistor graphene gas sensors used in this thesis are fabricated based on the wafer scale transfer-free graphene fabrication method described in [2]. In the final structure of the sensor, graphene layer with length 250um and width 5um lies directly on top of a 90nm thick SiO_2 layer and metal contacts are deposited on top of the graphene layer.

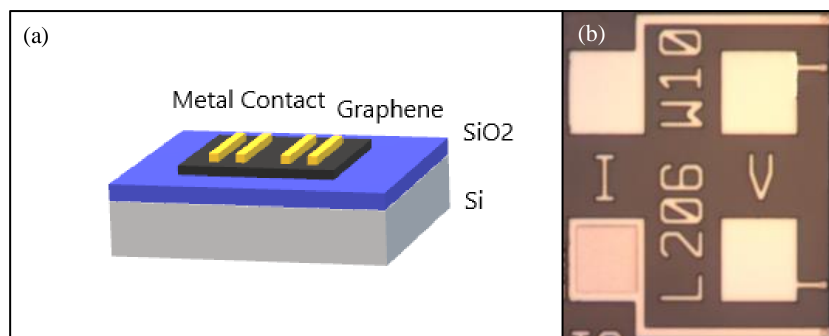

Figure 3.1(a) and (b). Schematic of graphene chem-resistor and an electrical test structure with a graphene line width of 10 µm

In this thesis work, three kinds of protocols are used as experiments. These protocols are different in terms of analyte exposure time, recovery time and analyte concentration used in each exposure. Other parameters such as relative humidity, temperature and pressure are set to be controlled and maintained throughout the experiments. Descriptions can be found in the following about the three protocols. Gas exposure profiles are presented in Figure 3.2(a)-2(c). Details about three protocols are also listed in Table 3.1.

I. Single exposure window with fixed NO_2 gas concentration of 1 ppm (Figure 3.2(a)).
II. Five repeated exposure windows with fixed NO_2 gas concentration of 1ppm (Figure 3.2(b)).
III. Multiple exposure windows with uniformly decreasing concentrations from 1500ppb to 120ppb (Figure 3.2(c)).

Exposure time is defined as a time interval during which the analyte is flowed through with a certain constant concentration. Recovery time is defined as a time window during which only carrier gas exists and the device starts restoring to the initial conditions before analyte exposure.

Protocol (I) is considered the standard sample protocol of a gas sensing measurement. It provides the basic standard sensing behavior of a device. Protocol (II) is designed as an extended version of protocol (I) and it can test the consistency of sensing behavior under multiple exposures with the same conditions. Protocol (III) is designed to investigate the effects of changing analyte concentrations on sensing behaviors. Of course, more variations of protocols can exist for sensing experiments, such as adopting a more complex analyte concentration profile. But as of now, the previous mentioned three types are of interest in this thesis.

Table 3.1. Three Protocols of Experiments

	I	II	III
Exposure Time[min]	10	10	4
Recovery Time[min]	20	10	20

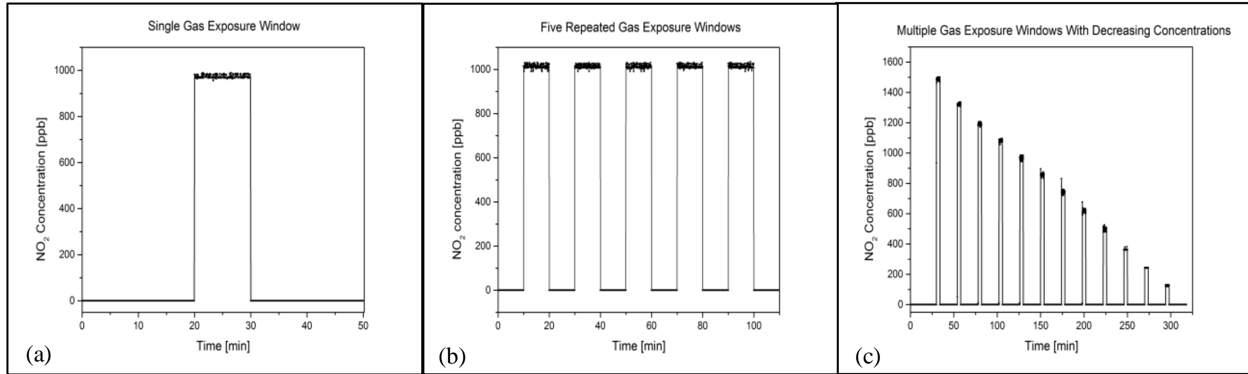

Figure 3.2(a)-(c). Gas exposure profiles.

3.2 Analysis Methodology and An Example Analysis Based on Sensing Responses from Protocol (I)

As explained in last section, experiments were carried out using three protocols. Sensing data is acquired from experiments using graphene based chem-resistor prepared on three different kinds of substrates, namely thermal oxide, LPCVD oxide and PECVD oxide. Because the methodology of analyzing the data from all experiments is similar, here it is reasonable to explain the methodology first by analyzing the data from protocol (I) which is the simplest case of a single exposure experiment.

In previous chapters the working principles of a chem-resistor has been discussed. Figure 3.3(a)-(c) present the sensing responses from sensors under protocol (I) experiments.

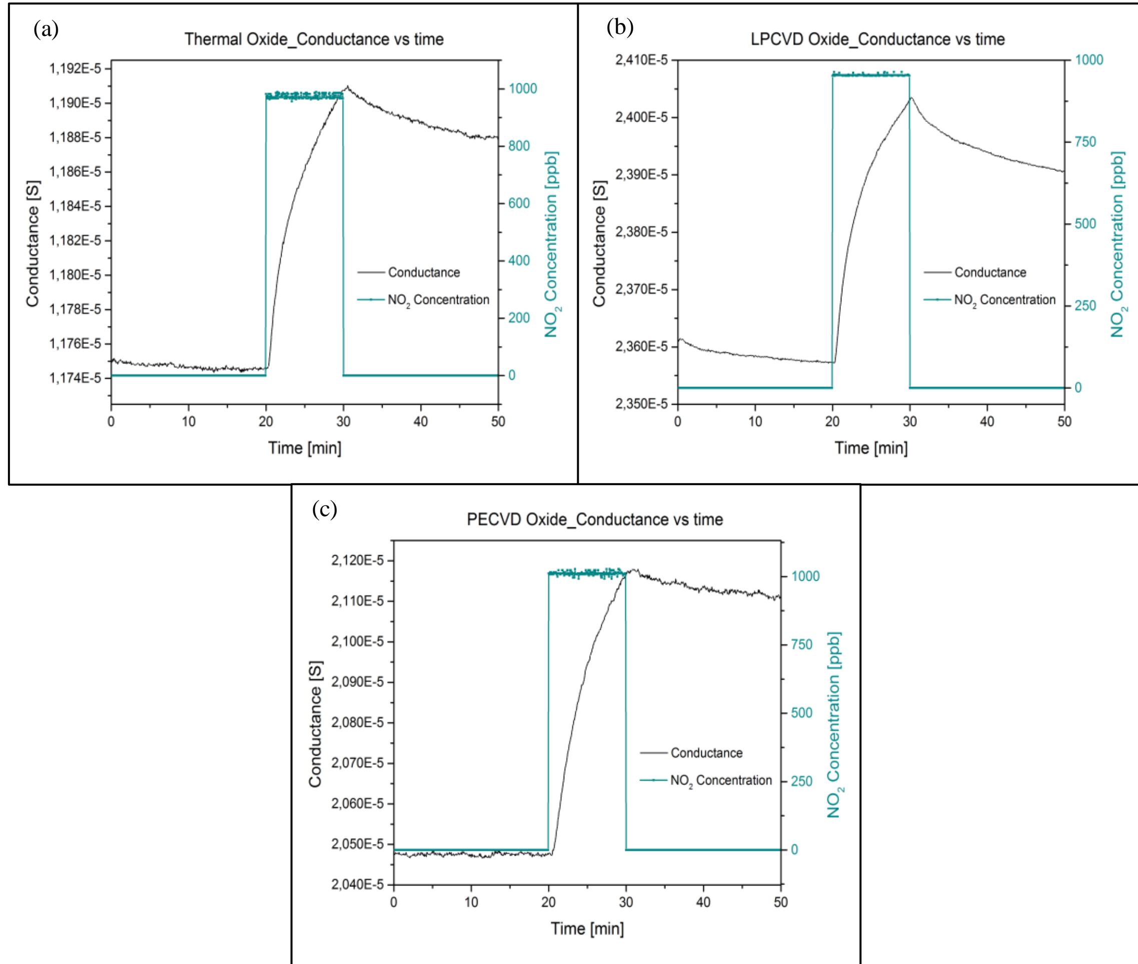

Figure 3.3(a)-(c). Sensing responses of devices using protocol (I): single gas exposure window

From Figure 3.3 it is observed that the conductance of graphene starts increasing after introducing NO_2 in the test chamber. This observation is in agreement with the discussion I did in Chapter 2, claiming that adsorption of NO_2 molecules will increase the conductivity of graphene. NO_2 concentration in all cases is maintained well at 1ppm, however, some differences in performance are observed from sensors based on thermal oxide substrate (T sensor), LPCVD oxide substrate (L sensor) and PECVD oxide substrate (P sensor).

First, the absolute values of conductance in three cases are different. For example, the conductance prior to exposure of analyte is 1.175×10^{-5} S in T sensor while in L sensor that is 2.360×10^{-5} S. It can be inferred that the difference in absolute value of conductance from device to device is caused by two reasons. First of all, data recorded from experiments show slight differences in initial chamber temperature and humidity conditions. It is reported that factors such as temperature and humidity are influencing factors in graphene based sensor device [3]. Second, the choice of substrate material is a clear difference among all three types of sensors. Therefore, although the environment in test chamber is maintained and controlled through each single experiment, small differences in starting conditions from an experiment to another will affect the absolute value of conductance. Moreover, the different choice of substrate material is another major influencing factor in these experiments.

An accepted way to compare the performance from different devices, as reported for instance by Wang et al. [4], is to look at the ratio of variation from the sensor response. In the following analysis used by this thesis, the ratio of conductance variation is given by:

$$M = \frac{\Delta G}{G_0} = \frac{G_m - G_0}{G_0} \times 100\%$$

- M: Ratio of conductance variation
- G_m: Conductance value reached during analyte exposure at a certain point of time.
- G_0: Initial value when gas exposure starts

For example, in the case of the thermal oxide based device as shown in Figure 3.4, G_m is the value of maximum conductance reached during the analyte exposure, then M = 1.369%

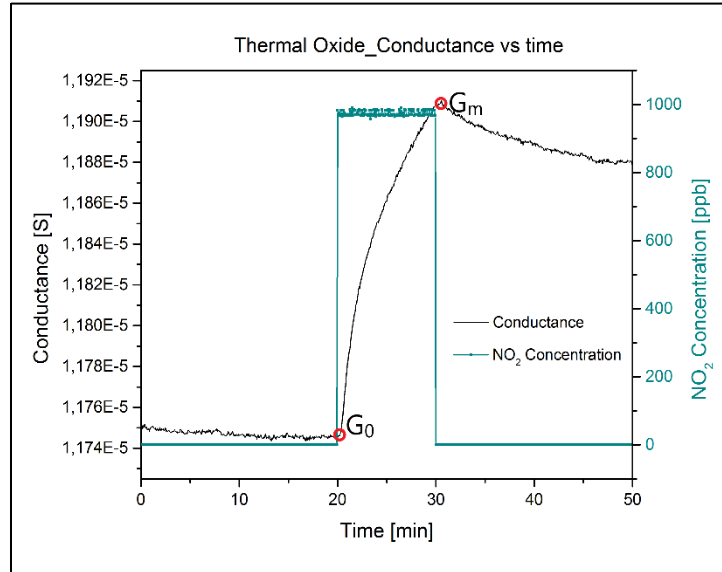

Figure 3.4. Sensing response from T sensor, Protocol (I)

The normalization of the conductance is useful in the data analysis to fairly compare responses of devices with different conductance levels. The normalized conductance in this case for the thermal oxide based device is shown in Figure 3.5.

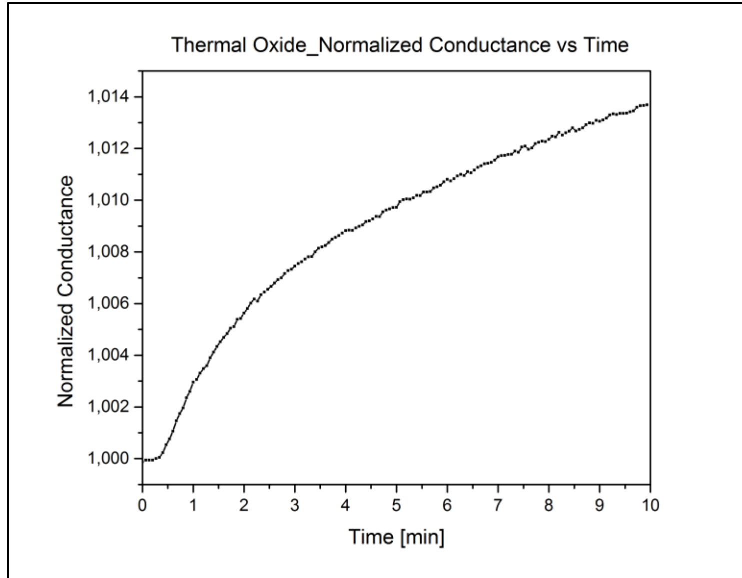

Figure 3.5. Normalized conductance of T sensor as recorded towards exposure protocol (I)

From Figure 3.5 it is able to determine how much the conductance has increased at a certain point in the experiment. The above calculation indicates that for this instance the device has a maximum conductance increment of 1.369%. Thus, normalized conductance as function of time curve reflects how the conductance increases over time in a clearer way than conductance vs time curve. Moreover, as can be observed from Figure 3.5, conductance increases much faster in the first 150s or so than in the rest of the analyte exposure time.

In order to study the rate of conductance variation in a more detailed way, the derivative of conductance vs time ($\frac{\partial G}{\partial t}$) is taken into account as shown in Figure 3.6.

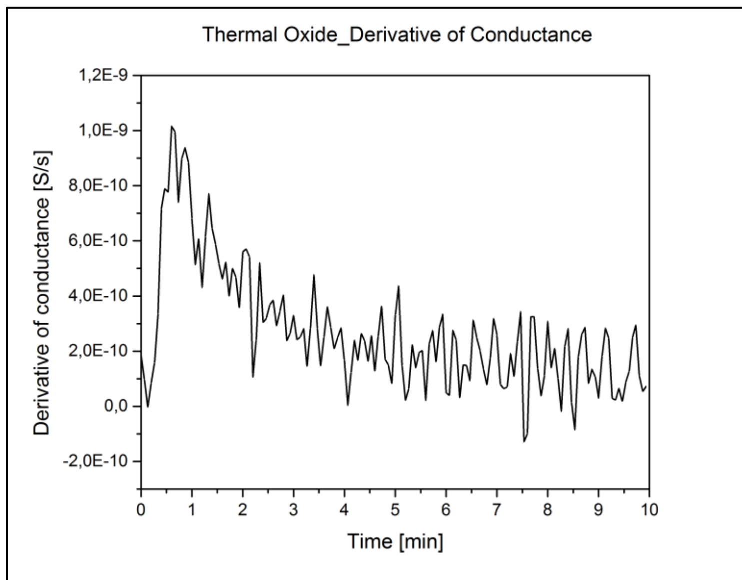

Figure 3.6. Derivative as function of time of conductance of T sensor under exposure protocol (I)

From $\frac{\partial G}{\partial t}$ curve it is observed that the rate of conductance variation increases rapidly in the first minute of experiment, reaching maximum value of 1.016×10^{-9} S/s at the time of around 20.5 mins. For sensing responses from the other two types of device, similar analysis for normalization and derivative of conductance can be applied. Results are shown in the Figure 3.7 and Figure 3.8.

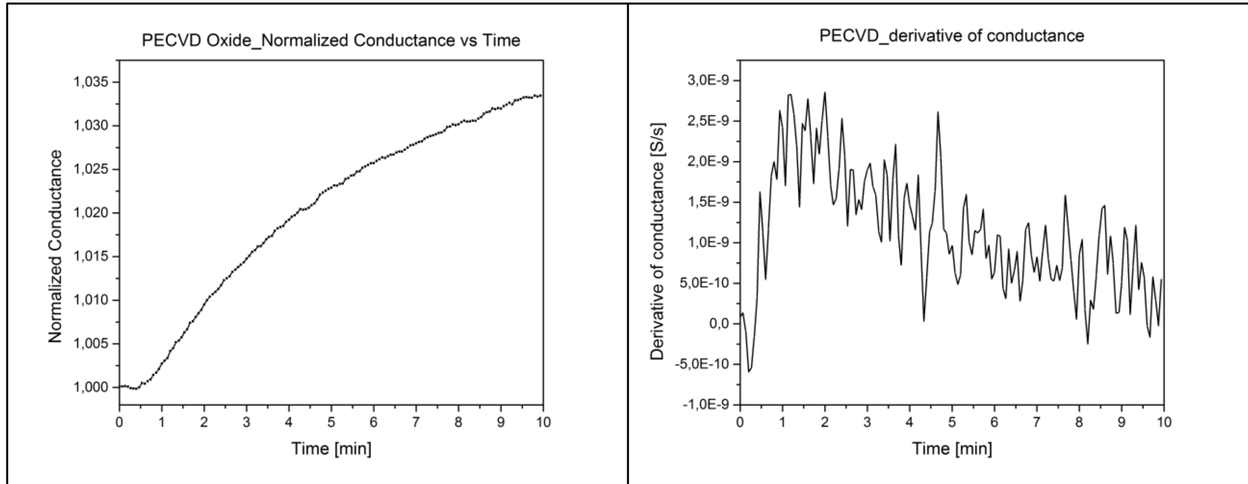

Figure 3.7. Normalized conductance and derivative of conductance as a function of time of P sensor under exposure protocol (I)

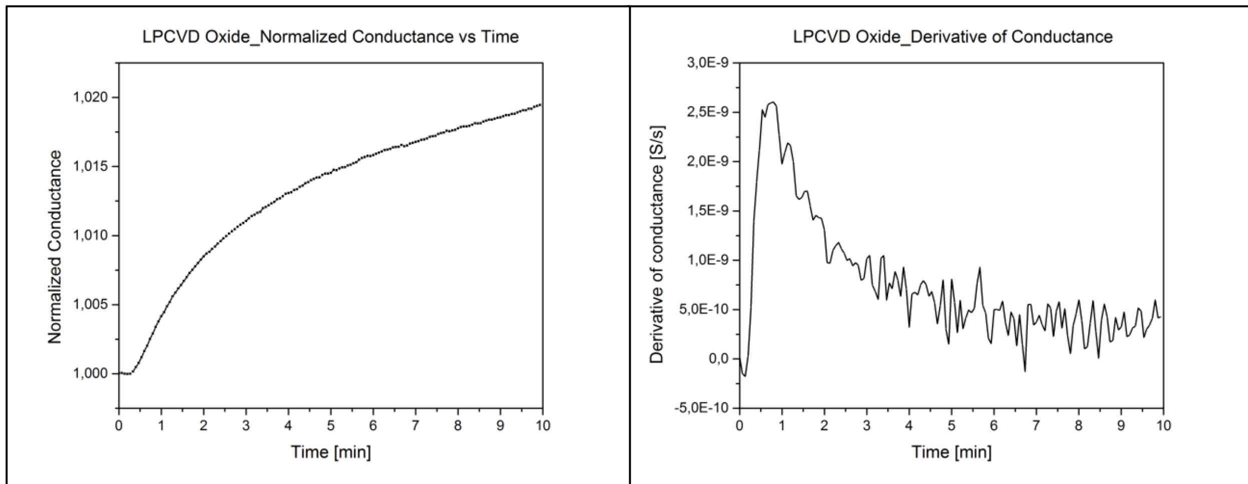

Figure 3.8. Normalized conductance and derivative of conductance as a function of time of L sensor under exposure protocol (I)

In Table 3.2 the analysis results for experiments under Protocol (I) has summarized.

Table 3.2. Summary of conductance variation, protocol (I)

	T sensor	L sensor	P sensor
M |max [%]	1,369	1,946	3,345
$\frac{\partial G}{\partial t}\|_{max}$ [nS/s]	1,016	2,604	2,858

From the above analysis, it can be concluded that device based on PECVD substrate has the largest sensing response in terms of both magnitude and rate of conductance variation. On the contrary, device based on thermal oxide substrate has the smallest sensing response and device based on LPCVD substrate acts in between of the other two types.

Comparing the derivative of conductance curves of devices based on three different substrates, it is also worth noticing that in case of PECVD, $\frac{\partial G}{\partial t}$ is noisy if it is compared to the other two cases. In fact, statistics in Table 3.3 shows that sensing data from PECVD based device has the largest standard deviation.

Table 3.3. Summary of statistics of derivative of conductance, protocol (I)

Oxide	Mean [nS/s]	Stan. Dev. [nS/s]	$\frac{\partial G}{\partial t}\|_{max}$ [nS/s]
Thermal	0,271	0,222	1,016
LPCVD	0,765	0,663	2,604
PECVD	0,114	0,761	2,858

So far, methodology of data analyzing has been introduced and sensing responses from experiments under protocol (I) have also been examined. As for experiments with five repeated analyte exposure windows---protocol (II) and multiple analyte exposures windows with decreasing concentrations---protocol (III), same analysis can be applied to compare the performance of sensing responses from devices based on thermal oxide, LPCVD oxide and PECVD oxide.

So far, methodology of data analyzing has been introduced and sensing responses from experiments under protocol (I) have also been examined. As for experiments with five repeated analyte exposure windows---protocol (II) and multiple analyte exposures windows with decreasing concentrations---protocol (III), same analysis can be applied to compare the performance of sensing responses from devices based on thermal oxide, LPCVD oxide and PECVD oxide.

3.3 Analysis of Sensing Responses from Protocol (II)

As explained in section 3.1, each experiment under protocol (II) has five identical exposure windows, with each exposure similar to experiment under protocol (I). There is a 10 minutes recovery time in between every two exposures.

The sensing responses and related normalized conductance curves are shown below in Figure 3.9-11. The derivative of conductance curves and statistics are shown below in Figure 3.12 and Table 3.5.

Combining the data from normalization curves and derivative of conductance analysis, the following table summarizes the results for each analyte exposure window in all cases:

Table 3.4. Summary of conductance variation, protocol (II)

# Exposure window	T sensor		L sensor		P sensor	
	$M\,\rvert_{max}$ [%]	$\frac{\partial G}{\partial t}\rvert_{max}$ [nS/s]	$M\,\rvert_{max}$ [%]	$\frac{\partial G}{\partial t}\rvert_{max}$ [nS/s]	$M\,\rvert_{max}$ [%]	$\frac{\partial G}{\partial t}\rvert_{max}$ [nS/s]
1st	1,380	1,278	1,310	1,913	2,175	2,975
2nd	0,753	0,741	0,801	1,329	1,087	2,049
3rd	0,663	0,581	0,686	1,128	0,811	2,193
4th	0,644	0,559	0,616	1,026	0,771	2,558
5th	0,614	0,516	0,577	1,009	0,668	2,428

Some observations can be made based on the results from Table 3.4. The case for P sensor has the largest magnitude and rate of conductance variation during experiments under protocol (II). Moreover, this trend holds for every single analyte exposure window. For T sensor the least magnitude and rate of variation is obtained whilst the case for L sensor acts in between of the other two cases. Therefore, results show that the sensing behavior of each device in protocol (II) is consistent with the behavior in protocol (I).

Additionally, analysis of derivative of conductance reveals that although the case for PECVD oxide has the largest rate of conductance variation, the standard deviation of the rate is also the largest among all three types of device. Also, the average rate of conductance variation is possible to be smaller, for example in the 5th exposure analyte window the mean of PECVD case is smaller than that of LPCVD case. Details can be found in Table 3.5.

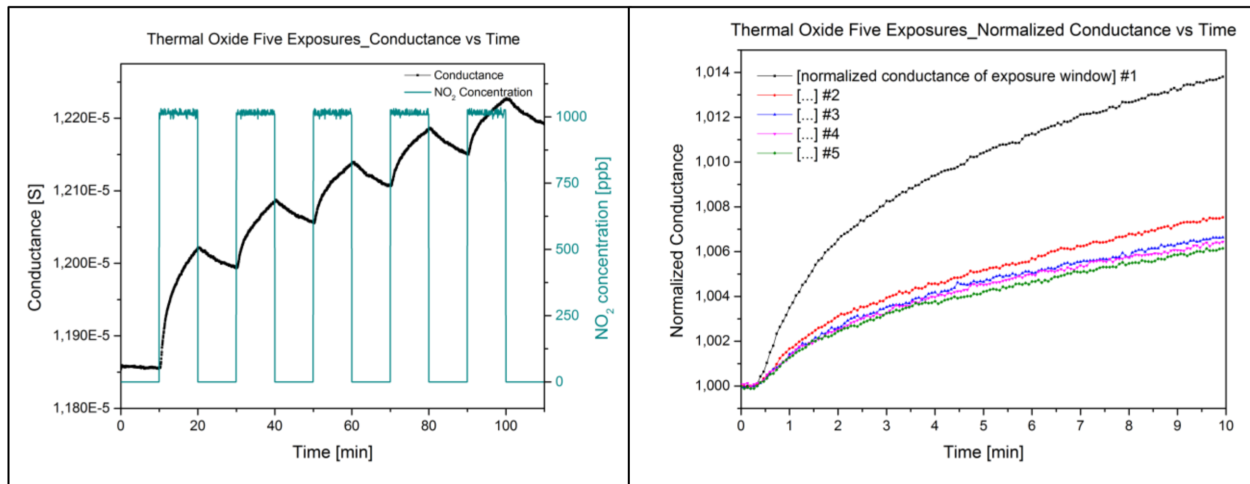

Figure 3.9. Sensing response and normalized conductance curve of T sensor under exposure protocol (II)

Another noticing fact is that for the cases of thermal oxide and LPCVD oxide, there is a common observable trend in the derivative of conductance curves. The curve reaches maximum rapidly and then gradually decreases for the rest of the analyte exposure time. However, the curve does not exhibit the similar trend in the case of PECVD oxide.

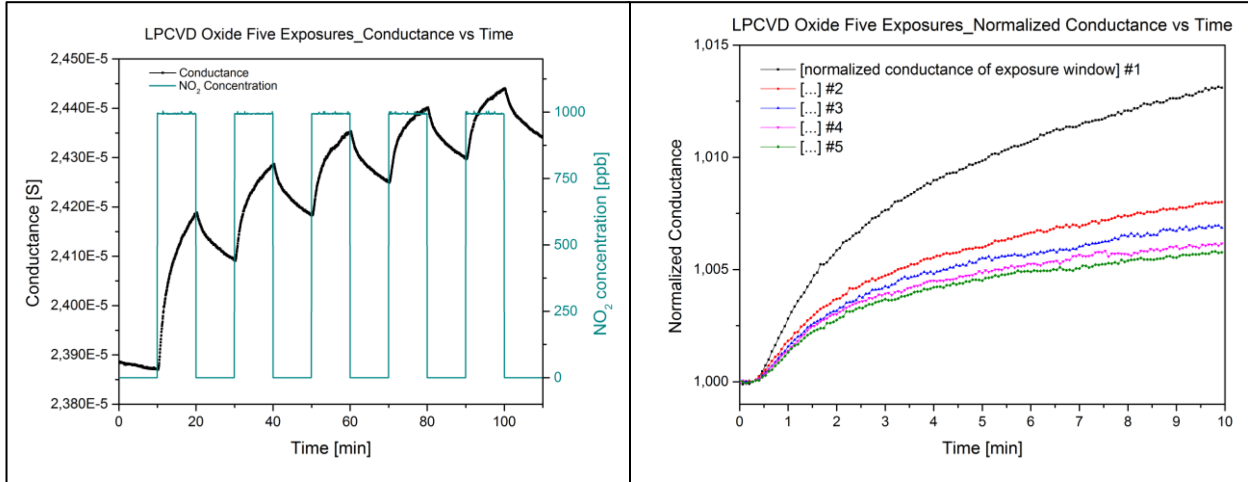

Figure 3.10. Sensing response and normalized conductance curve of L sensor under exposure protocol (II)

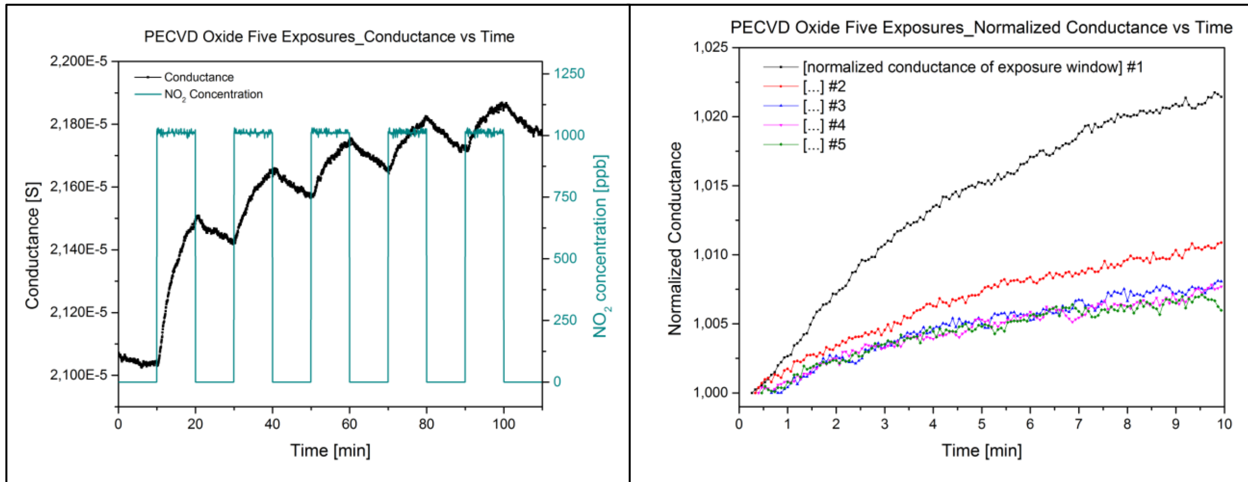

Figure 3.11. Sensing response and normalized conductance curve of P sensor under exposure protocol (II)

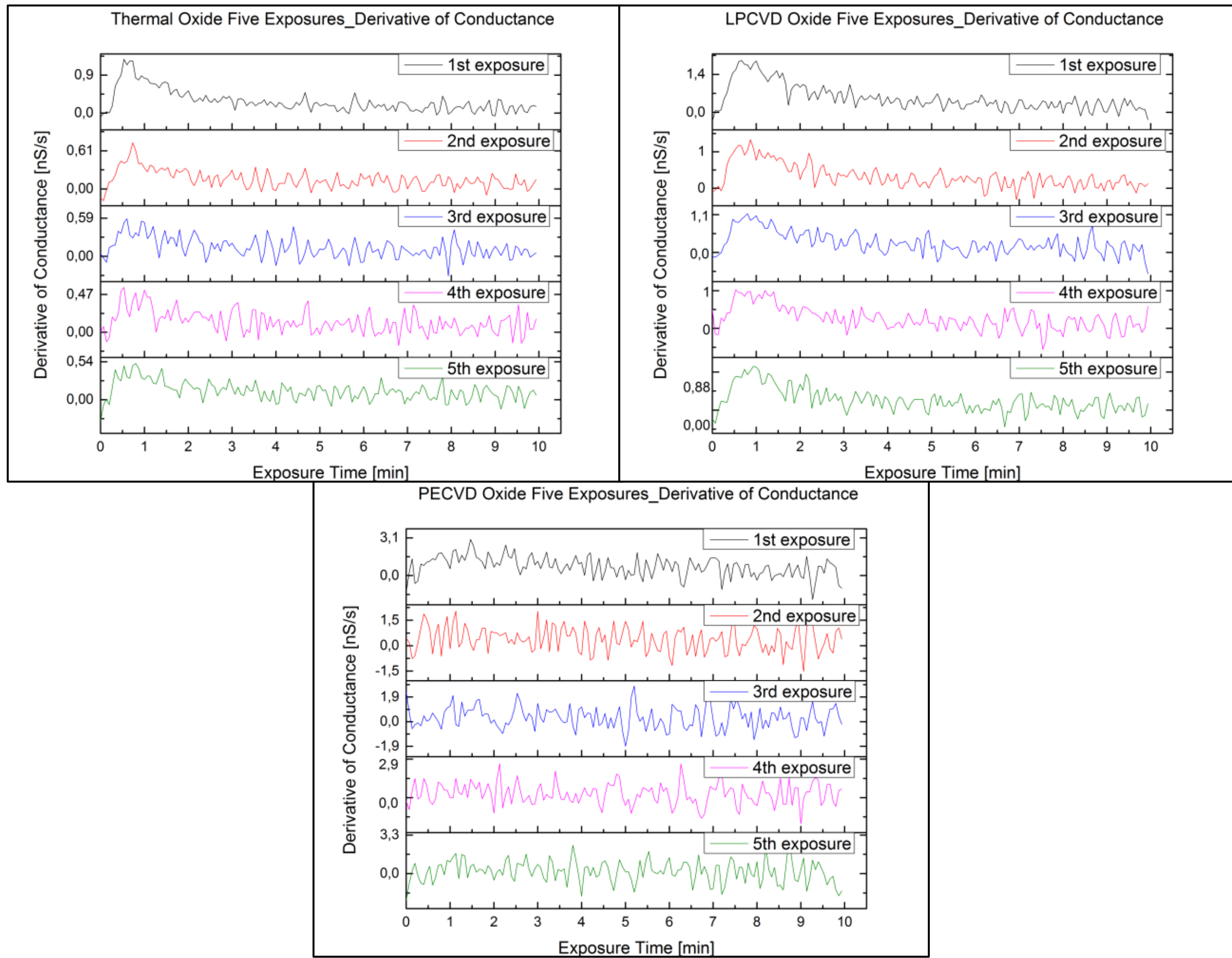

Figure 3.12. Derivative of conductance variation under protocol (II)

Table 3.5. Summary of statistics of derivative of conductance under protocol (II)

Oxide	# Exposure Window	Mean [nS/s]	Stan. Dev. [nS/s]
Thermal	1st	0,273	0,266
	2nd	0,149	0,143
	3rd	0,135	0,153
	4th	0,129	0,143
	5th	0,124	0,133
LPCVD	1st	0,521	0,475
	2nd	0,320	0,322
	3rd	0,272	0,330
	4th	0,254	0,301
	5th	0,232	0,278
PECVD	1st	0,738	0,823
	2nd	0,386	0,734
	3rd	0,309	0,848
	4th	0,288	0,807
	5th	0,176	0,943

3.4 Analysis of Sensing Responses from Protocol (III)

Protocol (III) is different from protocol (I) and (II) because the analyte concentration is not fixed at 1ppm, but decreasing gradually from 1.5 ppm down to 0.12 ppm, as shown in Figure 3.2(c). Small fluctuations around the set levels of analyte concentration can exist in every experiment, but data inconsistency due to the experiment setup is kept to be minimized and not considered to be an influencing factor of sensing results.

Following a similar methodology of analyzing used in previous sections, sensing responses and normalized conductance of devices based on different substrates are obtained and shown in Figures 3.13. Derivative of conductance are also taken for every analyte exposure window according to the methodology discussed in section 3.1. Results are summarized and presented in the following Table 3.6 and 3.7, along with a plot in Figure 3.14 presents how $\frac{\partial G}{\partial t}|_{max}$ varies against analyte concentration using data from Table 3.6.

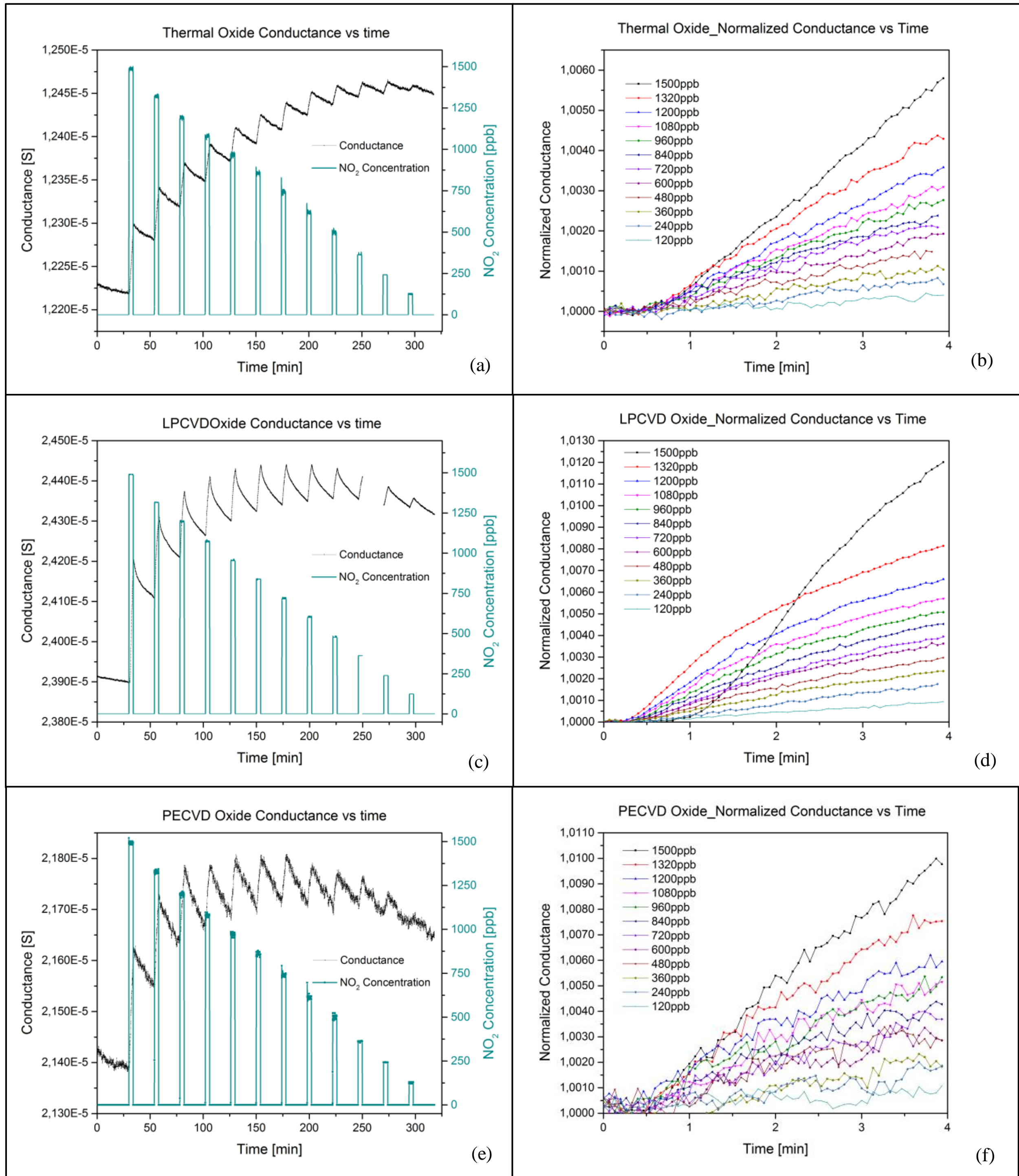

Figure 3.13. Sensing responses and normalized conductance curves of all sensors under exposure protocol (III)

Comparing among panels (a) to (f) in Figure 3.13, it is observed that the sensing response for P sensor is not as smooth as that of the other two types. From statistics shown in Table 3.7, this observation can also be explained since P sensor has the largest standard deviation from the mean at every concentration level. This point is in agreement with the observations from protocol (I) and (II).

The maximum of conductance variation in protocol (III) has a slightly different situation than what has been discussed previously about protocol (I) and (II). Previous discussions reveal that P sensor always has the maximum magnitude of conductance variation during an analyte exposure window. In this occasion, as Table 3.6 suggests, $M|_{max}$ of LPCVD is larger than that of PECVD for all concentration levels except 960ppb and 240ppb.

P sensor still owns the largest $\frac{\partial G}{\partial t}|_{max}$ for every concentration level as can be seen in Figure 3.14. However, it is observed that the spread of data is also the worst among all sensors. T sensor still has the smallest magnitude and rate of conductance variation on all concentration levels. These two points are in agreement with the observations from protocol (I) and (II).

The difference in the length of analyte exposure window is a possible reason why the case of LPCVD has the largest magnitudes of conductance variation, in other words, the means of rate of conductance variation. Each analyte exposure window in protocol (I) and protocol (II) lasts 10 minutes while in protocol (III) only 4 minutes. Suppose analyte exposure also lasts only 4 minutes in protocol (I) and (II), using existing experiment data from protocol (I) and (II), a comparison of magnitude of conductance variation can be made. From Table 3.8, it can be seen that PECVD has smaller magnitude for all cases except the 1st exposure window in protocol (I) and (II). Therefore, the difference observed in protocol (III) is not likely to be an abnormality. And if the analyte exposure length of protocol (III) is prolonged to 10 minutes, it is reasonable to infer that the maximum magnitude of conductance variation of device based on PECVD substrate could still be the largest among three types of devices. Future experiments can be conducted to prove this proposition.

It is also observed that there is a missing part in panel (c) which is out of scale due to abnormality of recorded data. In order to present the majority of the sensing response, that single part is not shown on purpose, otherwise the variation of conductance in each exposure window is not observable as shown in Figure 3.15 (out of scale part is marked in red color).

Table 3.6. Summary of conductance variation, protocol (III)

NO_2 [ppb]	T sensor		L sensor		P sensor	
	$M|_{max}$ [%]	$\frac{\partial G}{\partial t}|_{max}$ [nS/s]	$M|_{max}$ [%]	$\frac{\partial G}{\partial t}|_{max}$ [nS/s]	$M|_{max}$ [%]	$\frac{\partial G}{\partial t}|_{max}$ [nS/s]
1500	0,580	0,593	1,201	2,308	0,998	2,441
1320	0,437	0,584	0,814	1,659	0,753	3,080
1200	0,358	0,461	0,660	1,501	0,595	2,135
1080	0,310	0,541	0,570	1,533	0,515	2,656
960	0,277	0,435	0,507	1,105	0,534	2,203
840	0,238	0,338	0,453	1,056	0,427	2,141
720	0,209	0,360	0,395	0,803	0,369	2,770
600	0,193	0,404	0,362	0,915	0,286	2,703
480	0,148	0,315	0,297	0,636	0,285	2,614
360	0,113	0,444	0,235	0,516	0,182	1,579
240	0,083	0,465	0,175	0,559	0,186	1,360
120	0,040	0,324	0,093	0,366	0,107	1,510

Table 3.7. Summary of derivative of conductance statistics, protocol (III)

NO_2 [ppb]	T sensor		L sensor		P sensor	
	Mean [nS/s]	Stan.Dev. [nS/s]	Mean [nS/s]	Stan.Dev. [nS/s]	Mean [nS/s]	Stan.Dev. [nS/s]
1500	0,290	0,176	1,199	0,775	0,847	0,892
1320	0,221	0,159	0,816	0,425	0,663	0,778
1200	0,192	0,110	0,664	0,357	0,503	0,847
1080	0,162	0,153	0,578	0,346	0,510	0,943
960	0,146	0,135	0,511	0,288	0,469	0,869
840	0,127	0,101	0,463	0,248	0,354	0,818
720	0,114	0,129	0,411	0,219	0,264	0,923
600	0,101	0,112	0,360	0,233	0,231	0,854
480	0,075	0,122	0,307	0,199	0,136	1,260
360	0,049	0,142	0,239	0,155	0,110	0,647
240	0,044	0,130	0,191	0,188	0,143	0,832
120	0,026	0,113	0,080	0,163	0,057	0,663

Table 3.8 Magnitude of conductance variation for 4mins analyte exposure of L sensor and P sensor

Protocol	**# Exposure window**	**$M|_{max}$ [%]**	
		L sensor	P sensor
(I)	1st	1,030	1,326
(II)	1st	0,709	0,964
	2nd	0,447	0,422
	3rd	0,394	0,308
	4th	0,373	0,344
	5th	0,345	0,296

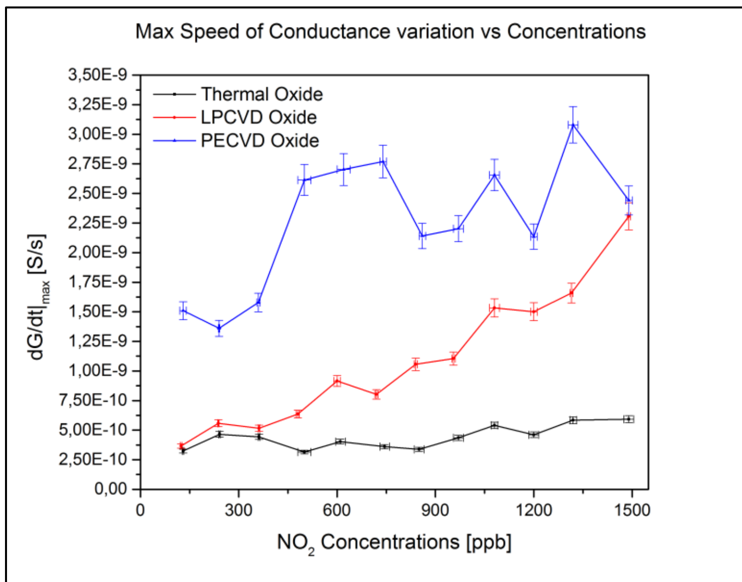

Figure 3.14. Maximum dG/dt as a function of various gas concentrations

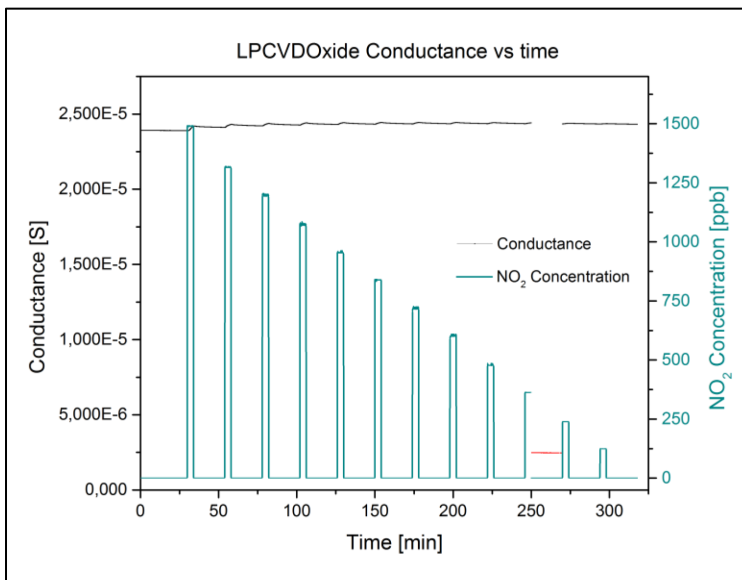

Figure 3.15. Abnormality of partial data recorded in L sensor under exposure protocol (III)

3.5 Conclusions and additional discussions

Previous sections in this chapter have introduced the setup of gas sensing experiments and discussed related sensing results. Combining observations and discussions made upon different experiment protocols, all clues point out to a central conclusion that the choice of substrate oxide material can lead to substantial difference in sensing behaviors of graphene gas sensors. Specifically speaking, the following judgements about sensing responses based on different oxide substrates can be made.

1) Sensing response is reproduceable and alike under same environment. Multiple times of analyte exposure under the same condition follow the same sensing behavior.

2) In terms of magnitude of sensing response at a certain concentration level, P sensor is the largest, L sensor is the second largest and T sensor is the smallest.

3) In terms of maximum rate of variation of sensing response at a certain concentration level, P sensor is the largest, L sensor is the second largest and T sensor is the smallest.

4) Sensing response from T sensors and L sensors exhibits much smaller spread of data than that of P sensors.

5) The rate of conductance variation tends to rapidly reach the maximum level and then gradually decay on sensing responses from T sensors and L sensors. However, rate of conductance variation from P sensors show no similar behavior.

It is especially necessary to repeat more experiments under protocol (III) in order to confirm the achieved conclusions. In the future, it will be also possible to carry out experiment with other protocols, such as mixed analyte concentrations with in a random order rather than constantly decreasing.

Seeing the differences in terms of sensing behaviors among devices based on three different oxides, in Chapter 4, material study will be introduced to find reasons to explain these differences. The material properties of three oxides will be analyzed based on capacitance-voltage relationship and Fourier-Transform Infrared spectroscopy. Related discoveries are also reported. These efforts in Chapter 4 will try to explain how different material properties of these oxide substrates lead to different sensing behaviors, providing new insights into understanding the conclusions found in Chapter 3.

References

1. Ricciardella, F., 2015. From Graphene to Graphene-Based Gas Sensors Operating in Environmental Conditions. PhD Thesis. University of Napoli "Federico II"

2. Vollebregt, S., Alfano, B., Ricciardella, F., Giesbers, A.J.M., Grachova, Y., van Zeijl, H.W., Polichetti, T. and Sarro, P.M., 2016, January. A transfer-free wafer-scale CVD graphene fabrication process for MEMS/NEMS sensors. In *Micro Electro Mechanical Systems (MEMS), 2016 IEEE 29th International Conference on*(pp. 17-20). IEEE.

3. Yuan, W. and Shi, G., 2013. Graphene-based gas sensors. *Journal of Materials Chemistry A*, *1*(35), pp.10078-10091.

4. Wang, T., Huang, D., Yang, Z., Xu, S., He, G., Li, X., Hu, N., Yin, G., He, D. and Zhang, L., 2016. A review on graphene-based gas/vapor sensors with unique properties and potential applications. *Nano-Micro Letters*, *8*(2), pp.95-119.

Chapter 4. Material Study of Thermal, LPCVD, PECVD SiO_2 Substrates

4.0 Overview

This chapter discusses some material properties about SiO_2 and related way to characterize these properties. In order to provide useful information to understand the effects of different silicon dioxide substrates on gas sensing behaviors, Capacitance-Voltage (C-V) measurements and Fourier-Transform Infrared Spectroscopy (FTIR) measurements are taken. Section 4.1 introduces some of the fabrication details and a general comparison of quality among thermal, LPCVD and PECVD oxide. Section 4.2 discusses C-V measurements and results. Section 4.3 reports FTIR measurements and results. Additionally, section 4.4 includes a concise Raman analysis of the few layer graphene (FLG) used in this thesis, complementing the material study in section 4.2 and 4.3. In section 4.5, conclusions on oxide material properties and their effects on graphene gas sensor response are reported.

4.1 Substrate Material Fabrication and Related Experiment Setup

In Chapter 3, differences in sensing behavior from devices based on thermal oxide, LPCVD oxide and PECVD oxide substrates have been observed. Results from gas sensing experiments are analyzed and discussed as well. To investigate deeper into the possible reasons behind different sensing behaviors, material study of these differently prepared oxide substrates is carried out by using C-V and FTIR measurements.

C-V measurement is a useful and widely applied technique to characterize semiconductor material and C-V measurement is a useful and widely applied technique to characterize semiconductor material and devices, such as Metal-Oxide-Semiconductor capacitor (MOSCAP), Metal-Oxide-Semiconductor Field Effect Transistor (MOSFET) and Bipolar Junction Transistor (BJT). By applying C-V measurements on hereby presented three different kinds of oxides, it is able to discover useful information about the electronic properties about them. Besides digging electronic properties from C-V measurement, FTIR measurement can provide extra information in terms of detailed chemical composition and structures about these oxide substrates. In the end, combining results from C-V and FTIR measurements, more credibility will be added into the process of determining the quality of oxide materials. Thus, it will be beneficial to understand reasons behind differences in sensing behaviors from devices based on these three differently prepared oxide substrates.

To test on the three kinds of oxide substrates, separate test structures for C-V measurement and FTIR measurement are fabricated. Brief descriptions and discussions about the fabrication processes are reported in the following. The oxide growth part in C-V and FTIR test structures is the same. Special attentions are paid to some differences in the fabrication flow of thermal, LPCVD and PECVD oxides.

(1) The fabrication flow of C-V structure consists of the following steps (see Appendix B for details):

- Starting material is single side polished p-type <100> 4-inch wafers. Resistivity: 2-5 Ω•cm
- Grow 90nm thick thermal oxide, LPCVD oxide and PECVD oxide layer on individual wafers
- Heat wafers to 1000°C in Aixtron BlackMagic Pro machine to mimic graphene growth step (Appendix A)
- Deposit 675nm Al layer in frontside of wafers; Clean backside oxides and deposit 2075 nm Al layer on backside of the wafers
- Fabricate test structures using lithography, as reported in Figure 4.1
- Etch excess Al.
- Clean wafers with deionized (DI) water then spin dry wafers. Store wafers for measurements

Final cross section structure is shown in the following schematic. The radius of each finished MOSCAP structure is 500um.

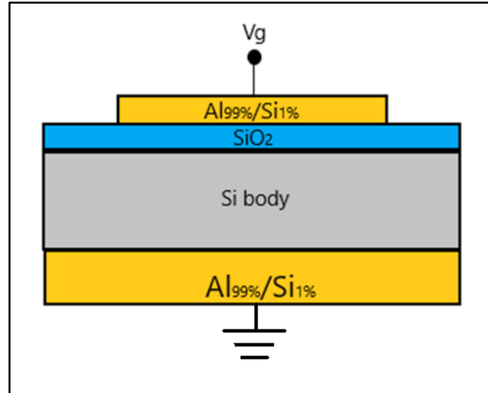

Figure 4.1. Schematic of a MOSCAP structure used in C-V measurements

(2) The fabrication flow of FTIR structure consists of the following steps:

- Starting material is single side polished n-type <100> 4-inch wafers. Resistivity: 2-5 Ω•cm
- Grow 90nm thick thermal oxide, LPCVD oxide and PECVD oxide layer on individual wafers
- Heat wafers to 1000°C in Aixtron BlackMagic Pro machine to mimic graphene growth step (Appendix A)
- Clean wafers with deionized (DI) water then spin dry wafers. Store wafers for measurements

Thermal oxide used in this thesis study is grown by dry thermal oxidation at 1050°C. A schematic of horizontal oxidation furnace is shown in Figure 4.2. Thermal oxidation is a slow process, but offers superior oxide quality than deposited CVD oxides [1]. For dry oxidation process, the following chemical reaction takes place:

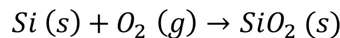

$$Si\ (s) + O_2\ (g) \rightarrow SiO_2\ (s)$$

Under the force of diffusion, oxygen atoms will diffuse into silicon structure to form silicon dioxide. Thermally formed silicon dioxide has a glassy structure in comparison to perfect crystalline quartz and unlike perfect structure, some oxygen atoms are not bonded to silicon, leaving unbonded charged oxygen atoms [1].

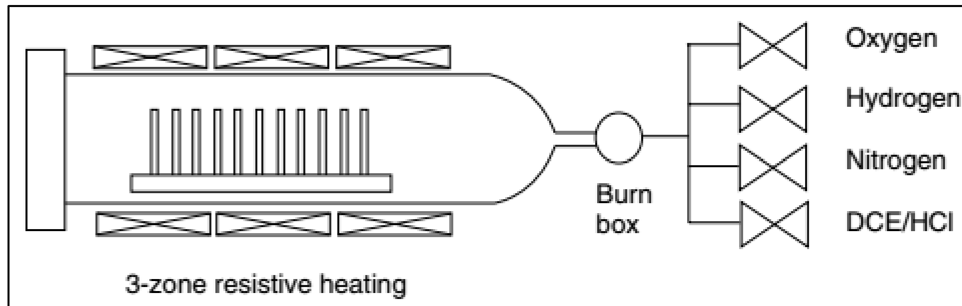

Figure 4.2. Horizontal oxidation furnace. Wafers are vertically loaded in quartz boats [1]

Fabrication of oxide using LPCVD and PECVD processes is very different from the thermal oxidation process. LPCVD reactor is similar in structure to the oxidation furnace shown in Figure 4.2. In CVD

process, source materials are in gaseous form and brought into the vicinity of the wafer substrate to react or decompose under either the influence of temperature (LPCVD) or plasma (PECVD) [1]. A schematic of CVD process is shown in Figure 4.3 below.

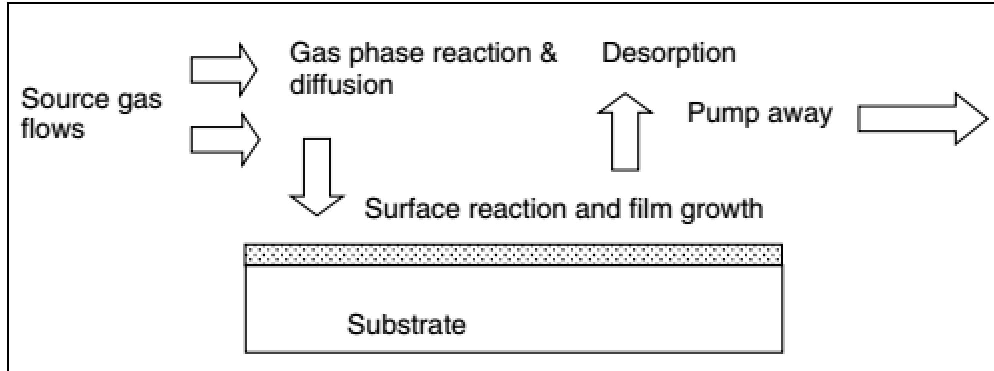

Figure 4.3. Schematic of chemical vapor deposition process [1]

In LPCVD process, oxide used in this thesis is made by Tetraethyl Orthosilicate (TEOS) at 650°C. TEOS decompose into silicon dioxide and the by-product is Diethyl ether.
In PECVD process, SiO_2 is formed by reaction of Silane (SiH_4) and Nitrous oxide (N_2O) and the by-product is Hydrogen (H_2) and Nitrogen (N_2) . The following chemical reaction takes place:

- LPCVD: $Si(OC_2H_5)_4\,(g) \rightarrow SiO_2\,(s) + 2\,(C_2H_5)_2O\,(g)$
- PECVD: $SiH_4\,(g) + N_2O\,(g) \rightarrow SiO_2(s) + H_2(g) + N_2\,(g)$

The large-scale adoption of SiO_2 in semiconductor industry has good reasons and historical roots [2]. Numerous investigations have been published to research about the electrical, chemical, structural properties of SiO_2 prepared by different methods and tested under various conditions. These study results can be found through literature search conveniently. A good handful studies, for example as shown in [3-9], are selected in this thesis work for comparison of experimental with historical data and, in addition, as references for analysis.

Generally, as reported by Pliskin [2], because of its superior reproducibility and chemical stability, thermal oxide can serve as a standard for comparison between SiO_2 films deposited by other techniques. thermal oxide is the closet to properties of perfect crystalline SiO_2 except a slightly open structure. Various other deposition techniques are developed to meet different fabrication requirements, such as low thermal budget, and they lead to films which are more porous or less dense than thermal grown oxide. Also, according to Shokri [5], pure silicon dioxide films were difficult to be deposited at a low temperature and films deposited at low temperatures contain many impurities. From the above perspectives, it is reasonable to infer that in terms of film quality, thermal grown oxide is the best among thermal, LPCVD and PECVD oxides. Additionally, it has been reported that TEOS process provides better film properties than those obtained from silane chemistry [8], therefore in terms of quality, the LPCVD TEOS oxide should have better film properties than the PECVD SiH_4 based oxide used in this thesis work. More detailed descriptions and analysis about the properties of these three oxides are introduced in the following sections 4.2 - 4.3.

4.2 Characterization of substrate materials by C-V measurements

Since MOS capacitors are useful tools to indicate the parameters of oxide quality and judging its performance, in order to characterize the quality of three oxide samples, MOS capacitors are fabricated and measured. The MOS capacitor structure is shown in Figure 4.1. When the front side of the wafer is connected to gate voltage V_g and the back side connected to ground, certain capacitance will form between the two conducting plates separated by the oxide layer, depending on the gate voltage and charges inside the oxide. Since p-type wafers are adopted for fabrications, the majority carriers are holes, so that under the electrical field formed by a negative gate voltage and ground, holes will accumulate at the Si-SiO_2 interface region. If gate voltage is positive, holes will repel from Si-SiO_2 interface region, gradually causing a depleted layer of charges. Suppose the gate voltage keeps increasing, eventually the concentration of electrons will be larger than holes, resulting in an inversion layer at the Si-SiO_2 interface. The above-mentioned processes are referred to as the accumulation, depletion and inversion of the capacitance-voltage relationship, as presented by Figure 4.4 below.

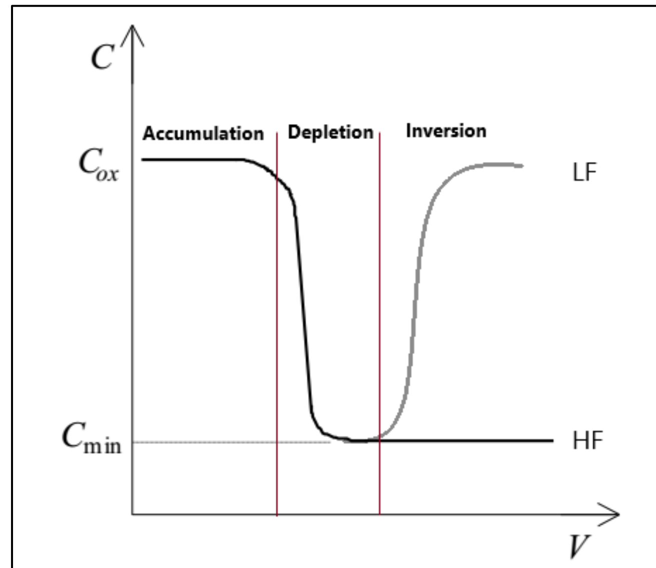

Figure 4.4. Ideal high frequency and low frequency C-V relationships

The capacitance voltage relationships allow useful information of oxides to be determined, such as relative permittivity (ε_r) and fixed oxide charge (Q_f). Figure 4.4 also indicates that the C-V relationships under low frequency and high frequency of gate voltage is different. However, as reported by Hu [10], low frequency measurement, such as at hundreds of Hz or even lower, has lost practical meaning due to technology advancement and the high quality of semiconductor material used today. Therefore, in the analysis adopted in this thesis work, also only results of high frequency analysis are examined in the following discussions. The C-V measurements are performed on probe stations with source measurement units connected to Agilent 4156C Precision Semiconductor Parameter Analyzer. The setup is controlled and driven by Agilent ICCAP software on a dedicated workstation. Each oxide sample is measured at 5 regions spread uniformly across the wafer to minimize error, as indicated by Figure 4.5.

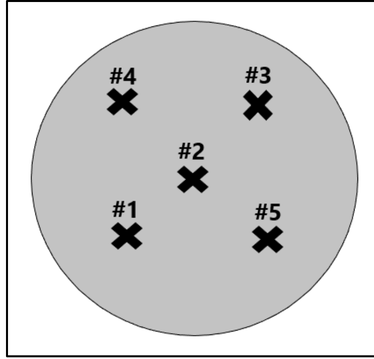

Figure 4.5. Locations for C-V measurements on a test wafer

From the obtained C-V measurement results, fixed oxide charge of each oxide sample is calculated. The detailed process will be presented in the following discussion.

C-V curves of SiO_2, LPCVD oxide and PECVD oxide are shown in Figure 4.6 below. Note that because in the probe station the electrodes for gate and ground are reversed from the conventional setup, so that during experiment, a negative gate voltage is in fact a positive voltage at the gate.

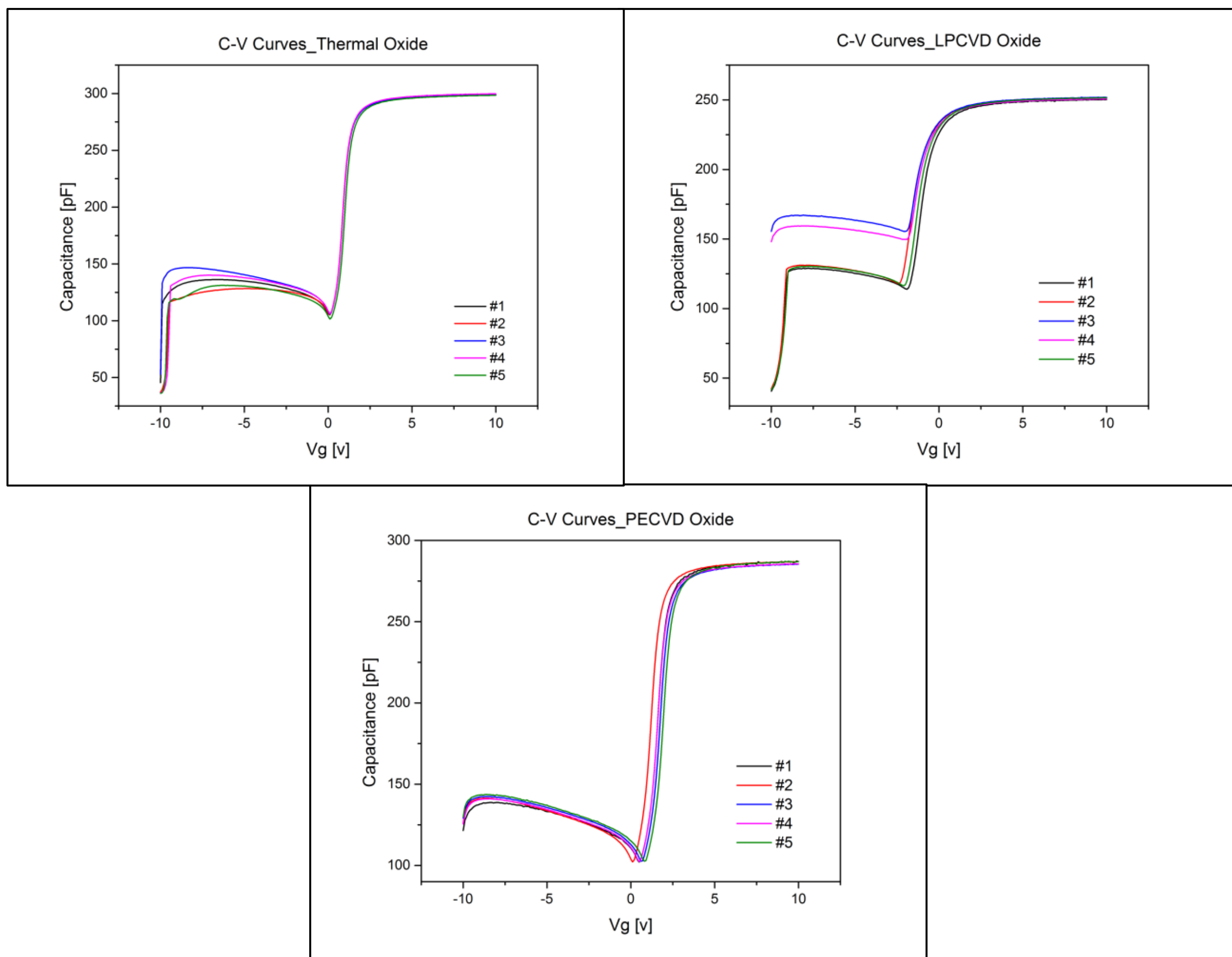

Figure 4.6. C-V relationships of thermal, LPCVD and PECVD oxide

In the process of interpreting the C-V relationship, an important occasion to understand is the flat band condition reached under gate voltage $V_g = V_{FB}$. At flat band condition, there is no accumulation or depletion at the interface of $Si\text{-}SiO_2$. Figure 4.7 presents the energy band diagram of the MOSCAP at flat band condition [10].

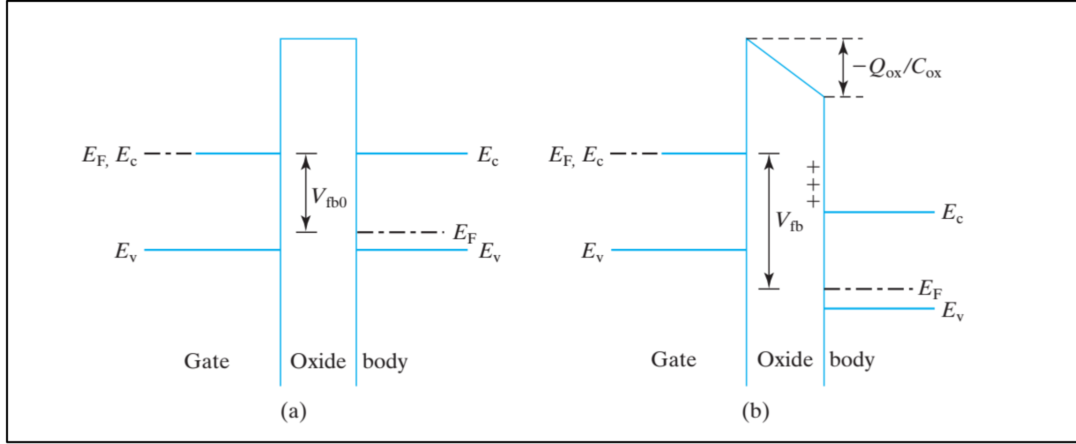

Figure 4.7. Energy band diagram of MOSCAP at flat band condition with (b) and without (a) fixed oxide charge [10]

For the analysis of this work, it is accepted to assume that most of the fixed oxide from the bulk will be concentrated at the $Si\text{-}SiO_2$ interface [10]. Ideally in a perfect oxide layer without the fixed oxide charge (Q_{ox}), as suggested by Hu [10], the flat band condition of a MOSCAP is just the work function difference (φ_{ms}) between substrate Si and gate metal (Figure 4.7(a)), which is Al the metal in the examined case. Since fixed oxide charge exists in real material, then an extra voltage drop is produced (Figure 4.7(b)), therefore, the flat band voltage becomes:

$$V_{FB} = \varphi_m - \varphi_s - Q_{ox}/C_{ox} \quad \text{(eq.1)}$$

Then in order to calculate Q_{ox}, it is essential to figure out the flat band voltage from obtained C-V relationships. Although V_{FB} is not obvious to see directly from features of C-V curves, it is possible to identify V_{FB} from its corresponding flat band capacitance C_{FB}. According to the analysis in ref [10-12], flat band capacitance equals to

$$C_{FB} = \frac{C_{max}}{1+\frac{(C_{max}/C_{min})-1}{2\sqrt{\ln(N_A/n_i)}}} \quad \text{(eq.2)}$$

where C_{max} also known as C_{ox} is the maximum capacitance obtained during C-V measurement. C_{min} is the minimum capacitance. N_A is the doping concentration of the acceptor in the p-type wafer and n_i is the intrinsic carrier concentration of the semiconductor. It is known that for the wafers used in this work, N_A is approximately 4.97×10^{15} cm^{-3} and n_i is 1.45×10^{15} cm^{-3}.

Therefore, combining the obtained data from all locations of three oxide samples and using eq.1 and eq.2, the final results are calculated as shown in Table 4.1.

Table 4.1. Summary of C-V measurement results

Oxide Type	Location	C_{max} [pF]	C_{min} [pF]	C_{FB} [pF]	V_{FB} [v]	Q_{ox} [10^{10} e/cm^{-2}]	Absolute average Q_{ox} [10^{10} e/cm^{-2}]
Thermal	#1	299	105	237	-1.08	3.19	3.72
	#2	299	105	237	-1.08	3.19	
	#3	299	106	238	-1.10	3.54	
	#4	299	106	238	-1.09	3.36	
	#5	298	102	235	-1.20	5.31	
LPCVD	#1	250	114	214	0.40	-23.0	22.8
	#2	251	118	217	0.75	-29.2	
	#3	252	155	232	0.12	-18.5	
	#4	251	150	229	0.10	-17.7	
	#5	251	116	216	0.57	-26.0	
PECVD	#1	287	102	229	-1.88	17.3	17.5
	#2	287	102	229	-1.48	10.3	
	#3	285	103	228	-2.02	19.8	
	#4	286	102	228	-1.87	17.1	
	#5	287	103	230	-2.20	23.0	

From the calculated results, it is observable that thermal oxide sample has the smallest fixed oxide charge, which is an order of magnitude smaller than that of LPCVD or PECVD oxide. In addition, LPCVD sample has the absolute value fixed oxide charge larger than that of PECVD oxide sample.

Comparison of the fixed charge implies that inside LPCVD and PECVD sample, there are much more impurities than in thermal oxide sample. Thus, we can conclude that the oxide quality of thermal oxide is the best among all three examined oxides.

4.3 Characterization of substrate materials by FTIR measurements

Apart from C-V measurements to characterize the oxide property, FTIR is another effective and widely applied material analyzing technique to determine structural properties [9]. The Fourier transform spectroscopy technique is based on the concept of a Michelson interferometer. As shown in Figure 4.8, a Michelson interferometer contains a light source (a monochromatic light source is preferred), a beam splitter, a fixed mirror, a moveable mirror and a detector.

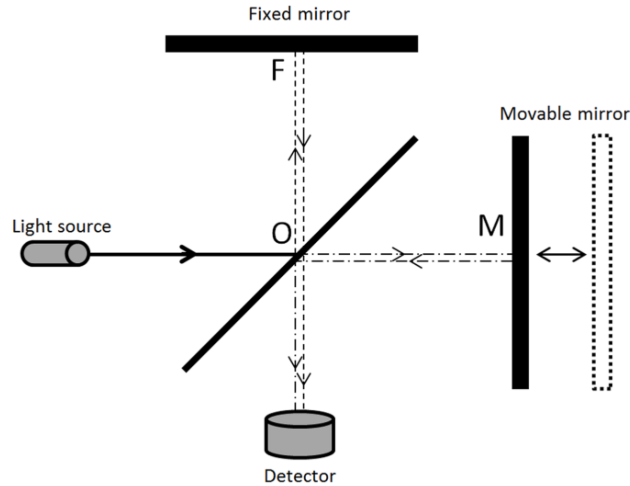

Figure 4.8. A schematic of the Michelson interferometer. The dashed line represents the reflected and transmitted light path, with arrows showing directions [20]

A beam of light with wavelength λ or wavenumber k = 1/ λ from the source will split, while part being transmitted and the other part being reflected. Then a beam of reflected light and a beam of transmitted light will reach a fixed mirror and a movable mirror respectively. Once again, two beams of light will all reach the beam splitter and partly being transmitted and the other part being reflected. In the end, portions of light will go back to the light source, which is of no interest, while the other portions of light are go to the detector being either constructively interference or destructively interference, depending on the difference of beam distance (OM-OF). Suppose the movable mirror has a constant velocity, the interference pattern is in the end a function of the wavenumber k [13]. Therefore, a spectrum as a function of wavenumber k can be generated to describe the interference pattern.

In real FTIR technique, the sample of interest will be put in between the detector and the beam splitter. The sample will distort the signal intensity measured at the detector in a way related to the various vibration modes of different atomic bonds in the sample [13]. Multiple measurements are repeated to reduce noise of the spectrum. In this way, the intensity and wavenumber position of different peaks in a FTIR spectrum can provide useful information to indicate the existence and quantity of certain atomic bonds. Such results are powerful tools to determine chemical composition and structural properties of a material.

In this thesis work, all FTIR measurements are carried out by a Thermo Scientific Nicolet 5700 spectrometer which is connected through USB to a dedicated workstation with OMNIC data processing software. The light source is an Ever-Glo infrared lamp. A DTGS detector, KBr beam splitter and a He-Ne laser for position tracking of the moving mirror are included in the spectrometer. The measurements are carried out in the spectral range 400-4000 cm^{-1}. All samples to be measured in the spectrometer will be firstly cleaned with HF dip to remove native oxide and then purged with N_2 for 15 minutes in the spectrometer to remove contaminants like water vapor. A complete measurement of the oxide sample

contains two sub measurements. Before measuring the oxide sample, a reference measurement of the same n-type wafer sample without oxide growth is taken. The spectrometer will automatically switch holders between the reference sample and the actual sample. By taking the reference measurement, the spectrum of the n-type body of the wafer is taken into account. Then, through OMNIC software, the spectrum as a reference is automatically eliminated from the spectrum obtained from the subsequent oxide sample measurement. The final result can be shown in transmittance mode or absorption mode by user's choice of interest. A typical spectrum of SiO_x layer is shown below.

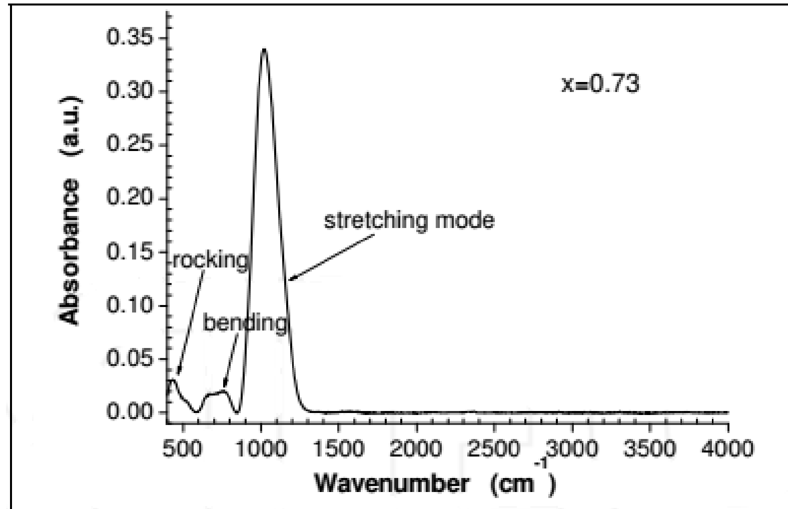

Figure 4.9. IR spectrum of SiO_x layer with x=0.73 [21]

As Figure 4.9 suggests, there are three vibration modes existing for SiO_x layer, namely, rocking, bending and stretching mode. In a SiO_2 film, these three characteristic bands also exist and are generally referred to as the Si-O-Si rocking mode, O-Si-O bending mode and Si-O stretching mode, despite some differences in annotations and naming habits are present in literature [5,8,9]. It would be beneficial at this moment as well to know some basics about SiO_2 structure to better understand these three characteristic modes and any discussion to be addressed in the following contexts.

In both crystalline and amorphous SiO_2, the fundamental building block is the SiO_4 group with a silicon place in the center of a cage of oxygen atoms [9]. As shown in Figure 4.10, the structure has tetrahydric coordination for crystalline SiO_2 while for amorphous SiO_2 the tetrahedron is distorted and some bonds can be unsaturated [9].

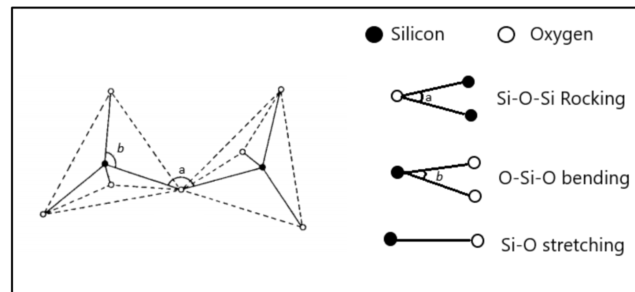

Figure 4.10. Adjacent SiO_4 units sharing an oxygen ion

In Figure 4.11 the result of raw FTIR spectra of three oxides in absorbance mode is presented.

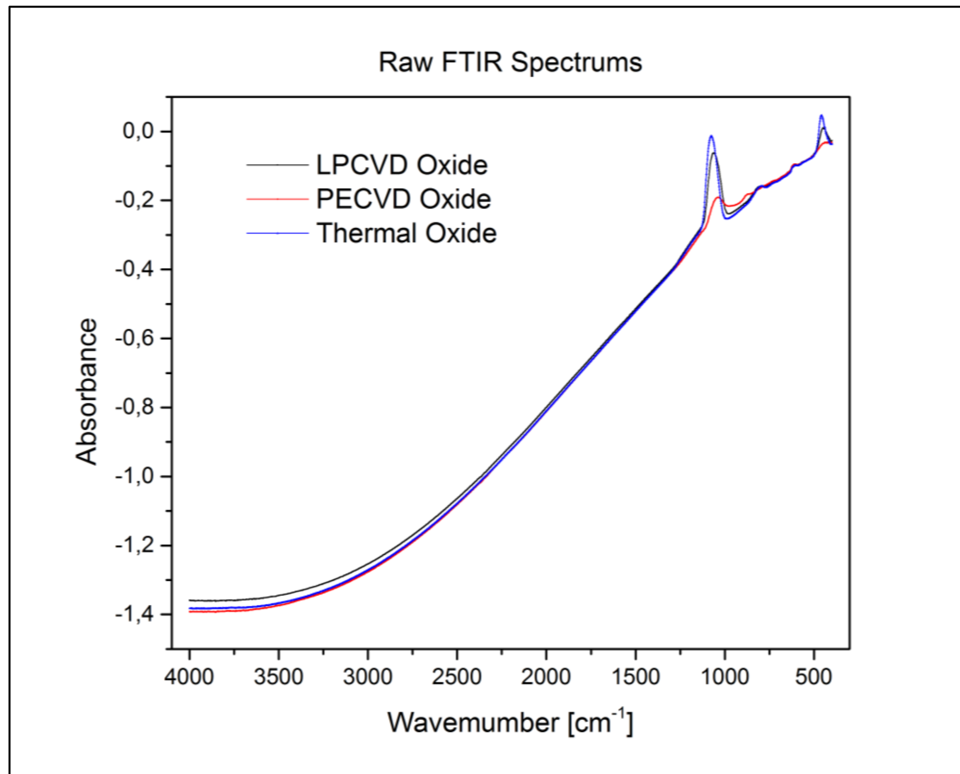

Figure 4.11. Raw FTIR spectrums of three oxides

From the raw spectra, observable peaks are located in the wavenumber range 400-1500 cm^{-1}. No peaks exist within wavenumber range3000-4000 cm^{-1} and detail examination of spectra support this observation. Therefore, the spectra of the first wavenumber range are of interest for next step analysis.

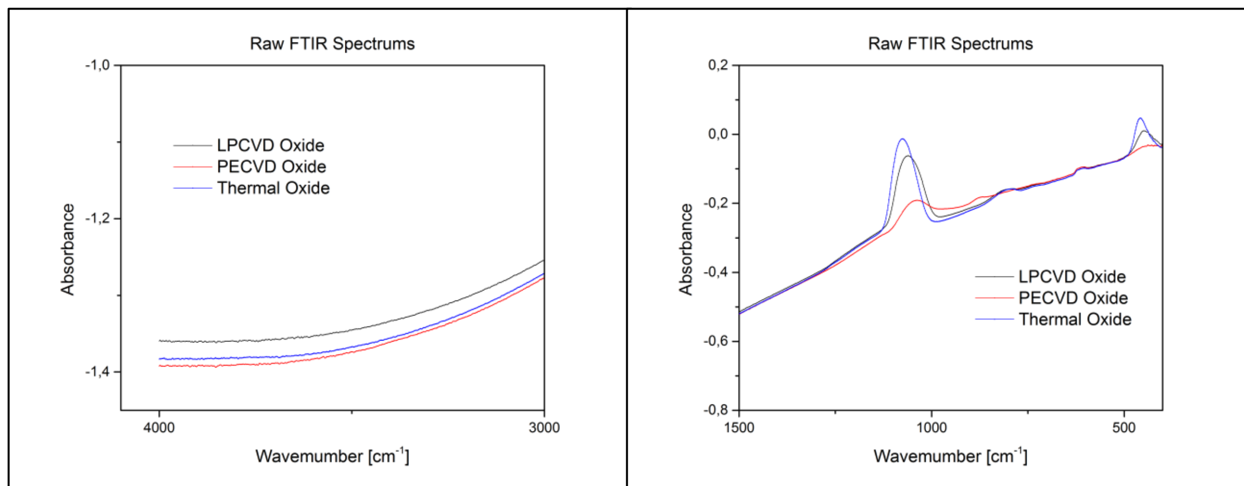

Figure 4.12. Closer examination of raw spectrums at low and high ranges

The background wave caused by the internal reflection of the oxide film is contained in each spectrum. Taking the spectrum of thermal oxide as example and adopting a similar processing technique used in ref [13,15], the background wave at around 1100 cm^{-1} peak is removed by a linear fit curve from 1140 cm^{-1} to 1000 cm^{-1}; the background wave at around 800 cm^{-1} peak is removed by a linear fit curve from 860 cm^{-1}

to 750 cm^{-1}; the background wave at around 600 cm^{-1} is removed by a linear fit curve from 640 cm^{-1} to 580 cm^{-1}; the background wave at around 450 cm^{-1} is removed by a linear fit curve from 500 cm^{-1} to 400 cm^{-1}. In Figure 4.13, a comparison of spectrum before and after removing background is shown.

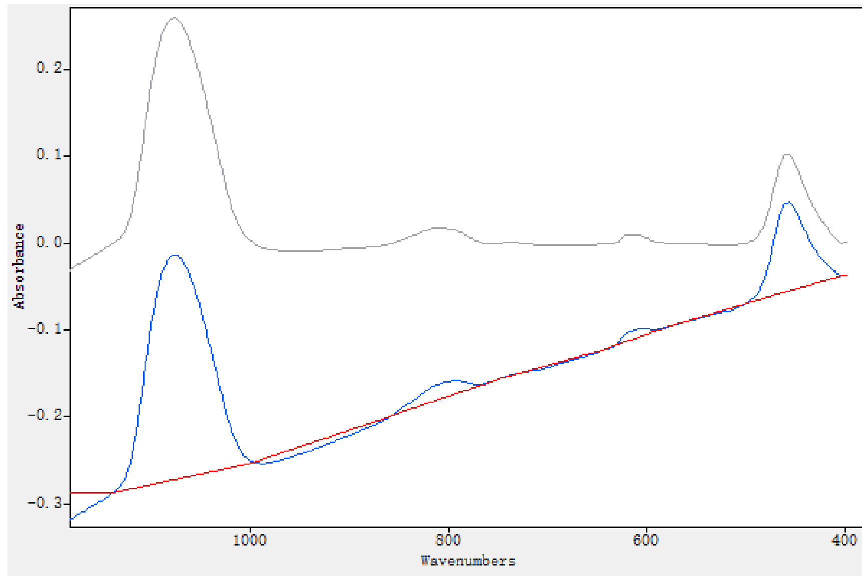

Figure 4.13. Applying baseline correction to remove background wave from thermal oxide FTIR spectrum

After removing of background wave, distinct peaks of absorption will be clear to see. The result of absorbance spectrum of thermal oxide is presented in Figure 4.14 (a). Identical method can be adopted for removing background waves in the spectrums of LPCVD and PECVD oxide. The final results are presented in Figure 4.14 (b) and (c) on the next page.

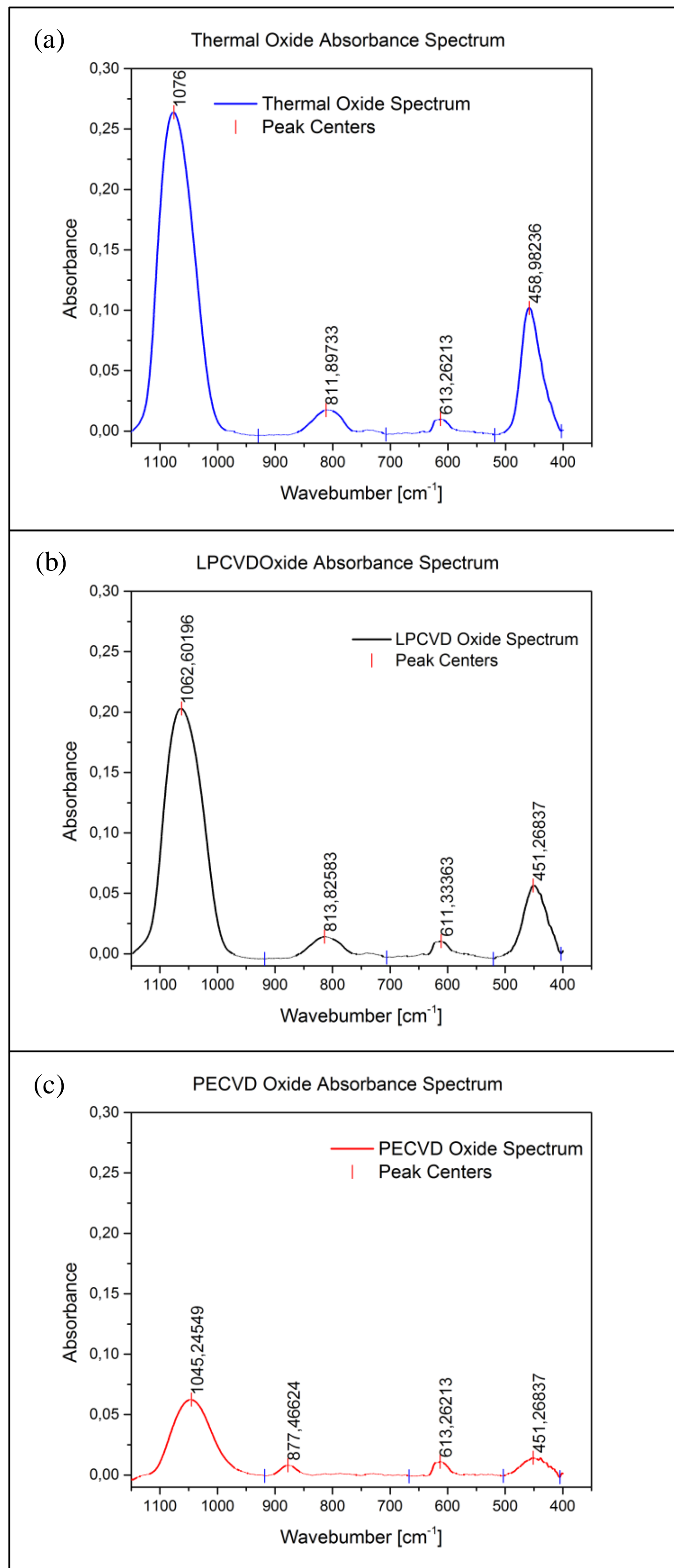

Figure 4.14(a)-(c). Absorbance spectra of three kinds of oxide substrates

From Figure 4.14, it is clearly represented that each kind of oxide has four distinct peaks. For thermal and LPCVD oxide, the peaks located around wavenumber 1050 cm^{-1}, 810 cm-1 and 450 cm^{-1} represent the Si-O-Si stretching mode, O-Si-O bending mode and Si-O-Si rocking/wagging mode respectively [5,8,9]. For PECVD oxide, the spectrum is a bit different. First, besides the major Si-O-Si stretching and rocking mode, there is an absorption peak around 870 cm^{-1}. In addition, there is no O-Si-O bending mode detected in PECVD oxide. According Rojas [6] and Shanks [17], absorption peak observed around 880 cm^{-1} can be attributed to Si-H stretching mode and definitely related to the existence of SiH_2 or SiH_3. The absence of O-Si-O bending mode in the spectrum can possibly be explained by the overall much weaker absorbance obtained from PECVD oxide, thus the intensity of O-Si-O bending mode may fall below the detection limit of the experiment.

Apart from the peaks just mentioned, a surprising fact occurred to be the absorption peak located at around 613 cm^{-1} in all oxide samples. Regarding this point, more discussions can be found in the end of the section.

After identifying the peaks, in order to compare the relative shift and broadness of peaks among three oxides, all three spectrums are presented together in Figure 4.15.

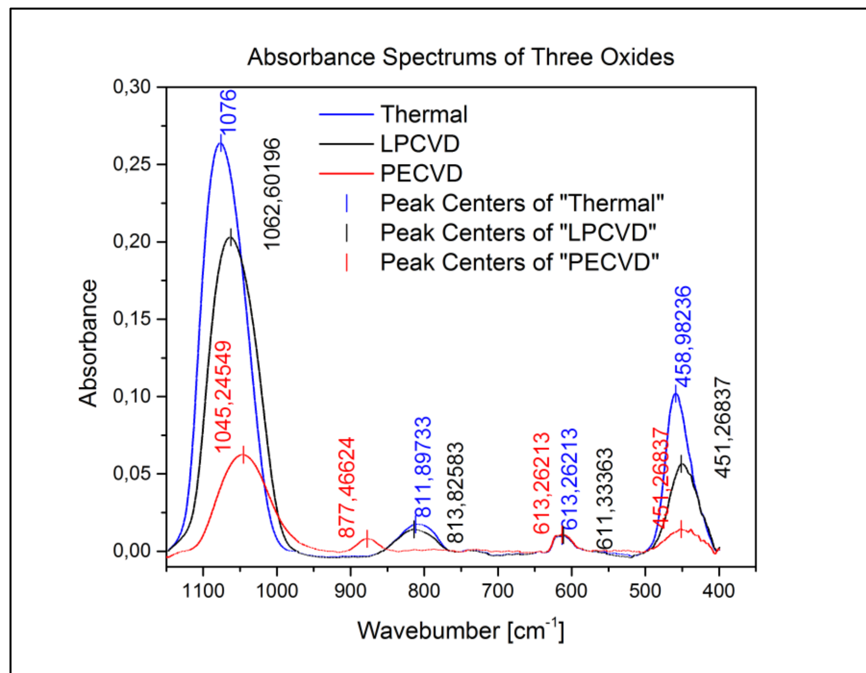

Figure 4.15. FTIR spectrums of all oxides in absorbance mode

From Figure 4.15 it is observed that, the band from Si-O-Si stretching mode and rocking mode all shift towards lower wavenumbers from Th to PECVD oxide. The O-Si-O bending mode is shifted towards higher wavenumbers from thermal oxide to LPCVD oxide. These observations are in agreement with the experiment results shown in [2]. Additionally, Pliskin pointed out porosity and bond strain of CVD films are the reasons for band shift and broadness effects.

It has been implied by Borghesi et al. [9] that the closer the vibration frequencies to the ideal data, the less porous (with less unsaturated bonds) the sample structure is. Thus, a summary is presented in the following table about peak data of oxides samples and data of crystalline SiO_2.

Table 4.2. Summary of absorbance peaks from samples and crystalline SiO_2

Vibration Mode	**Peak Frequency [cm^{-1}]**			
	Crystalline SiO_2[9]	Thermal Oxide	LPCVD Oxide	PECVD Oxide
Si-O-Si Stretching	1086	1076	1063	1045
O-Si-O Bending	784	812	814	NA
Si-O-Si Rocking	496	459	451	451

Comparing data of the three characteristic vibration modes of SiO_2 from the oxide samples to the data of crystalline structure, it is found that the peak frequencies from thermal oxide is closest to that of crystalline SiO_2, while peak frequencies from PECVD oxide being the farthest. It can be inferred from the implication by Borghesi that PECVD oxide has the most porous structure with more unsaturated Si bonds compared to the structure of LPCVD oxide, let alone the structure of thermal oxide.

Additionally, as already reported in Figure 4.14(c), FTIR spectrum reveals the existence of Si-H bonds in PECVD oxide. In fact, this is the strong proof proving that the structure of PECVD is porous because hydrogen ions saturated all the dangling bonds of Si atoms [9].

To summarize the previous discussions, FTIR study reveals that the spectra from the oxide samples match observations from historical researches. Thermal oxide sample has the structure being closest to crystalline SiO_2. LPCVD oxide has a more porous structure indicated by the broadness and peak shift effects of three characteristic SiO_2 bands. PECVD oxide sample has the most porous structure among all proved by not only the broadness and shift effects, but also the existence of Si-H bonds in the material.

Up till this point, the study of FTIR has successfully revealed the differences between three oxide samples. Besides all analysis reported above, few more facts from the spectra are still worth discussing.

Unlike often reported by other publications on CVD oxides for example [6,8,9], there is neither detectable peaks at around 3300 cm^{-1} which is related to H_2O molecules nor peaks like 939 cm^{-1} and 3650 cm^{-1} which is related to Si-OH bands [18]. It could be known from the fabrication flow introduced in section 4.1, that a special step to simulate graphene growth environment is taken in order to keep the oxide quality consistent between the one used in real device and FTIR analysis. In fact, ambient temperature gradually increases and maintain at 1000 °C during the graphene growth [19]. It can be inferred that the oxide samples were actually annealed during this process (see Appendix A for more information). Due to annealing, impurities like OH groups and H_2O molecules are effectively eliminated from the sample. Supporting evidence from [8] also states that annealing can reduce film porosity by decreasing Si-OH groups concentration and absorbed water, increasing at the same time the number of Si-O-Si bonds. Figure 4.16 demonstrates that after annealing Si-OH and H_2O are removed on a LPCVD TEOS oxide grown at 650 °C [8], which is exactly the same as the LPCVD oxide used in this thesis study.

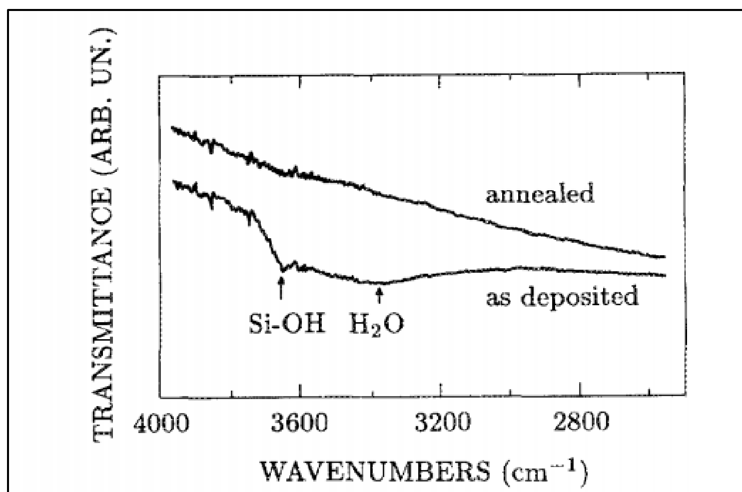

Figure 4.16. Infrared spectra of Si-OH and H_2O bonds stretching vibration for annealed and as deposited oxide [8]

One last note should pay attention to is the existence of an absorption peak at around 611 or 613 cm^{-1} in all oxide samples. Preliminary literature research did not provide clear evidence linking this absorption peak to any substance. While it is unclear about the exact reason causing this absorption peak, there are two possibilities. Because the peak wavenumber in all oxide samples are nearly identical, the first possible cause is a systematic error of the spectrometer during measurements. The second possible cause is by a certain kind of metal or organic group formed inside the graphene growth chamber. Because Aixtron BlackMagic Pro machine is considered contaminated, this possibility exists unless a detailed examination of material used in BlackMagic can provide counter-evidence.

4.4 Comparison of FLG on top of oxides using Raman measurement data

The properties of differently prepared oxides are analyzed in previous sections. In order to further demonstrate that the effects on gas sensing behavior are predominately brought by different oxide substrates, a comparison of FLG used in the sensors based on Raman measurement results will help add credibility to any conclusions drawn henceforth.

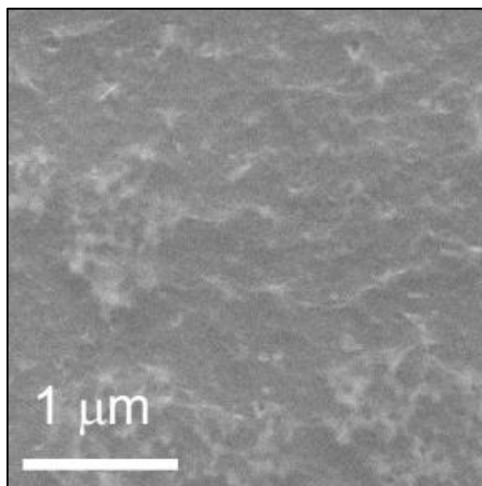

Figure 4.17. SEM image of CVD produced few layer graphene

Few spectra are reported in the following contexts based on data captured on three different points on the device. An example of FLG Raman spectrum has the following characteristics as presented in Figure 4.18. The spectrum intensity is normalized to the value of G peak.

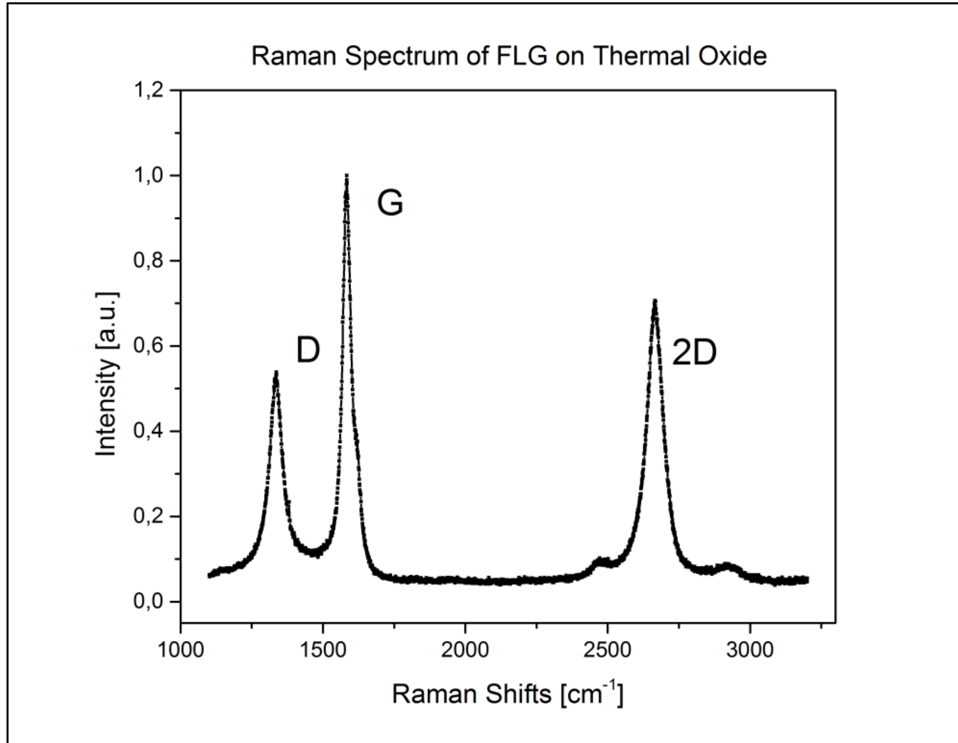

Figure 4.18. Raman spectrum of FLG on thermal oxide

All spectra to be presented henceforth are also normalized to the value of its corresponding G peak, being reported in Figure 4.19-21.

- Figure 4.19 presents the Raman spectra of FLG on thermal oxide at three different points
- Figure 4.20 presents the Raman spectra of FLG on LPCVD oxide at three different points
- Figure 4.21 presents the Raman spectra of FLG on PECVD oxide at three different points

As can be observed in Figure 4.18, D, G and 2D peak are the characteristic peaks of graphene. As demonstrated in Ref [20], the rise of D peak is associated with the defects of graphene, however 2D peak (overtone if D peak) is always present regardless of defects.

The average Raman spectra are calculated from the spectra of three points as shown in Figure 4.19-21. The result of the averaged Raman spectra of FLG on three different oxides is presented at last in Figure 4.22.

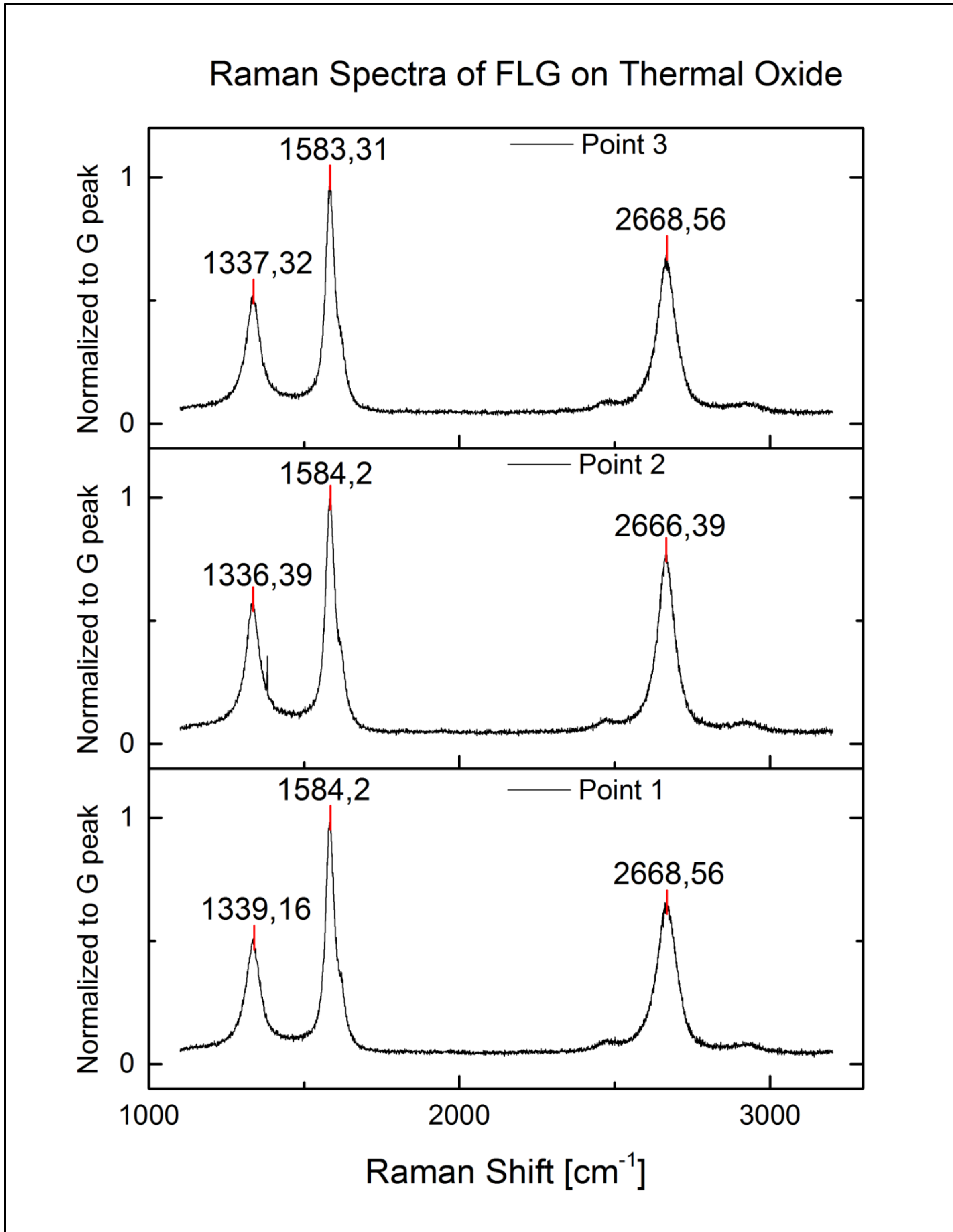

Figure 4.19. Raman Spectra of FLG on top of thermal oxide at three different points

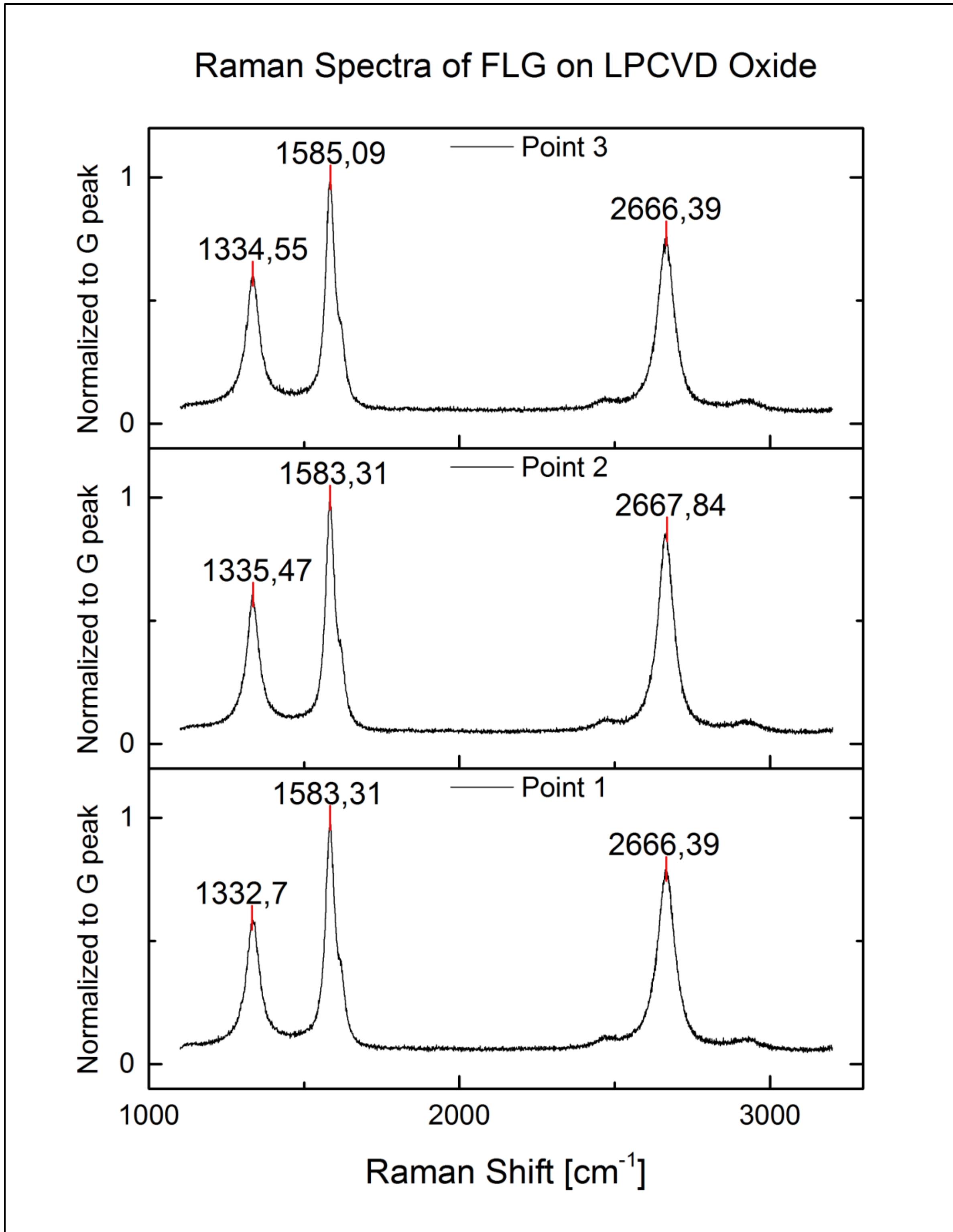

Figure 4.20. Raman Spectra of FLG on top of LPCVD oxide at three different points

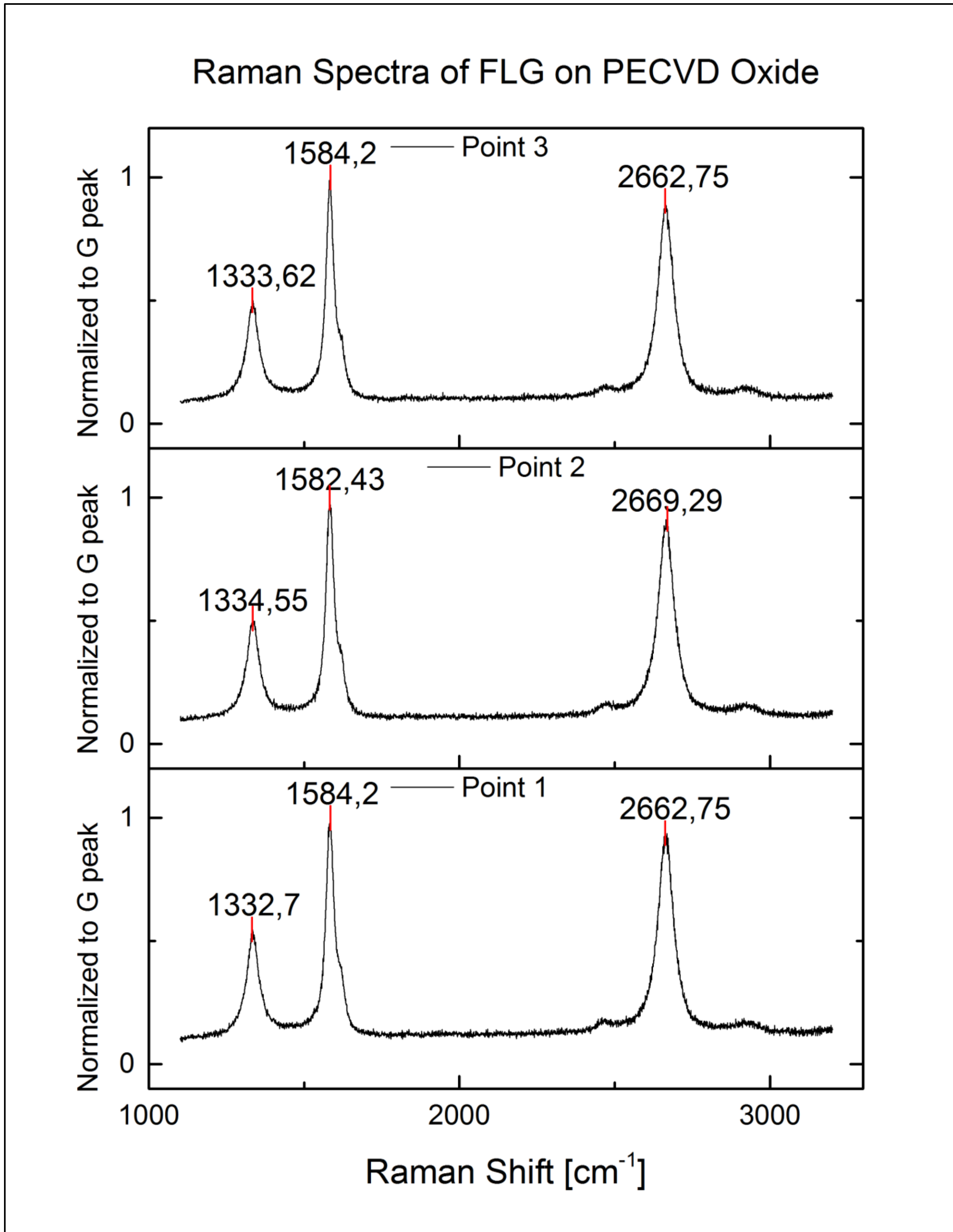

Figure 4.21. Raman Spectra of FLG on top of PECVD oxide at three different points

In Figure 4.19-21, every feature is labeled with its related Raman shift. It is first observed that for FLG on top of the same kind of oxide substrate, the characteristic D, 2D and G peaks among spectra obtained at three different points are similar. This indicates the good uniformity of samples. In particular, taking into the I(D)/I(G) ratio in Figure 4.19-4.21 to analyze the Raman spectra, it can be inferred from the results in Table 4.3 that the FLG on top of each kind of oxide substrate is similar because on average the difference of I(D)/I(G) ratios is at most 13%.

Table 4.3. I(D)/I(G) ratios of Raman spectra of FLG on different oxide substrates

FLG on	I(D)/I(G) of Raman Spectrum			
	Point 1	Point 2	Point 3	Average
Thermal Oxide	0,51	0,58	0,54	0,54
LPCVD Oxide	0,59	0,61	0,61	0,60
PECVD Oxide	0,55	0,51	0,50	0,52

An average Raman spectrum of FLG on top of each kind of oxide substrate can be calculated in order to compare among three oxide substrates. Figure 4.22 presents the final averaged spectra in the same frame.

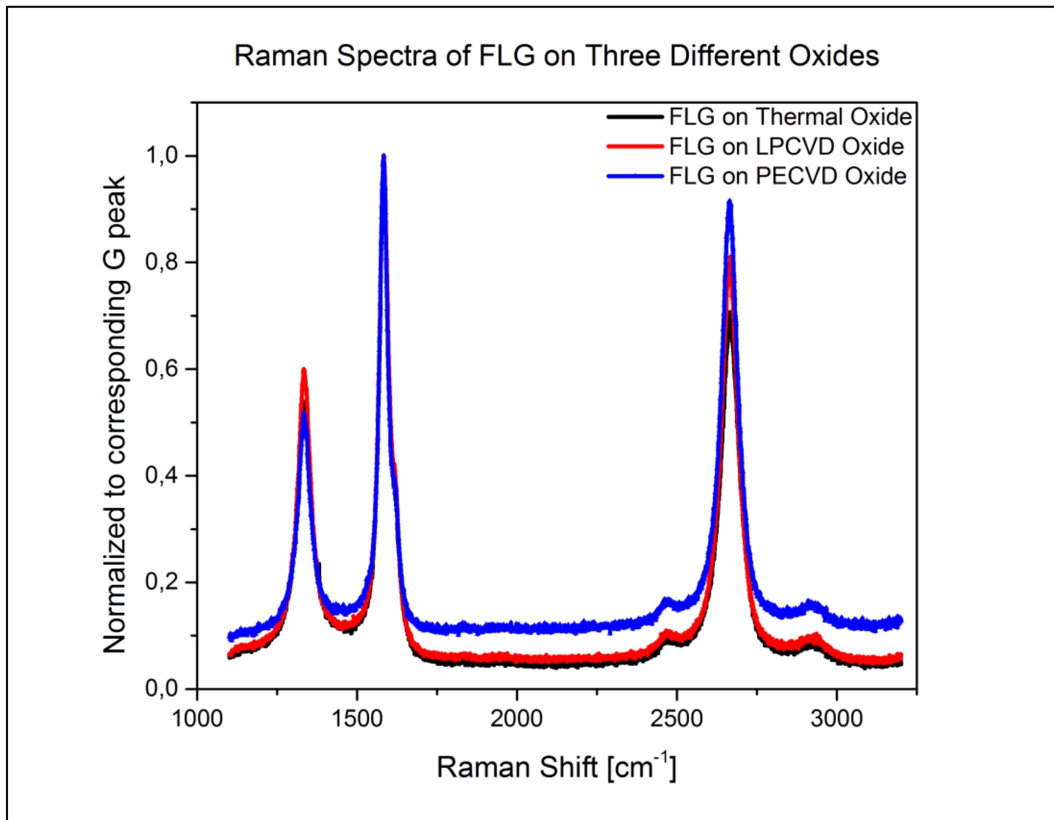

Figure 4.22. Raman spectra of FLG on top of three different oxide substrates

Details about spectra in Figure 4.22 are summarized below in Table 4.4. It is observed that the wavenumbers of D, 2D and G peaks of all kinds of oxide substrate are within extreme small distance from each other, no

larger than 3 cm^{-1}. This observation is indicating the FLG is of substantial equivalence among three different samples.

Table 4.4. Peak data of averaged Raman spectra of FLG on different oxide substrates

Averaged spectrum of FLG on	Peak Raman Shift [cm^{-1}]		
	D	G	2D
Thermal Oxide	(1336)	(1583)	(2666)
LPCVD Oxide	(1334)	(1583)	(2667)
PECVD Oxide	(1335)	(1584)	(2665)

Hereby, it can be inferred that the differences of gas sensing behavior among the T sensors, L sensors and P sensors mentioned in Chapter 3 are predominately caused by the effect of different oxide substrates, having demonstrated the substantial equivalence of the sensing material.

4.5 Conclusions and implications on sensing behavior from material study

Through material study by C-V measurements and FTIR measurements, it is clear that the properties of the thermal oxide, LPCVD oxide and PECVD oxide are different.

In particular, fixed oxide charge calculations by C-V measurements in section 4.2 indicate that the quality of PECVD and LPCVD oxide is worse than quality of thermal oxide. LPCVD sample in that case has the largest fixed oxide charge, -22.8×10^{10} e/cm^{-2}, being the worst among all types that have values of 3.72×10^{10} e/cm^{-2}, -22.8×10^{10} e/cm^{-2} and 17.5×10^{10} e/cm^{-2} respectively.

In section 4.3, FTIR analysis reveals that structure from thermal oxide is the closest to the perfect crystalline structure, while PECVD structure being the most porous among all. The characteristic bonds of SiO_2 are found in all oxide samples, but inside PECVD oxide the existence of Si-H bond is proved and this point also supports the judgement that PECVD oxide has a porous structure with the most unsaturated bonds among all three types of oxides.

Previously, in Chapter 3 analysis reveals that sensing responses from device based on PECVD oxide substrate exhibit the greatest magnitude and rate of conductance variation. On the contrary, sensing responses from device based on thermal oxide substrate show the entire opposite. It can be inferred by the findings in this chapter that the quality of oxide structure is a direct influencing factor of gas sensing behavior. The more porous and imperfect the oxide is, the higher the sensing response magnitude and rate of conductance variation will be. Defects and impurities such as hydrogen ions will degrade the oxide structure and hence possibly increase the sensing responses. In Chapter 2, it is speculated within discussions that whether through engineering the substrate properties it is able to affect sensing behaviors. Here, through study of sensing responses and material properties related to differently prepared oxide substrates, it can be concluded that defects in oxide substrates is found to be effectively useful in improving gas sensing behaviors.

Besides, in section 4.4, comparison of Raman Spectra of FLG on top of different oxides indicates that FLG characteristics are similar in all cases. Therefore, it is reasonable to conclude that different sensing behaviors are predominately due to the role played by different oxide substrates.

Coming next, in Chapter 5, investigations about graphene-metal contacts are introduced. Being part of the efforts to improve gas sensing properties, its related results will be able to provide beneficial information to develop better graphene-metal contacts in a gas sensor system overall.

References

1. Franssila, S., 2010. *Introduction to microfabrication*. John Wiley & Sons.

2. Pliskin, W.A., 1977. Comparison of properties of dielectric films deposited by various methods. *Journal of Vacuum Science and Technology*, *14*(5), pp.1064-1081.

3. Lucovsky, G., Mantini, M.J., Srivastava, J.K. and Irene, E.A., 1987. Low-temperature growth of silicon dioxide films: a study of chemical bonding by ellipsometry and infrared spectroscopy. *Journal of Vacuum Science & Technology B: Microelectronics Processing and Phenomena*, *5*(2), pp.530-537.

4. Carlotti, G., Doucet, L. and Dupeux, M., 1997. Elastic properties of silicon dioxide films deposited by chemical vapour deposition from tetraethylorthosilicate. *Thin Solid Films*, *296*(1-2), pp.102-105.

5. Shokri, B., Firouzjah, M.A. and Hosseini, S.I., 2009, August. FTIR analysis of silicon dioxide thin film deposited by metal organic-based PECVD. In *Proceedings of 19th international symposium on plasma chemistry society* (Vol. 2631).

6. Zhang, X., Chen, K.S., Ghodssi, R., Ayon, A.A. and Spearing, S.M., 2001. Residual stress and fracture in thick tetraethylorthosilicate (TEOS) and silane-based PECVD oxide films. *Sensors and Actuators A: Physical*, *91*(3), pp.373-380.

7. Rojas, S., Zanotti, L., Borghesi, A., Sassella, A. and Pignatel, G.U., 1993. Characterization of silicon dioxide and phosphosilicate glass deposited films. *Journal of Vacuum Science & Technology B: Microelectronics and Nanometer Structures Processing, Measurement, and Phenomena*, *11*(6), pp.2081-2089.

8. Rojas, S., Modelli, A., Wu, W.S., Borghesi, A. and Pivac, B., 1990. Properties of silicon dioxide films prepared by low-pressure chemical vapor deposition from tetraethylorthosilicate. *Journal of Vacuum Science & Technology B: Microelectronics Processing and Phenomena*, *8*(6), pp.1177-1184.

9. Borghesi, A., Colombo, L., Rojas, S. and Wu, W.S., 1988. Infrared characterization of silicon dioxide films obtained by chemical vapour deposition. *Il Nuovo Cimento D*, *10*(12), pp.1487-1496.

10. Hu, C., 2010. *Modern semiconductor devices for integrated circuits*. Prentice Hall. Chapter 5: MOS Capacitor.

11. Trifunovic, M., 2016. Liquid Silicon for Printed Polycrystalline Silicon Thin-Film Transistors on Paper. PhD Thesis. Delft University of Technology.

12. Zhang, J., 2015. Liquid-Si Technology for High-Speed Circuits on Flexible Substrates. PhD Thesis. Delft University of Technology.

13. Schouten, M., 2013. The nanostructure of hydrogenated amorphous silicon, examined by means of thermal annealing and light soaking. Master Thesis. Delft University of Technology.

14. Tomozeiu, N., 2011. Silicon Oxide (SiOx, 0<x<2): a Challenging Material for Optoelectronics. In *Optoelectronics-Materials and Techniques*. InTech.

15. Van Vliet, J., 2016. Hydrogenated amorphous silicon oxide passivation layer for silicon heterojunction solar cells. Master Thesis. Delft University of Technology.

16. Brodsky, M.H., Cardona, M. and Cuomo, J.J., 1977. Infrared and Raman spectra of the silicon-hydrogen bonds in amorphous silicon prepared by glow discharge and sputtering. *Physical Review B*, *16*(8), p.3556.

17. Shanks, H., Fang, C.J., Ley, L., Cardona, M., Demond, F.J. and Kalbitzer, S., 1980. Infrared spectrum and structure of hydrogenated amorphous silicon. *physica status solidi (b)*, *100*(1), pp.43-56.

18. Chou, J.S. and Lee, S.C., 1995. Effect of porosity on infrared-absorption spectra of silicon dioxide. *Journal of applied physics*, *77*(4), pp.1805-1807.

19. Vollebregt, S., Alfano, B., Ricciardella, F., Giesbers, A.J.M., Grachova, Y., van Zeijl, H.W., Polichetti, T. and Sarro, P.M., 2016, January. A transfer-free wafer-scale CVD graphene fabrication process for MEMS/NEMS sensors. In *Micro Electro Mechanical Systems (MEMS), 2016 IEEE 29th International Conference on* (pp. 17-20). IEEE.

20. Ricciardella, F., 2015. From Graphene to Graphene-Based Gas Sensors Operating in Environmental Conditions. PhD Thesis. University of Napoli “Federico II”

Chapter 5. Study of Contact Resistance Between Graphene and Metals

5.0 Overview

This chapter introduces the motivation for contact resistance study in section 5.1, and then discusses how to measure contact resistance in section 5.2. Results of contact resistance measurement are presented in section 5.2 along with problems encountered in the experiments as well. Moreover, different metal-graphene contacts are examined with scanning electron microscope (SEM) to provide more useful information. Finally, conclusions are reported in section 5.3.

5.1 Motivation of contact resistance study and Experiment Setups

In Chapter 1 to Chapter 2 of the thesis, the promising future of using graphene chem-resistor for gas sensing application is discussed. Along with other applications of graphene, such as high-speed electronics or optoelectronics, it becomes never more important than now to understand deeper how to reduce metal-graphene contact resistance (R_c) and form high-quality and stable low-resistance ohmic contacts [1-3]. Previous work from many researchers have purposed theoretical models and pioneer experimental works to explore graphene metal interaction [1-7]. So far, the following discoveries have been reported:

> Physical contact with the environment will deviate the ideal behaviors of graphene. Graphene interactions with metals like Co, Ni and Pd are strong such that the characteristic electronic structure is significantly altered. However, for metals such as Al, Cu, Ag, Au and Pt, the interactions with graphene is weaker so original properties like the zero band-gap are preserved [4,5].

1) Graphene sheet can be doped through charge transfer at a metal-graphene interface under the influence of metal substrates because the Fermi level is moved away from the original conical point where conduction and valance band meet. Specifically speaking, graphene is doped n-type on Al, Ag, and Cu and p-type on Au and Pt [4,5].
2) Contact resistance shows no or very weak relation to work function differences between graphene and various metals [2,3], indicating that fabrication processes of metal-graphene contacts can heavily influence the ability to dope graphene through work function difference engineering [2].

Besides, the effects of atomistic configuration at the contact region between graphene and metals received lots of attention. It has been reported by Cusati et al [1] that metals with strong interactions with graphene, such as Ni and Pd, show small sensitivity of contact resistance towards factors such as point defects, small contact length and edges without chemical terminations at the contact region. On the contrary, metals with weak interactions, such as Au and Ag, are sensitive to those factors. At last, metals like Pt and Cu with an intermediate strength of interaction, exhibit a slight dependence of the contact resistance on those factors of the contact region.

In this work, efforts are made to continue investigating the differences of contact resistance between graphene and various metals, with a special focus on examining whether metal-graphene contacts have a stronger peripheral or area dependency of device geometry. To this aim, metal-graphene contacts are fabricated in the form of Cross Bridge Kelvin Resistor (CBKR) structure, using CVD graphene and metal layers deposited with Cr/Au, Ti, Pd, Al (1% Si) and Pt/Ta, respectively. For each metal-graphene contact configuration, contact region with the following sizes (feature size) are fabricated: 2x2 μm^2, 5x5 μm^2, 10x10 μm^2, 15x15 μm^2, 20x20 μm^2, 25x25 μm^2 and 30x30 μm^2. The fabrication flow of metal-graphene contacts is summarized as the following procedures (see Appendix C for details):

- Starting materials are six 4-inch single side polished process wafers, P-type doped with <100> orientation. Resistivity: 2-5 Ω•cm
- Make alignment markers on each wafer and number each wafer after line width inspection
- Clean wafers and then grow 90nm thick SiO_2 with dry oxidation.
- 50nm thick Mo deposition using TRIKON SIGMA sputter coater and CVD growth of graphene in Aixtron BlackMagic Pro
- Backside 200nm thick TiN deposition using TRIKON SIGMA sputter coater
- Contact region patterning with lithography
- 100 nm thick metal layer deposition on each wafer. Use deposition machine Balzers for Cr/Au, CHA for Ti, Al (1% Si), Pd and Pt. Two wafers are deposited with Cr/Au metal layer in this work.
- Metal lift off with NMP (N-Methyl-2-pyrrolidone) bath > 50°C
- Clean wafers with deionized (DI) water and spin dry wafers. Store wafers for measurements

There are totally 52 dies on each wafer as shown in Figure 5.1, and after fabrication each die contains metal-graphene contacts with 7 different sizes.

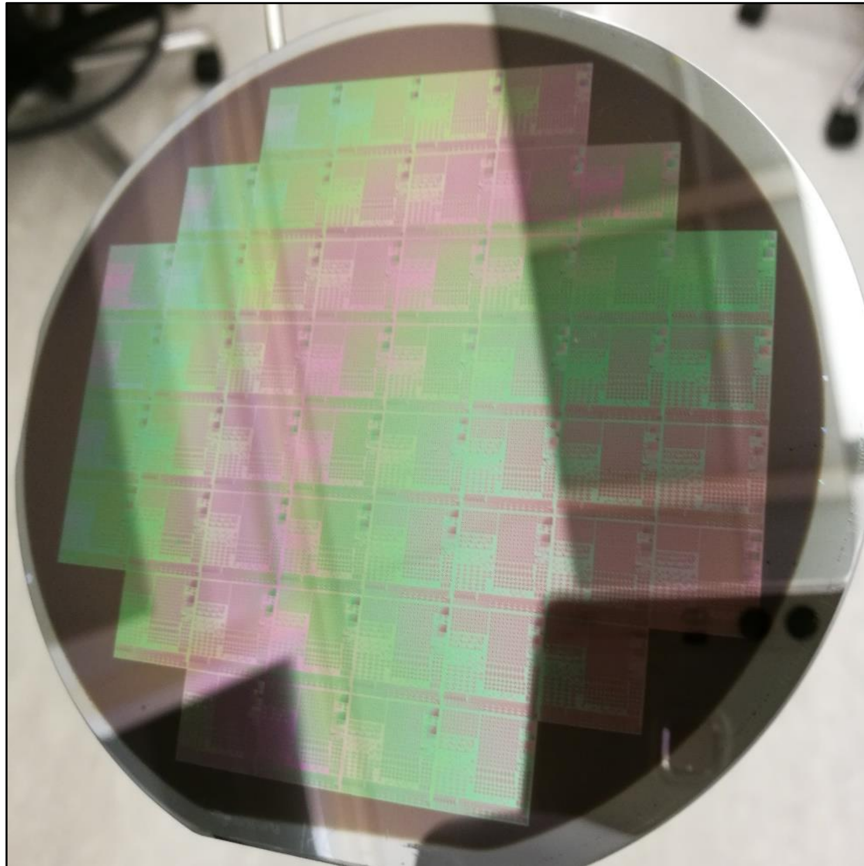

Figure 5.1. A wafer under inspection during contact resistance fabrication

During final inspection of wafers under microscope after all fabrication processes end, it is found that the yield of working device is lower than expected. Especially on wafer deposited with Al and Pt, barely any working device survived. This was caused by graphene peeling off during the lift-off step. Details will be

introduced in following discussions about measurement results obtained from each type of metal-graphene contacts.

5.2 Contact Resistance Measurement Results and Analysis

An example layout of CBKR structure for measuring is shown in Figure 5.2 below. The methodology of contact resistance calculation in this work is the same as discussed in ref [8].

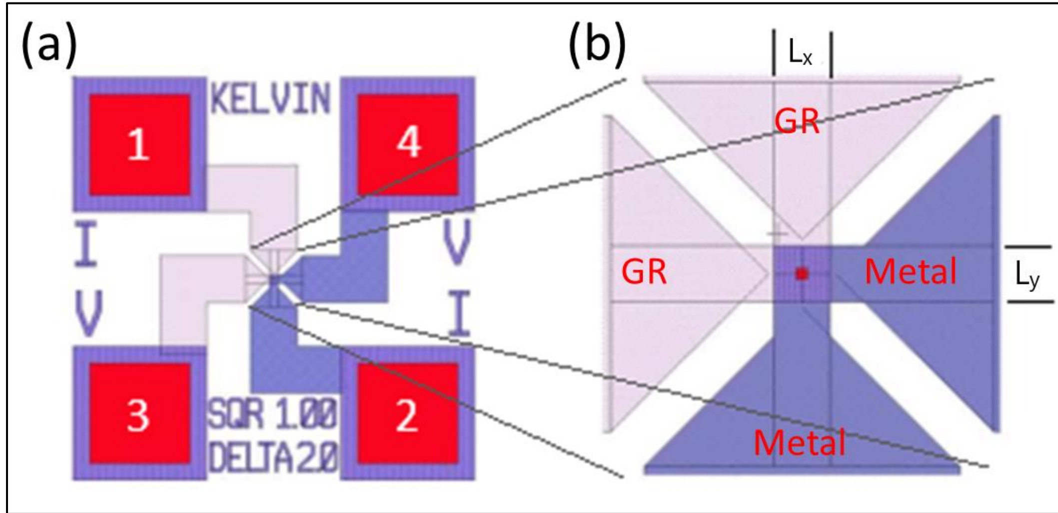

Figure 5.2. Layout of a CBKR structure with bond pads (a) and enlarged version of the actual contact region (b) [8]

To conduct contact resistance measurement through a CBKR structure as shown in Figure 5.2, a current (I_{12}) is forced between pad 1 and 2 and the corresponding voltage drop between pad 3 and 4 (V_{34}) is measured. Then Kelvin resistance (R_k) is calculated as

$$R_k = \frac{V_{34}}{I_{12}}$$

Because 1-D model can be applied for the purpose of this work [8], the Kelvin resistance therefore equals the contact resistance (R_c).

$$R_C = R_k = \frac{V_{34}}{I_{12}}$$

In this work, it is designed that $L_x = L_y = L$. Therefore, specific contact resistance (ρ_c) in this case is

$$\rho_c = R_c \times W_x \times W_y = R_c \times L^2$$

All test structures on each wafer are automatically measured through a probe station with the source measurement units and data recorded by Agilent ICCAP software. To facilitate data analysis and visualize results from a large quantity of data, a dedicated wafer scale data analysis software, ECTM Data Analysis Master, is adopted in this work. A wafer map with measurement detailed results of each test structure under the desired feature size is generated by the end of analysis. Results from contacts made by graphene and different metals are presented in the following sections.

The analysis of Cr/Au metal-graphene contact (Cr/Au contact) below will play the role of an example to present the steps of data processing. Measurement results from other types of metal-graphene contacts follow the same analysis steps.

Cr/Au Contact

As discussed above, the wafer map can be generated by ECTM Data Analysis Master to help data analysis. In order to minimize the effect of low yield of successfully fabricated test structure, data pre-screening rules are applied to tick out data points with random, abnormally high ($>10^6$) or negative R_c values, related to structures with total failures such as metal or graphene layer delamination. Structures with minor failures such as surface adhesion problem between oxide and metal layer could exhibit measurement results with Schottky contact behavior. These data points are also excluded from data analysis. Pre-screening process rules out most of the irrational data, allowing data obtained from well-performing structures to be selected so that wafer maps presenting useful information can be generated.

Here the wafer map of Cr/Au contact with feature size of 30x30 μm^2 is presented in Figure 5.3.

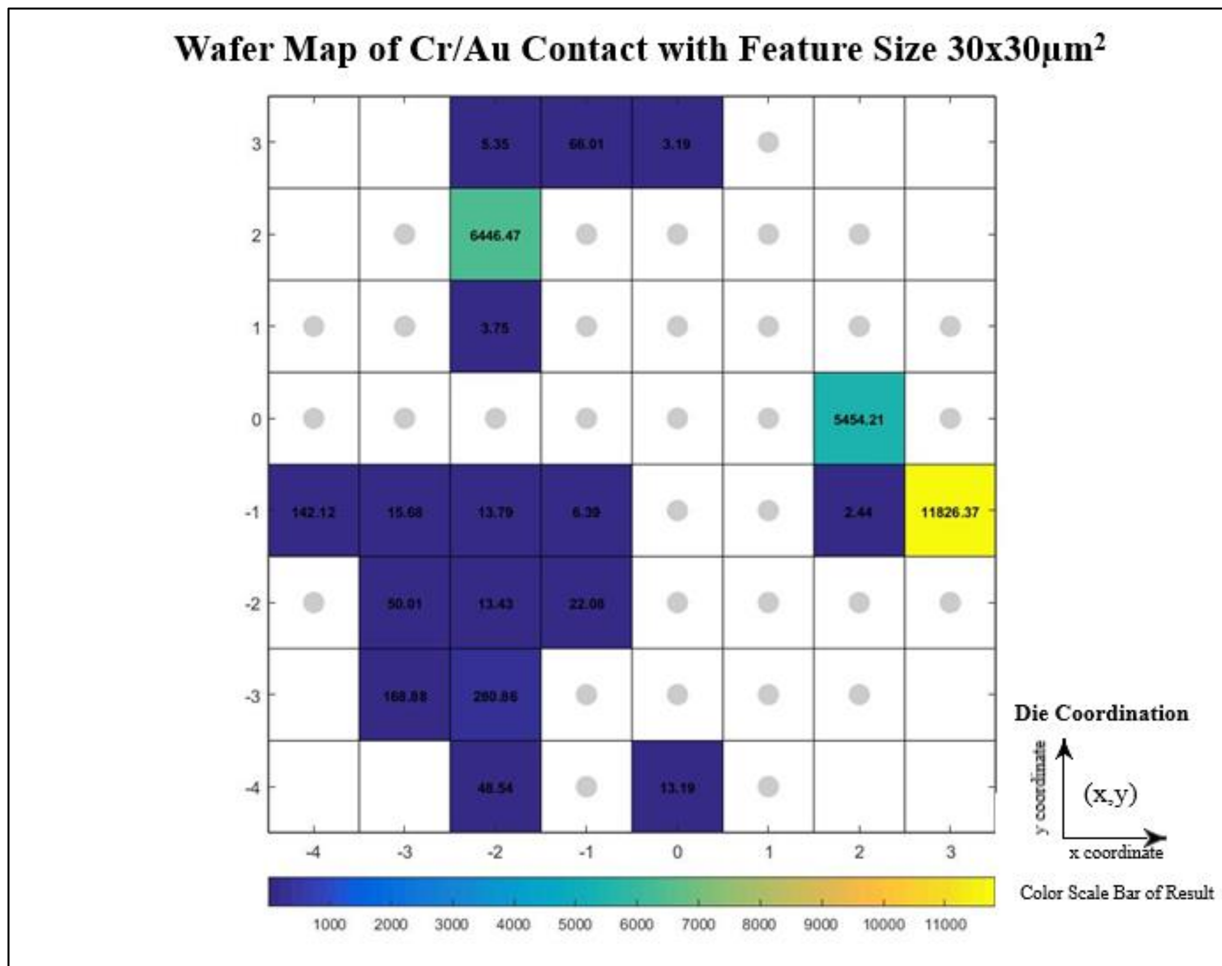

Figure 5.3. Wafer Map from Cr/Au contact with feature size of 30x30 μm^2. Color bar represents the relative level of magnitude of R_c measured on different dies.

Each wafer map organizes all 52 dies with x-y coordinates and an extra color scale bar at the bottom to visually represent the relative level of magnitude of R_c measured on different dies.

From Figure 5.3, it is observed that the contact resistance value of die (-2,-2), (2,0) and (3,-1) are 1000 times larger than values from the majority of dies, thus they are considered as abnormal data points as well. Having values to be considered at round the same level of magnitude, as indicated by the color scale bar, these data are selected as the base of analysis for Cr/Au contact with feature size of 30x30 µm². Besides, it is found through data analysis of wafer maps that the median is the best measure to represent the contact resistance value of a data set, because the majority of data are within the same level of magnitude, but few data points are 2 or 3 orders of magnitude larger than the majority. Contact resistance for Cr/Au contact under other feature sizes can be analyzed in the same manner, then a summary of the results is presented in Table 5.1.

Table 5.1. Summary of Contact Resistance data for Cr/Au contacts

Feature		**Contact Resistance [Ω]**	**Specific Contact Resistance [µΩ• cm²]**
Length [µm]	Area [µm²]		
2	4	529	21,2
5	25	86	21,5
10	100	27	27
15	225	26	58,5
20	400	18	72
25	625	9	56,3
30	900	15	135

Figure 5.4 below shows the plotted relationships of contact resistance with repect to length and area of the feature design.

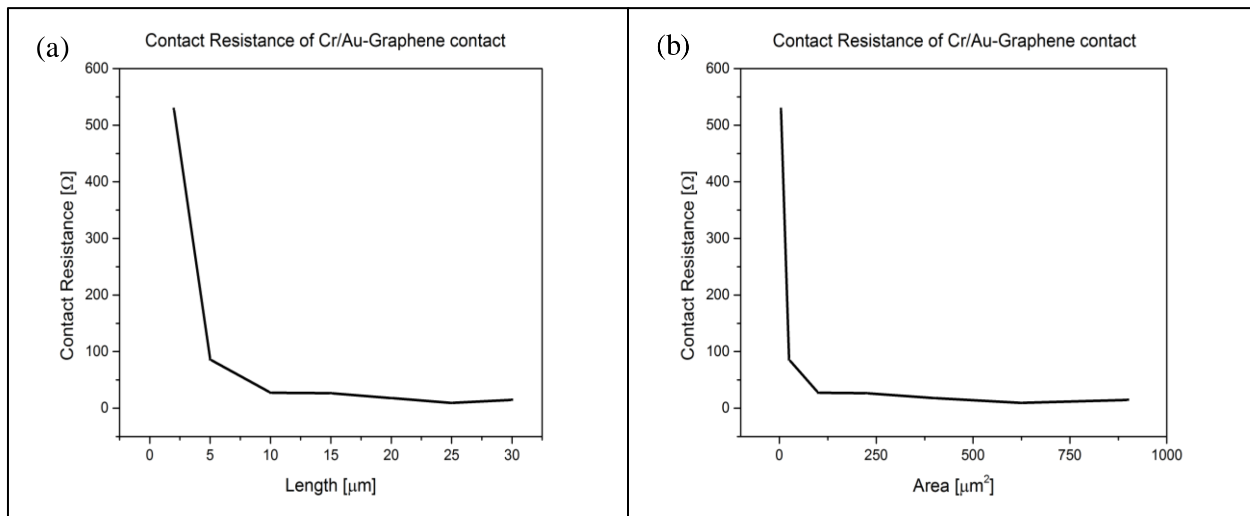

Figure 5.4. Rc vs Length (a) and area (b) of Cr/Au-Graphene contact

It is first observed in Figure 5.4 (a)–(b) that the contact resistance value decreases rapidly as the feature size increase from 2x2 µm² to 10x10 µm². Then, also combining the data shown from Table 5.1, it shows

that for the same amount of feature length/area percentage variation, contact resistance changes more with respect to feature length than feature area. For example, such comparison is shown in Table 5.2 below.

Table 5.2. Variation of contact resistance w.r.t. length and area change of Cr/Au contacts

Change of feature length [%]	Percent variation of R_c [%]	Change of feature area [%]	Percent variation of R_c [%]
400 [5-20 µm]	79	625 [100-625 µm^2]	67
300 [5-15 µm]	70	400 [25-100 µm^2]	68

From the obtained data in Table 5.2, it is shown that smaller or equal amount of percentage change of feature length leads to larger variation of contact resistance. It can be inferred that the contact resistance of Cr/Au contact exhibit stronger dependency on feature length than feature area.

Ti Contact

Using similar analyzing methodology, the results of contact resistance measurements are obtained and summarized in Table 5.3 for the Ti contacts.

Table 5.3. Summary of Contact Resistance data for Ti contacts

Feature		Contact Resistance [Ω]	Specific Contact Resistance [µΩ• cm^2]
Length [µm]	Area [µm^2]		
2	4	2048	81,9
5	25	592	148
10	100	202	202
15	225	75	168,8
20	400	147	588
25	625	97	606
30	900	106	954

And corresponding plot of relationships of contact resistance with repect to length and area of the feature is presented in Figure 5.5.

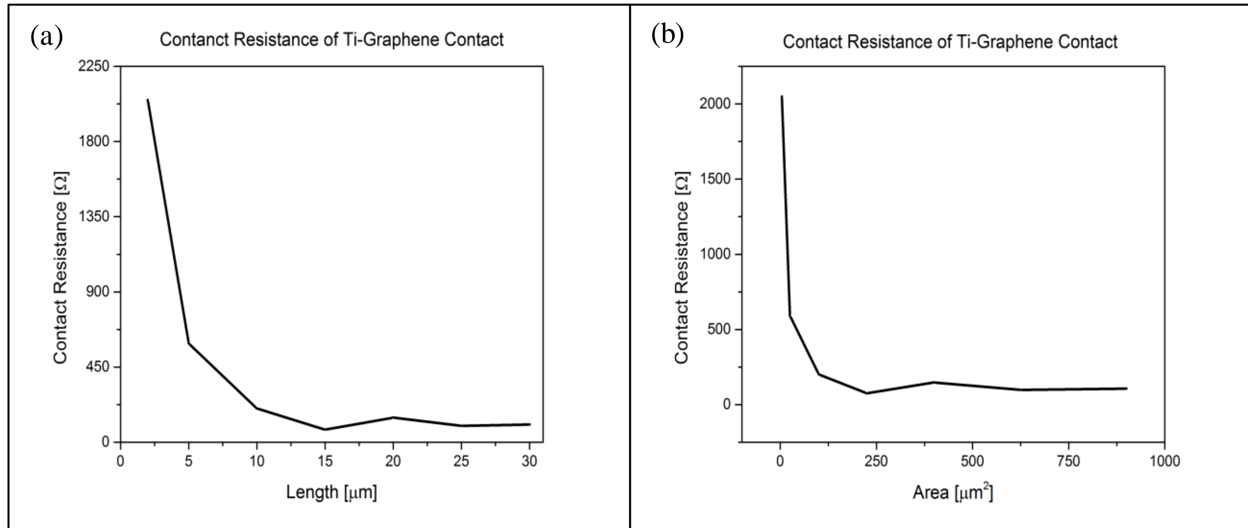

Figure 5.5. Rc vs Length (a) and area (b) of Ti-Graphene contact

Similar trends are observed as presented in the discussion of Cr/Au contacts. Combining Table 5.3 and Figure 5.5, a comparison of variation of contact resistance with respect to change in feature length and area is shown in Table 5.4.

Table 5.4. Variation of contact resistance w.r.t. length and area change of Ti contacts

Change of feature length [%]	Percent variation of R_c [%]	Change of feature area [%]	Percent variation of R_c [%]
400 [5-20 μm]	75	625 [100-625 μm^2]	52
300 [5-15 μm]	87	400 [25-100 μm^2]	66

From the obtained data in Table 5.4, it is shown that smaller or equal amount of percentage change of feature length leads to larger variation of contact resistance. This is in agreement with the observation reported about Cr/Au-graphene contacts. Therefore, it can also be inferred that the contact resistance of Ti contact exhibit stronger dependency on feature length than feature area.

Pd Contact

For palladium contact with larger feature sizes, no working device is found due to the low yield problem, for example as shown in Figure 5.6, possibly caused by delamination of metal layer at contact area.

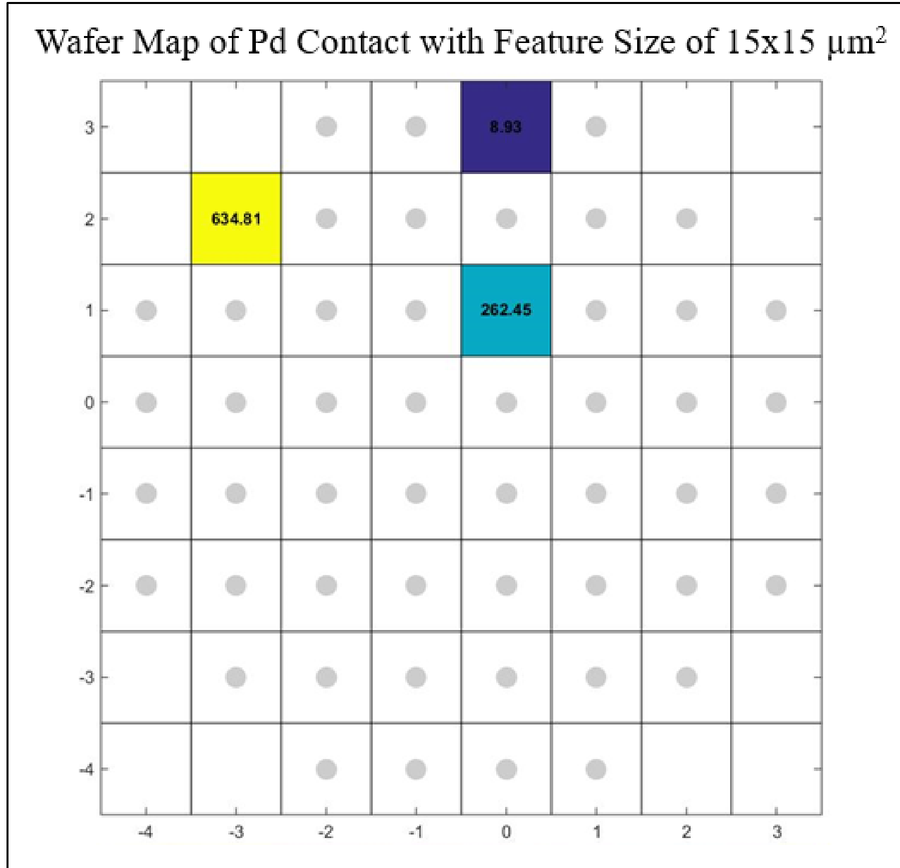

Figure 5.6. Low yield from Pd contact with feature size of 15x15 µm2

However, for feature size of 2x2 µm^2 and 5x5 µm^2, working structures are found and their results are summarized in Table 5.5 below.

Table 5.5 Summary of Contact Resistance data for Pd contacts

Feature		Contact Resistance [Ω]	Specific Contact Resistance [µΩ• cm^2]
Length [µm]	Area [µm^2]		
2	4	8	0,32
5	25	4	1

As shown in Table 5.5, the specific contact resistance of Pd is even lower than that of Cr/Au contact. This result presents opportunity to investigate in the future of using Pd to make contacts with ultralow contact resistance values.

Other Metal-Graphene Contacts

As for Al contact and Ta/Pt contacts, not enough working devices survived for useful measurements of all feature sizes. Figure 5.7-8 are examples to present this low-yield problem, which is covered in details in the following discussions about SEM pictures. No useful data exist after pre-screening and manual selection. Therefore, it is not possible to retrieve any more information.

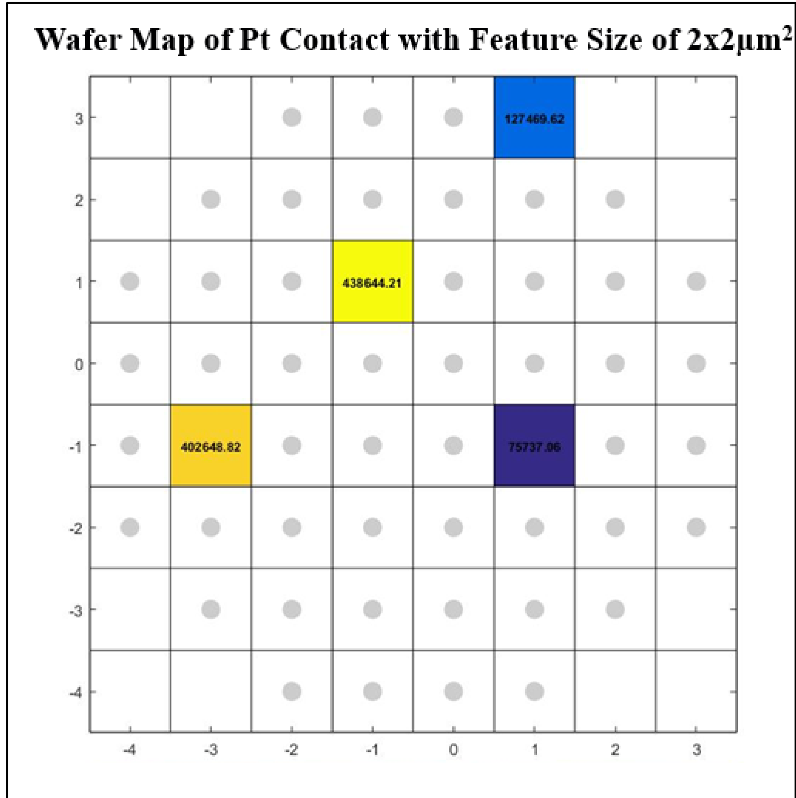

Figure 5.7. Low yield from Pt contact with feature size of 2x2 μm^2

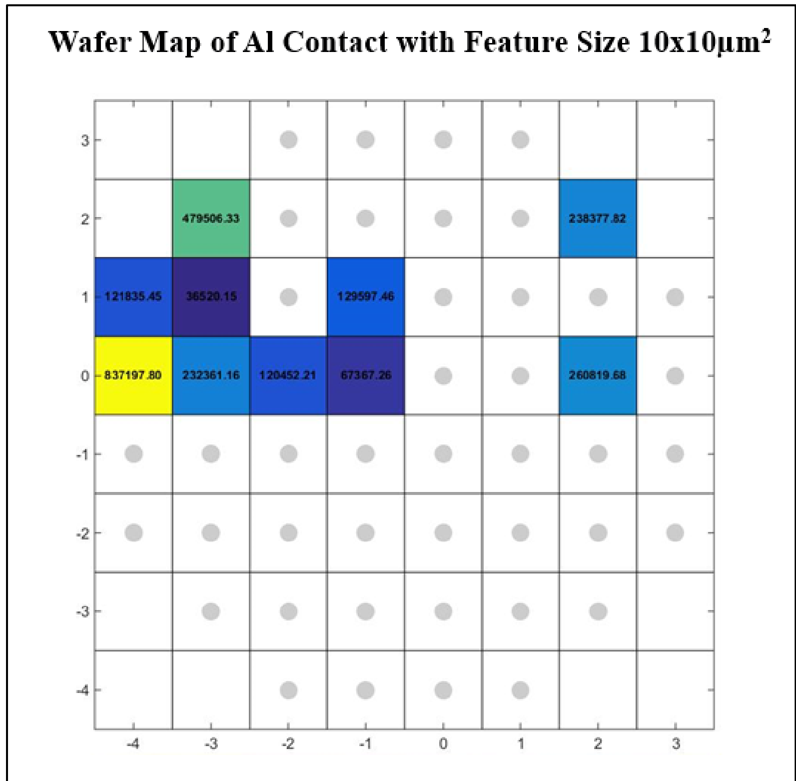

Figure 5.8. Low yield from Al contact with feature size of 10x10 µm2

The fabricated metal-graphene contacts are also studied with scanning electron microscope (SEM) to closely examine the structure at the contact region between metal and graphene. With SEM it is also possible to investigate the mechanisms causing low-yield of working structures.

In Figure 5.9-10, the SEM pictures of Cr/Au contact are presented.

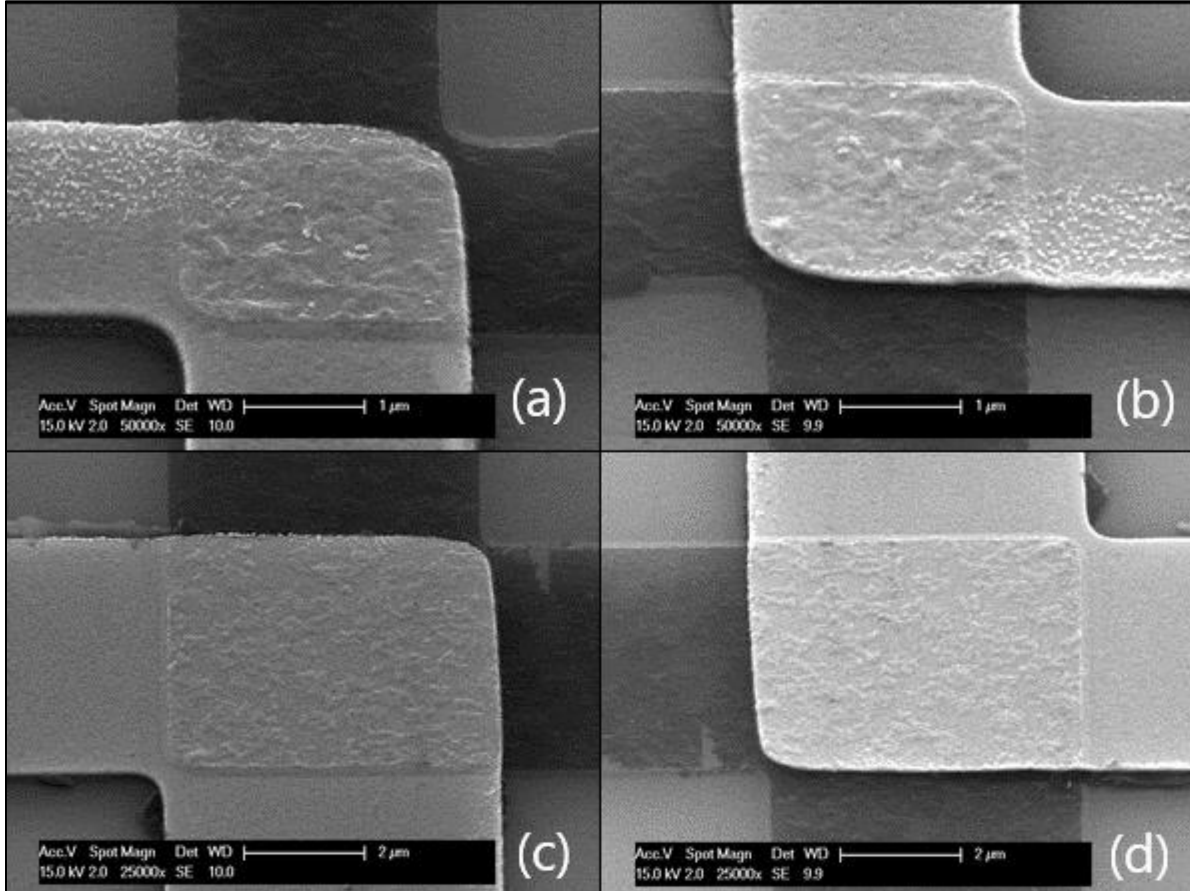

Figure 5.9. SEM pictures of Cr/Au contacts. (a)&(b) present contact area with size 2x2 μm^2; (c)&(d) present contact area with size 5x5 μm^2

As shown in Figure 5.9 (a) – (d), the brighter layer is the Cr/Au metal layer, the darker layer underneath is the graphene. It is observed that the surface of contact area is not smooth. Because metal is deposited on top of the graphene layer, then the uneven surface texture of graphene will result in uneven surface structure of the metal layer laid down on top. In general, the structure has no major defects or damage. Graphene and metal layer are preserved without damage. But it is still observable in some structures that metal layer is peeled partially from the graphene layer, as shown in the bottom left and right corners of Figure 5.10.

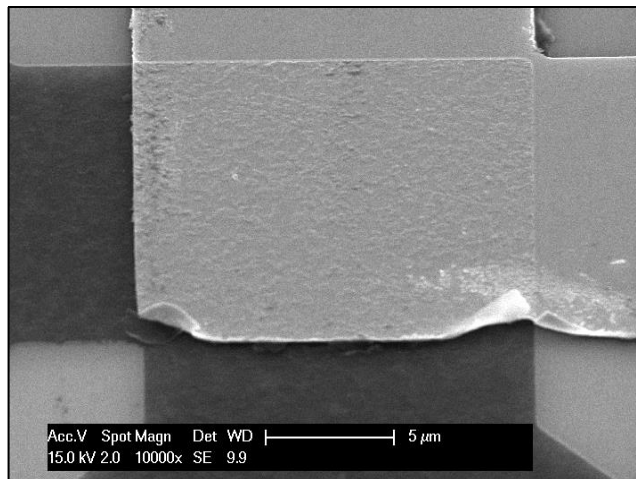

Figure 5.10. SEM picture of Cr/Au contact with parts of metal peeling off from graphene layer

In Figure 5.11, SEM pictures of Ti contact are presented.

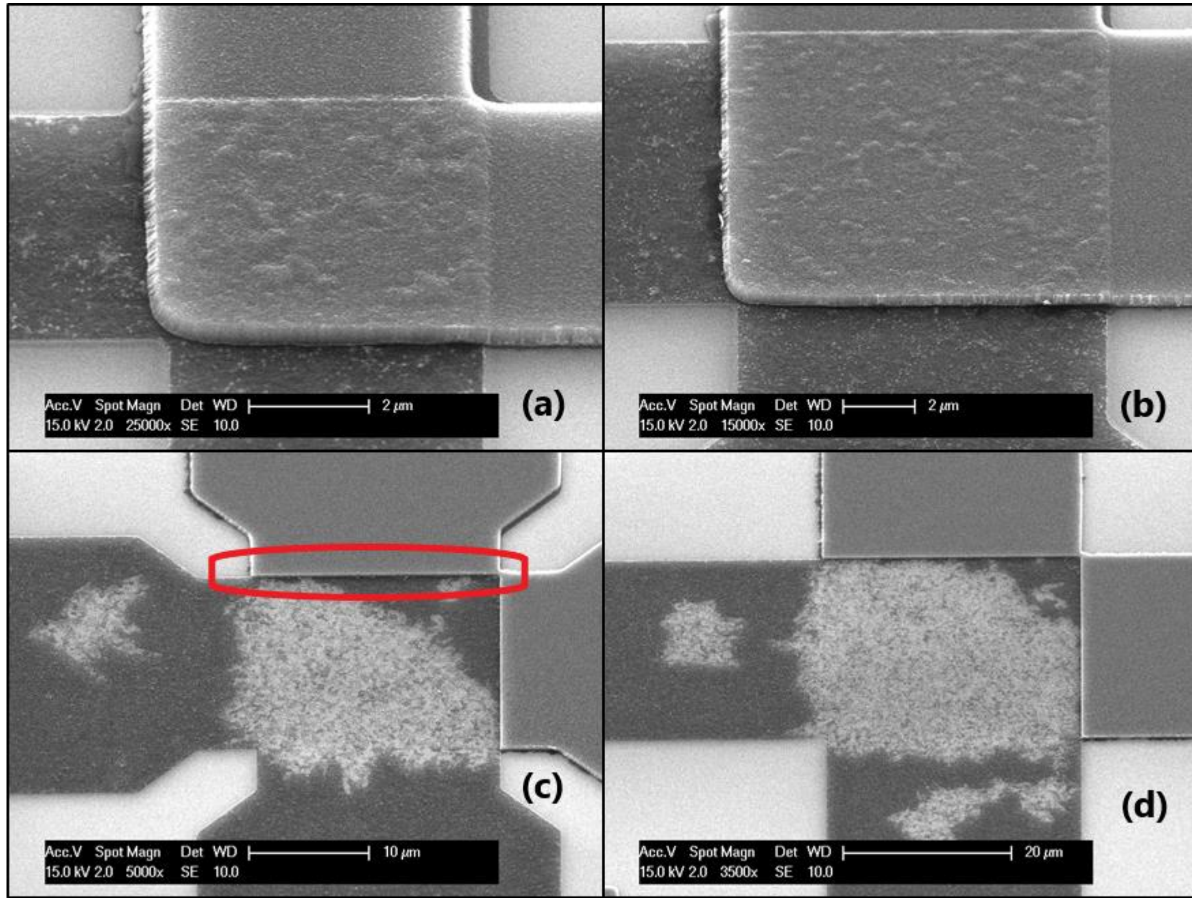

Figure 5.11. SEM pictures of Ti contacts. (a)&(b) present contact area with size 5x5 µm2 and 10x10 µm2 respectively; (c)&(d) present contact area with size 20x20 µm2 and 30x30 µm2 respectively

From Figure 5.11, clearly the deposited layer of Ti is thicker than the desired thickness of 100nm. This thickness error is possibly caused by mis-programming of the deposition profile in the metal deposition machine. Except the thickness, the contact areas with relative small feature size show no major defect or damage, for example the 5x5 μm^2 and 10x10 μm^2 contacts shown in Figure 5.11(a) and 11(b). However, when the contact area size is increased to 20x20 μm^2 or even larger, complete delamination of metal layer on some test structures are observed more and more often. As can be seen in Figure 5.11(c), the contact area is completely cutoff near the neck of the device area marked by a red circle. Graphene layer underneath the metal layer is mostly ripped off from the substrate. The situation is worst when the feature size is the largest at 30x30 μm^2 (Figure 5.11(d)).

For Pd contacts, feature sizes with 2x2 μm^2, 5x5 μm^2 and 10x10 μm^2 have working structures. The SEM pictures of them are presented in Figure 5.12 below. Contacts with larger feature sizes barely left any working device.

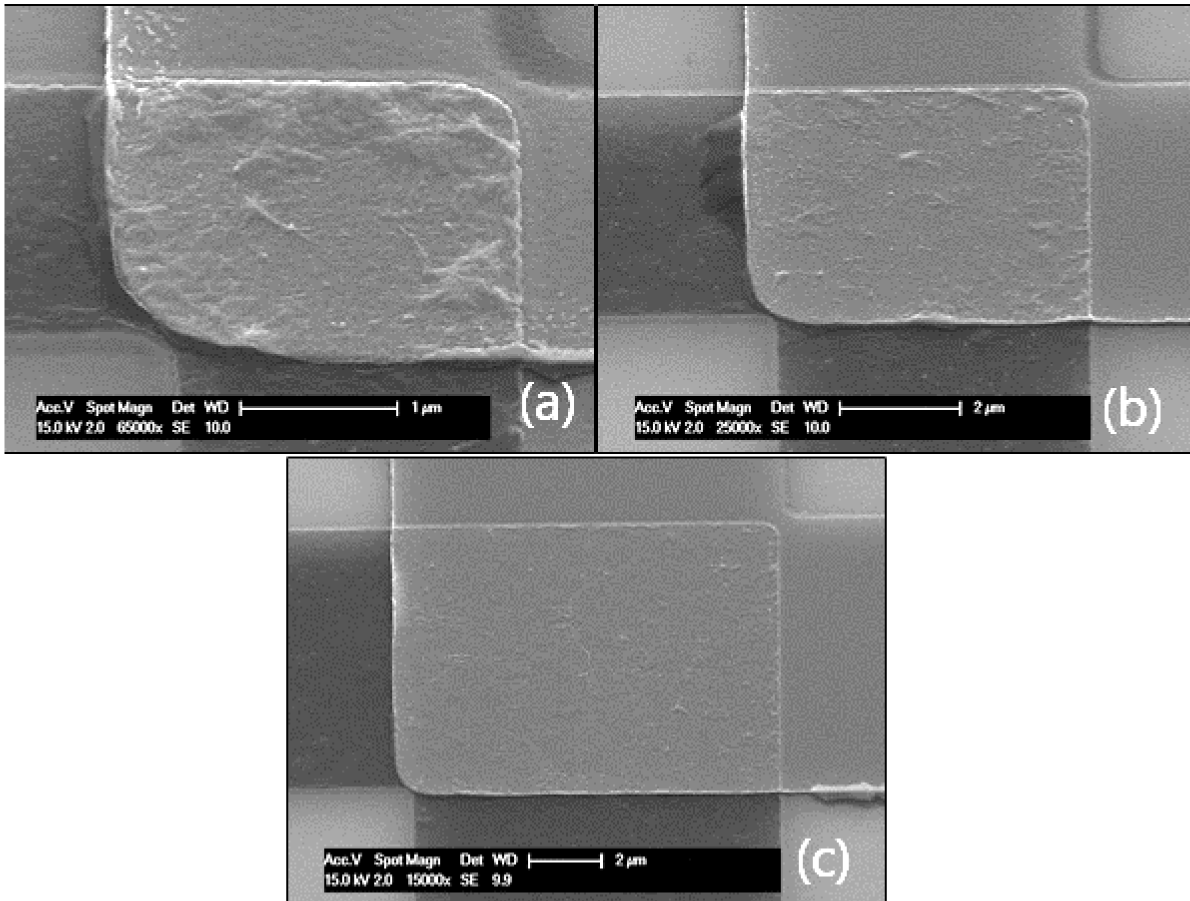

Figure 5.12. SEM pictures of Pd contacts. (a), (b) and (c) present contact area with size 2x2 µm2, 5x5 µm2 and 10x10 µm2 respectively

Judging from the surface texture, the contact area of Pd contacts are relatively well fabricated without damages to either metal or graphene layer, only few parts of the metal layer have curved up slightly. This minor defect is not the same as the peel off situation shown in Figure 5.10.

For Al contacts, SEM pictures are taken for contact area with size 2x2 μm^2, 5x5 μm^2 and 15x15 μm^2, as presented in Figure 5.13 below.

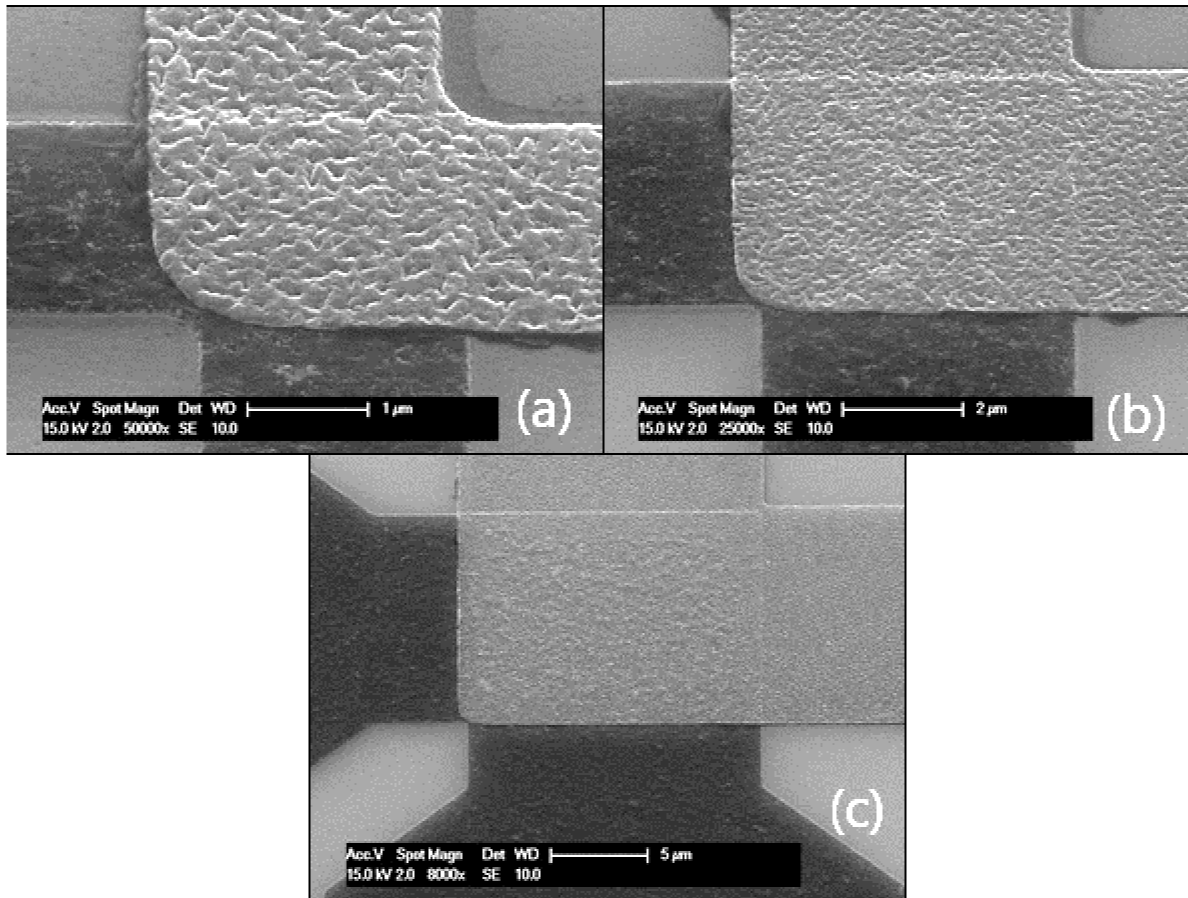

Figure 5.13. SEM pictures of Al contacts. (a), (b) and (c) present contact area with size 2x2 µm2, 5x5 µm2 and 15x15 µm2 respectively

Under inspection with SEM, it is found that on most structures graphene layer stays intact. But the Al layer exhibits very rough surface texture on most structures. This is an unexpected result of the experiment. As can be seen for example in Figure 5.13(a), the Al film deposited on top of graphene layer appears to be porous and has an irregular surface. This phenomenon may be the reason why contact resistance measured from Al contacts often has abnormally high values. To determine the reason behind low-yield problem in this case, more information is needed from future experiments.

At last, for Pt contacts SEM pictures are taken for contacts with various feature sizes. As shown in Figure 5.14 below.

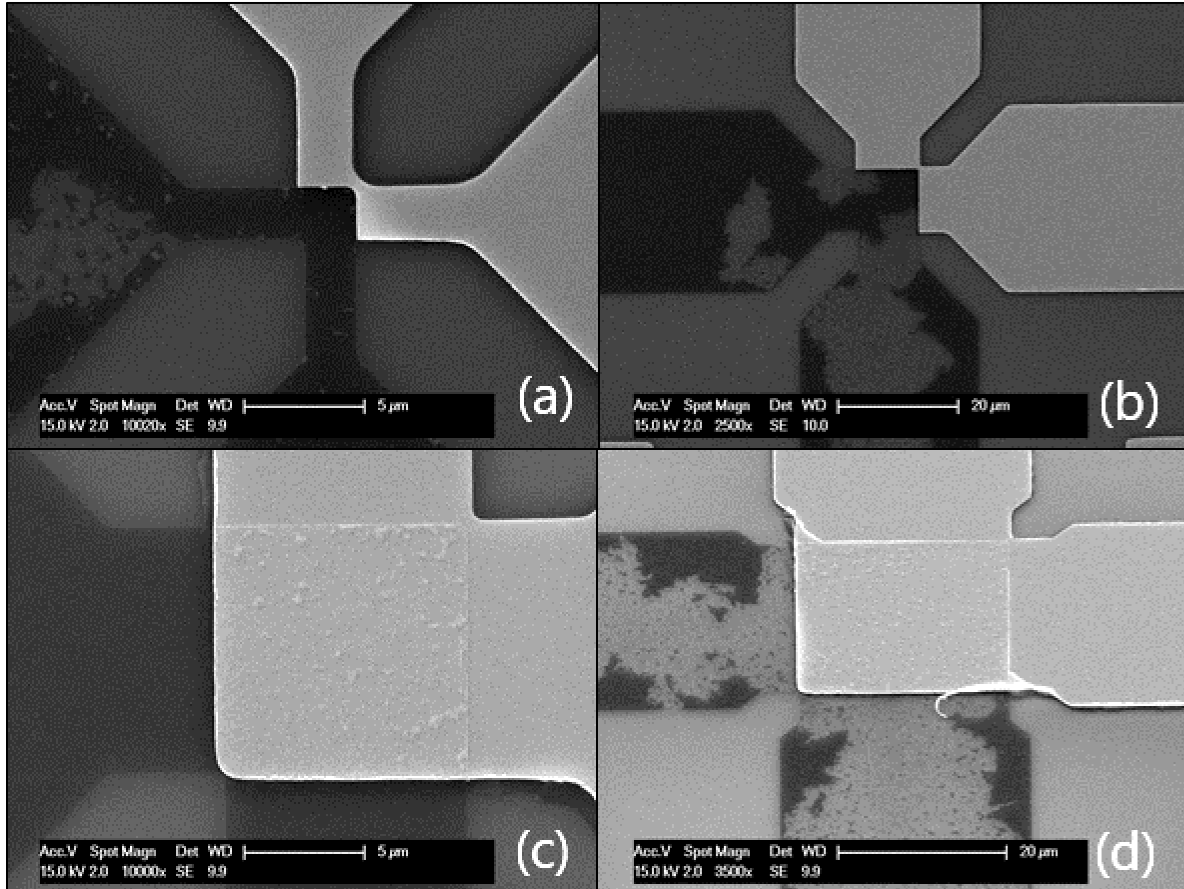

Figure 5.14. SEM pictures of Pt contacts. (a), (b), (c) and (d) present contact area with size 2x2 µm2, 10x10 µm2, 10x10 µm2 and 20x20 µm2 respectively

Figure 5.14(a)-(b) exhibit the delamination of metal layer with graphene peeled off from substrate. Delamination at small feature size does not happen for other metal-graphene contacts. Besides, as Figure 5.14(c) indicates, on many structures the graphene layer out of contact region with metal is completely detached from the substrate, or the graphene layer is severely damaged instead of completely detached from the substrate (Figure 5.14(d)). SEM inspection reveals found that the adhesion of graphene layer is very poor in this case. This also explains why the yield of Pt contacts is extremely poor with basically no working device left.

5.3 Conclusions

Contact resistance measurements are performed on various metal-graphene contacts, including metals like Cr/Au, Ti, Pd, Al and Ta/Pt. The contact area has different feature sizes and it is found that the contact resistance decreases as the feature length or area of increases. Stronger feature length dependency than area dependency is observed through the data from Cr/Au and Ti contacts. The low yield of working structure posed a serious challenge especially in cases of Pd, Al and Ta/Pt contact. Acquiring more data from these structures, then it will be reasonable to infer the relationship of contact resistance in this case.

Through the SEM investigation, the contact area between different metals and graphene are examined with high resolution. It is found that delamination of metal layer occurs more often in contacts with large feature size, such as 20x20 μm^2, 25x25 μm^2 and 30x30 μm^2. A severe graphene layer detachment or peel off from the substrate always happen with metal layer delamination. Among all metal-graphene contacts, Ta/Pt contact has the worst situation since the great majority of devices have delamination of metal layer. In addition, it is unexpected to find that the surface texture of Al contact seems very porous and irregular. This may also explain why there are barely any working device of Al contact despite graphene layer mostly stay intact.

Overall, the contact resistance study demonstrated Cr/Au contact with specific contact resistance as low as 21 $\mu\Omega \cdot cm^2$ and Ti contact with specific contact resistance as low as 82 $\mu\Omega \cdot cm^2$. Cr/Au contact with specific contact resistance of 5 $\mu\Omega \cdot cm^2$ and Ti contact with 0.2 $\mu\Omega \cdot cm^2$ have been reported in ref [2]. Therefore, the ρ_c value of Cr/Au contact and Ti-contact achieved in this study are higher compared with literature. Pd contacts with feature size of 2x2 μm^2 have shown low ohmic specific contact resistance of 0.32 $\mu\Omega \cdot cm^2$, which is comparable with value from literature [2]. In order to find whether metal-graphene contact have a stronger area or peripheral dependency with in general, more experiment data are needed based on an improved fabrication technology with higher yield.

References

1. Cusati, T., Fiori, G., Gahoi, A., Passi, V., Lemme, M.C., Fortunelli, A. and Iannaccone, G., 2017. Electrical properties of graphene-metal contacts. *Scientific Reports*, *7*(1), p.5109.

2. Robinson, J.A., LaBella, M., Zhu, M., Hollander, M., Kasarda, R., Hughes, Z., Trumbull, K., Cavalero, R. and Snyder, D., 2011. Contacting graphene. *Applied Physics Letters*, *98*(5), p.053103.

3. Watanabe, E., Conwill, A., Tsuya, D. and Koide, Y., 2012. Low contact resistance metals for graphene based devices. *Diamond and Related Materials*, *24*, pp.171-174.

4. Giovannetti, G.A.K.P.A., Khomyakov, P.A., Brocks, G., Karpan, V.V., Van den Brink, J. and Kelly, P.J., 2008. Doping graphene with metal contacts. *Physical review letters*, *101*(2), p.026803.

5. Khomyakov, P.A., Giovannetti, G., Rusu, P.C., Brocks, G.V., Van den Brink, J. and Kelly, P.J., 2009. First-principles study of the interaction and charge transfer between graphene and metals. *Physical Review B*, *79*(19), p.195425.

6. Xia, F., Perebeinos, V., Lin, Y.M., Wu, Y. and Avouris, P., 2011. The origins and limits of metal-graphene junction resistance. *Nature nanotechnology*, *6*(3), pp.179-184.

7. Matsuda, Y., Deng, W.Q. and Goddard III, W.A., 2010. Contact Resistance for “End-Contacted” Metal− Graphene and Metal− Nanotube Interfaces from Quantum Mechanics. *The Journal of Physical Chemistry C*, *114*(41), pp.17845-17850.

8. Stavitski, N., Klootwijk, J.H., van Zeijl, H.W., Kovalgin, A.Y. and Wolters, R.A., 2009. Cross-bridge Kelvin resistor structures for reliable measurement of low contact resistances and contact interface characterization. *IEEE Transactions on Semiconductor Manufacturing*, *22*(1), pp.146-152.

Chapter 6 Thesis Conclusions and Recommendations

6.1 Conclusions of thesis study

The central goal of this thesis study is to investigate potential effects of differently prepared SiO_2 substrates on gas sensing behaviors of graphene sensors. To be more specific, it is essential to determine whether there are different sensing behaviors from graphene gas sensors using thermal oxide, LPCVD oxide or PECVD oxide substrate. In the end of this thesis work, I can infer that the sensing behaviors are evidently altered among graphene gas sensors using differently prepared oxide substrates. Besides, supported by the findings of experiments, some reasons to explain the why these oxide substrates cause different sensing behaviors are also revealed.

Starting from the motivation of this research opportunity, the possibility of controlling gas sensing properties by engineering the substrate properties of graphene gas sensor has been evaluated [*Chapter 1&2*]. Following this thread, gas sensing experiments using graphene as active medium have been carried out under three different testing protocols [*Section 3.1*]. Protocol (I) is the standard test with a one-time analyte exposure window with a fixed analyte concentration. From the sensing responses under protocol (I) [*Section 3.2*], it is found that the greatest magnitude of response and rate of response variation are achieved from graphene gas sensors using PECVD oxide substrate (P sensors). Graphene sensors using thermal oxide substrate (T sensors) have the least magnitude and rate of response variation. Graphene sensors using LPCVD oxide substrate (L sensors) act in between the other two types. In addition, it is observed that sensing responses from P sensors have the largest spread of data as well, while responses from T sensors having the least. Protocol (II) is the continually repeated version of protocol (I) for five times. Sensing responses under protocol (II) [*Section 3.3*] verified the reproducibility of sensing responses from protocol (I). The observations of sensing responses from protocol (II) are in agreement with those from protocol (I). Unlike the previous two protocols, protocol (III) contains a uniformly decreasing analyte concentration profile, so that the intention of protocol (III) is focused on evaluating how sensors respond with respect to the changing concentration [*Section 3.4*]. As shown in Table 3-6 and Figure 3-14, it is observed that as the analyte concentration is decreasing, the magnitude of response and rate of response variation is also diminishing. Similar conclusions seen from previous analysis occurred, however, there are uncertainties. It can be inferred that P sensors still hold largest magnitude of response and rate of response variation at all analyte concentration levels. Future experiments are needed for further verification.

Seeing the differences in gas sensing behavior among T sensor, L sensor and P sensor, it is concluded that the choice of substrate oxide material leads to substantial changes in graphene gas sensor responses. Next, in order to explain the reasons why three oxide substrates bring different effects to graphene gas sensors, material properties of thermal, LPCVD and PECVD oxides are studied with C-V measurements and FTIR measurements. C-V measurements [*Section 4.2*] provided results of fixed oxide charge within oxide substrates. Results point out that thermal oxide has least fixed oxide charge while LPCVD oxide having the most. The fixed oxide charge of PECVD is slightly smaller than that of LPCVD oxide. Based on these findings, conclusion is drawn that the quality of thermal oxide layer is the best, with least lattice damage or impurities. PECVD and LPCVD oxide all contains certain amount of impurities making them defective in the sense of oxide structure. This is the first indication linking the defects in oxide structure to the effect on graphene sensing responses from an oxide substrate. Moreover, FTIR measurements [*Section 4.3*] are further performed with the aim to infer the structures of these three oxide substrates. The characteristic bands of SiO_2 are found in all oxide layers, while peak data indicate thermal oxide being the closest to crystalline SiO_2. LPCVD oxide structure is slightly worse than that of thermal oxide. Moreover, from spectrum analysis it is determined that PECVD has the most porous structure with unsaturated bonds among

all types of oxide substrates. The existence of "Si-H" band at 870 cm^{-1} from the FTIR spectrum of PECVD oxide further supports this judgement. Results from FTIR measurements are also indications linking the defects in oxide structure to the effects on gas sensing behaviors from oxide substrates. Therefore, in Chapter 4, it is concluded that the quality of oxide substrate is a direct influencing factor of graphene gas sensing behavior.

Additionally, Raman analysis of the few layer graphene (FLG) on top of different oxide substrates [*Section 4.4*] demonstrated that in fact FLG used in all sensors is the same. Hereby, it is proved that the differences on gas sensing behaviors come predominately from the effects of different oxide substrates. Finally, all the adopted techniques totally agreed that through engineering the oxide substrate, the responses of graphene-based gas sensors can be improved. In particular, defects in oxide substrates play a fundamental role: the more porous and imperfect the oxide is, the higher the sensing response magnitude and rate of response variation will be.

Besides the investigation around oxide substrate, particular attention has been paid to the study of contact resistance (R_c) between graphene and metals, in addition to evaluate whether metal-graphene contact resistance has a stronger area or peripheral dependency. This study presents the effort to improve graphene gas sensor system overall for future possible applications. For this goal, cross-bridge-kelvin-resistor (CBKR) structures with various feature sizes ranging from 2x2 μm^2 to 30x30 μm^2 are fabricated in order to measure contact resistance values between graphene and metals including Cr/Au, Ti, Pd, Al and Pt [*Section 5.2*]. Through preliminary experimental work, contact resistance values are successfully measured from Cr/Au, Ti, and Pd-graphene contacts. First, it is shown that R_c decreases as feature length/area increases. A stronger R_c dependency on feature length than feature area is shown on both Cr/Au-graphene and Ti-graphene contacts. In addition, it is also discovered that Pd-graphene contacts have even lower contact resistance values than Cr/Au-graphene contacts when the contact area is no larger than 5x5 μm^2. However, the low-yield of working device was a difficulty greatly limited the amount of useful data obtained through measurements. Although Cr/Au, Ti-graphene contacts have acceptable yield on all feature sizes, the yield is found to be decreasing as feature size increases. Pd-graphene contacts only produced enough useful data under feature sizes of 2x2 μm^2 and 5x5 μm^2 and barely any Al-graphene or Pt-graphene contact survived for measurement on any feature size. With the limited amount of data, contact resistance of metal-graphene contacts are found to be more dependent on feature length than area. It is worth increasing the yield first in future experiments to be able to add credibility to the results reached in this study.

6.2 Recommendations for future works

A couple of recommendations are purposed based on the conclusions or problems encountered in experiments throughout this thesis work:

1. to provide more credibility to the conclusions concerning the gas sensing measurements, it is necessary to perform more experiments, especially under protocol (III). New protocol such as a random analyte concentration can also be adopted to test the conclusions from previous experiments.

2. Structure of oxide substrates can be differently investigated by other techniques, such as AFM, to directly compare the level of structure defectiveness among different oxide substrates.

3. Since the possibility of improving sensing response through engineering defects in oxide materials is proved, it is worth performing gas sensing experiments on sensors based on oxide substrates fabricated with different level of defectiveness. Ion implantation is one of the suitable technology

to do so. For example, by controlling the energy of bombarding ions, thermal oxides with different level of defects can be produced. Although annealing during graphene growth step will recover parts of the damage in crystal structures, but this effect can be considered limited.

4. As it concerns the contact resistance, the yield for metal-graphene contact fabrication is low and this draw-back brought difficulty for research. It is often found that graphene layer detaches form substrate after metal lift-off process. Through postponing the Mo etch after the metal lift-off step will possibly help improve the yield of working structures.

5. A more dedicated experiment is needed to investigate whether contact resistance have a stronger area or peripheral dependency. To do so, two sets of contact regions with different geometry layout can be fabricated. One set features different area but same perimeter, while the other set features same area but different perimeter.

Appendix A CVD Graphene Growth Environment

In this thesis study, chemical vapor deposition of graphene is performed in AIXTRON BlackMagic Pro machine. Unlike conventional methods, the graphene growth recipe in this thesis study uses Molybdenum (Mo) as the catalyst rather than Copper. Nevertheless, the conditions of ambient environment and other parameters such as temperature profile and ingredients are similar to the conventional method.

From Figure A1 below, the ambient temperature and related ingredients of the graphene growth at different stages of the conventional method can be observed. Slight differences can be noticed compared to the following description of the processes in the real recipe.

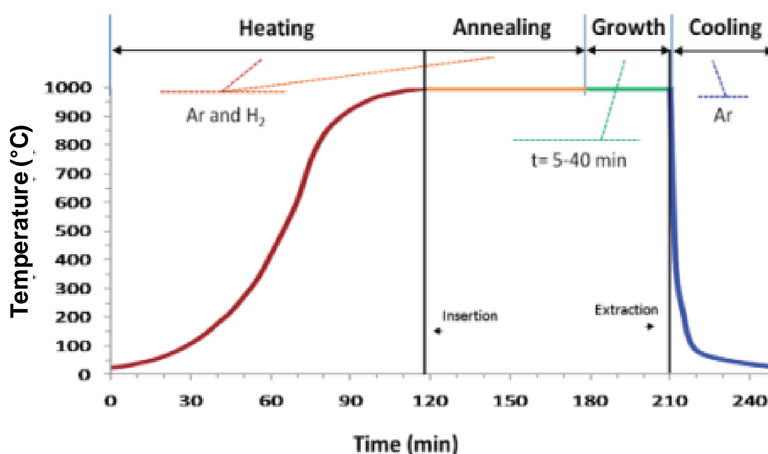

Figure A1. Example graphene growth process. Source: ENEA

To grow CVD graphene, at first the 4-inch sample wafer with pre-deposited Mo catalyst layer is loaded in the machine. Then environment temperature is gradually heated up to around 950°C to 1050°C in order to let reactions take place in the growth stage. The precursor gas mixtures for graphene growth are hydrogen (H_2)/argon (Ar)/ethanol (C_2H_6O) or H_2/methane (CH_4). Once the programmed conditions are met, gas mixture is introduced and graphene starts to grow for a certain period of time in the growth stage. When growth time is reached, gas mixture is switch off and the sample starts to cool down at a rate around 50°C per minute till room temperature. Gradual cooling is taken to reduce graphene film stress and cracks.

Speaking of graphene growth environment here, it is also worth some more discussion about the annealing effect on FTIR samples brought by the step to mimic graphene growth.

The discussion in Chapter 4 (page 43) reported the effect of annealing on the removal of hydrogen contents in PECVD oxide samples. In fact, for PECVD oxide used in FTIR measurements, the hydrogen contents can escape efficiently because there is no Mo catalyst layer deposited on top of the oxide. However, in the structure of a real graphene gas sensor, the oxide layer is capped by the catalyst layer, so that the hydrogen contents will not be able to escape from the oxide layer in the case of the FTIR measurements. Therefore, the annealing effect by the graphene growth step on a real graphene gas sensor will be different and likely to exhibit existence of more hydrogen contents.

Appendix B Processing Details of C-V Structures

Starting Material

Single side polished process wafers, with the following specifications:

- Type: p-type
- Orientation: 1-0-0, 0 deg off orientation
- Resistivity: 2-5 Ωcm
- Thickness: 525 ± 15 μm
- Diameter: 100.0 ± 0.2 mm

1. Thermal Oxidation

Target thickness: 90 nm

Program: Dry Oxidation at 1050°C

1. Plasma Enhanced CVD Oxidation

Novellus Concept One, target thickness: 90nm

Program: standard deposition of undoped oxide

1. Low Pressure CVD Oxidation

Target thickness: 90 nm

Program: new teos

2. Measurement: Oxide Thickness

Desired oxide thickness: 90nm

3. Heating in AIXTRON Black Magic Pro to mimic graphene growth using LPCVD

4. Metal Deposition on Wafer Frontside

Use the TRIKON SIGMA sputter coater for the deposition of the metal Al layer on the process wafers

Program: Al 675nm AlSi at RT

5. Backside Oxide Stripping

Use a dedicated contaminated plastic beaker with BHF (1:7) to strip the oxide on the backside of the wafers. Approximate etch rates are:

Thermal oxide: 80 nm/min

PECVD oxide: 340 nm/min

LPCVD oxide: 240 nm/min

Rinse in DI water for 5 min, dry using single wafer dryer.

Perform next step directly after the oxide etch.

6. Metal Deposition on Wafer Backside

Use the TRIKON SIGMA sputter coater for the deposition of the metal Al layer on the process wafers

Program: Al 2075nm AlSi at RT

7. Manual Coating and Baking

Perform a 10min HMDS treatment; Spin-coat 2.1 um of Shipley SPR3012 positive photoresist; Followed by 1min 95°C soft bake using the hotplate for contaminated wafers.

8. Exposure

Use ASM PAS 5500/80 automatic waferstepper.

9. Manual Development

Perform a cross-link bake at 115°C for 60s using the hotplate for contaminated wafers

Manual development in Shipley MF322 for 60s using glassware for contaminated wafers

Perform a hard bake at 100°C for 120s using hotplate for contaminated wafers

10. Manual Al etching

Use PES77-19-04 at 35°C to etch the Al and perform a 30s over etch.

Appendix C Processing Details of Metal-graphene Contacts

Starting Material

Single side polished process wafers, with the following specifications:

- Type: p-type
- Orientation: 1-0-0, 0 deg off orientation
- Resistivity: 2-5 Ωcm
- Thickness: 525 ± 15 µm
- Diameter: 100.0 ± 0.2 mm

1. Coating and Baking

Use EVG 120 wafertrack to coat wafers with Shipley SPR3012 positive photoresist (thickness 1.4 µm)

2. Alignment and Exposure

Use ASM PAS 5500/80 automatic waferstepper

3. Development

Use the EVG 120 wafertrack to develop the wafers.

4. Inspection: line width

Visually inspect the wafers through a microscope and check line width. No resist residues are allowed.

5. Number wafers

6. Plasma Etching of Alignment Marks

Use TRIKON Ωmega 201 plasma etcher

7. Cleaning Procedures

Plasma strip: use the Tepla plasma system to remove photoresist in an oxygen plasma.

Cleaning: 10 minutes in fuming nitric acid (Merck: HNO_3 100% selectipur) at ambient temperature

QDR: rinse in the Quick Dump Rinser with the standard program until the resistivity is 5MΩ

Cleaning: 10 minutes in concentrated nitric acid (Merck: HNO_3 65%selectipur) at 110°C

QDR: rinse in the Quick Dump Rinser with the standard program until the resistivity is 5MΩ

Drying: use the dryer tool.

8. Dry Oxidation with 90nm target thickness

9. Measurement: oxide thickness

Desired oxide thickness: 90nm

10. Mo deposition using TRIKON SIGMA. Target thickness: 50nm

11. Coating and Baking

Use EVG 120 wafertrack to coat wafers with Shipley SPR3012 positive photoresist (thickness 1.4 µm)

12. Alignment and Exposure

Use ASM PAS 5500/80 automatic waferstepper

13. Development

Use the EVG 120 wafertrack to develop the wafers.

14. Inspection: line width

15. Plasma Etching of Molybdenum

Use TRIKON Ωmega 201 plasma etcher.

16. Resist Stripping in NMP

Use NMP at 70°C for 8 mins. Use a q-tip to remove residues.

17. Graphene Growth

Use AIXTRON Black Magic Pro to grow graphene.

18. Titanium Nitride deposition at Backside

Use TRIKON SIGMA for deposition of the capping metal TiN layer

Program: Ti10 TiN 200 50C

19. Coating and Baking

Use EVG 120 wafertrack to coat wafers with AZ NLOF 2020 negative photoresist (thickness 3.5 µm)

20. Alignment and Exposure

Use ASM PAS 5500/80 automatic waferstepper

21. Development

Use the EVG 120 wafertrack to develop the wafers.

22. DUV Bake

23. Metal Deposition

Metal	Thickness [nm]	Tool
Cr/Au	10/100	Balzers
Ti	100	Sigma or CHA
Al (1%Si)	100	Sigma or CHA
Pd	100	CHA
Ta/Pt	10/100	CHA

24. Lift-off

Perform lift-off using an ultrasonic bath with heated NMP > 50°C

List of Abbreviations

Abbreviation	Definition
PM2.5	Atmospheric particulate matter with a diameter less than 2.5 μm
CNT	Carbon nanotube
2D	2 dimensions
LPCVD	Low pressure chemical vapor deposition
PECVD	Plasma enhanced chemical vapor deposition
FLG	Few layer graphene
SLG	Single layer graphene
MLG	Multi-layer graphene
FET	Field effect transistor
SWF	Surface work function
SAW	Surface acoustic wave
GSCS	Gas sensor characteristic system
FTIR	Fourier-transform infrared spectroscopy
T sensor	Graphene gas sensor using thermal oxide as substrate
L sensor	Graphene gas sensor using LPCVD oxide as substrate
P sensor	Graphene gas sensor using PECVD oxide as substrate
C-V	Capacitance-voltage
MOSCAP	Metal-oxide-semiconductor capacitor
BJT	Bipolar junction transistor
DI	Deionized
TEOS	Tetraethyl orthosilicate
DTGS	Deuterated-triglycine sulfate
SEM	Scanning electron microscope
CBKR	Cross Bridge Kelvin Resistor
NMP	N-Methyl-2-pyrrolidone
Cr/Au contact	Cr/Au graphene contact

List of Symbols

Symbol	Description
M	Ratio of conductance variation
$\frac{\partial G}{\partial t}$	Derivative of conductance variation [nS/s]
V_g	Gate voltage [V]
ε_r	Relative permittivity
Q_f	Fixed oxide charge [e/cm^{-2}]
V_{FB}	Flat-band voltage [V]
Q_{ox}	Fixed oxide charge [e/cm^{-2}]
φ_m	Metal work function [eV]
φ_s	Semiconductor work function [eV]
φ_{ms}	Metal semiconductor work function difference [eV]
C_{FB}	Capacitance at flat-band voltage [pF]
C_{min}	Minimum capacitance of oxide obtained during C-V measurement [pF]
C_{ox}	Maximum capacitance of oxide obtained during C-V measurement [pF]
N_A	Acceptor doping concentration [cm^{-3}]
K	Wavenumber [cm^{-1}]
λ	Wavelength [cm]
R_c	Contact resistance [Ω]
R_K	Kelvin resistance [Ω]
ρ_c	Specific contact resistance [μΩ• cm^2]